12-1-2016

A Validation Study of Gearing and Musculoskeletal Performance in Simple Biological Systems through Theoretical and Experimental Methods

Jenna Marie Hopkins
jmh9066@rit.edu

ROCHESTER INSTITUTE OF TECHNOLOGY

A Validation Study of Gearing and Musculoskeletal Performance in Simple Biological Systems through Theoretical and Experimental Methods

by
Jenna Marie Hopkins

A thesis submitted in partial fulfillment of the requirements for the degree of Master of Science in Mechanical Engineering

Department of Mechanical Engineering
Kate Gleason College of Engineering

Rochester, NY
December 1, 2016

Committee Approval

Dr. Steven Day **Date**
Thesis Advisor
Department Head of Biomedical Engineering

Dr. Kathleen Lamkin-Kennard **Date**
Committee Member
Department of Mechanical Engineering

Dr. Mario Gomes **Date**
Committee Member
Department of Mechanical Engineering

Dr. Alan Nye **Date**
Department Representative
Department of Mechanical Engineering

DEPARTMENT OF MECHANICAL ENGINEERING

Abstract

Musculoskeletal (MSK) systems have long been compared to simple mechanical machines. This not only allows for ease of understanding locomotion, but ease of modeling a biological system during complex motion. More specifically, simple lever systems are most commonly employed to approximate mechanical performance of complex biological systems. Every simple lever system can be characterized by its mechanical advantage, also known as gearing. Through this concept, the performance of a biological system can be modeled for comparability of theoretical concepts to actual MSK systems. In this thesis, a numerical model of a simple lever system, analogous to a locust leg and fish fin, was developed to understand the effects of mechanical advantage, muscle actuator, and external forces on simple MSK systems. Validation of the numerical model was attempted through the use of an existing McKibben air muscle test fixture. Conditions related to force loading, inertial loading, and viscous loading were tested.

The mathematical model showed that the spring-damper in parallel matches the expected results of the Hill's muscle model, where increases in muscle loading cause decreases in muscle velocity. Further, experimental tests conducted on the existing test fixture employed the addition of two dampers parallel with the McKibben air muscle. The data suggested that for a given damping scenario, under direct loading conditions, there is a maximum potential contractile velocity that could be achieved. Inertial loading tests provided a comparison in the fluid effects where observations illustrate the 100% glycerine trials caused a greater drag force to dampen the paddle velocity than the room temperature water solution.

Acknowledgements

I would like to thank: my family and friends who have supported me, not only through my college career, but my journey through my thesis project, the machine shop staff that have helped me by answering my various machining questions, and machined out various portions of the experimental test fixture, Mr. Andy Phatak for helping set-up the experimental test fixture and teaching me how to use it, and Dr. Steven Day, my thesis advisor, for the continual support, knowledge, and encouragement throughout my theoretical and experimental research.

Table of Contents

List of Figures

List of Tables

List of Equations

Nomenclature

Abbreviations:

MSK – Musculoskeletal system

ATP – Adenosine triphosphate

RFA – First-class levers with resistive force-fulcrum-application force structure

FRA – Second-class levers with fulcrum-resistive force-application force structure

FAR – Third-class levers with fulcrum-application force-resistive force structure

MTC – Muscle-tendon-complex

MCP – Metacarpophalangeal joints

ext – Extension

flex – Flexion

plantarflex – Plantarflexion

dorsiflex – Dorsiflexion

FF – Fully forward

IFT – Inverse forward starting at joint torque

IFM – Inverse forward staring at muscle force

EMG - Electromyography

FE – Finite element

PL – Plantaris longus

Variables:

M – Muscle moment arm (N/m)

r – Distance of force application to pivot point (m)

F_{muscle} – Applied contractile force (N)

$\theta_{application}$ – Angle of application (rad)

F_I – Isometric muscle contraction force (N)

A –Mechanical advantage (-)

F_r – Resistive force (N)

$F_{application}$ – Application force (N)

F – Force (N)

V – Shortening Velocity (m/s)

a – Coefficient of shortening heat (-)

b – Constant parameter based on Coefficient of shortening velocity, maximum isometric tension, and maximum shortening velocity (m/s-N)

F_0 – Maximum isometric tensile force (N)

V_0 – Maximum isometric contraction velocity (m/s)

$[R]$ –Moment arm matrix (Nm)

$\{t\}$ –Muscle tension (N)

$\{m_L\}$ –Elements of passive actions of MCP collateral ligaments (-)

$\{m_f\}$ –External force about each degree of freedom (N)

$(t_m)_s$ – Muscle tension of the muscle, *m*, for solution, *s* (N)

m—Muscle (-)

n –Parameter to exclude non-physiological results (-)

$PCSA_m$ –Physiological cross-sectional area of muscle, *m* (mm²)

$\{J_R\}_j$ –Joint reaction force (N)

$\{T\}_m$ – Estimated muscle tension of muscle, *m* (N)

$\{F\}_a$ – Grip force applied on anatomical area of finger, *a* (N)

$\{L\}_l$ – Passive MCP collateral ligament force, *l* (N)

U –Jump take-off velocity (m/s)

Π –Elastically stored energy in animal's legs (J/kg)

m_{body} –mass of body (kg)

H –Maximum jump height (mm)

g – Gravitational force (m/s²)

R – Ground reaction force (N)

β –Angle of joint (rad)

P –Center of pressure (mm)

j –Center of joint (mm)

$r^{\frac{p}{j}}$ –Position of the center of pressure (mm)

F_g –Force vector of ground reaction force moment (N)

F_m –Force vector of muscle moment (N)

E_p – Net gravitational potential energy (J)

E_{Kh} – Net kinetic energy in fore aft direction (J)

E_{Kv} – Net kinetic energy in vertical direction (J)

I – Moment of inertia (kgm²)

$\ddot{\theta}$ – Angular acceleration (rad/s²)

θ – Angular displacement (rad)

l_{in} – In-lever length and upper leg length (m)

l_{out} – Out-lever length and lower leg length (m)

F_{spring} – Spring force (N)

k – Spring stiffness (kg/s²)

L – Length of spring (m)

$sstetch$ – Spring stretch past resting length (m)

θ_{leg} – Angular displacement of leg during rotation (deg)

$F_{applied}$ – Summation of all spring and damper forces related to theorized muscle (N)

F_{damper} – Damping force (N)

c – Coefficient of damping (kg/s)

V_m – Muscle velocity (m/s)

$F_{reaction}$ – Ground reaction force (N)

F_{drag} – Viscous drag force (N)

C_d – Coefficient of drag

ρ – Fluid density (kg/m³)

$V_{l_{out}}$ – Velocity of lower leg/fin (m/s²)

A_f – Frontal area that the drag force acts on (m²)

$RoCAM$ – Rate of change of angular momentum (Nm)

α – Angular acceleration of a system (rad/s²)

Chapter 1: Introduction to Musculoskeletal Systems

1.1: Skeletal System Review

Within biological systems, the musculoskeletal system (MSK) is comprised of two sub components: the skeletal system and the muscular system. These subsystems help provide support, shape, movement, and organism stability [1, 2].

The skeletal system is composed of hard tissues, such as bone, and the various connective tissues that help provide shape and form to the body. Bone makeup consists of cancellous and cortical bone, as shown in figure 1. Cancellous bone, also known as trabecular or spongy, has long been compared to honeycomb structures. Within the null space of cancellous bone or medullary cavity, bone marrow thrives to promote supplies for new bone formation and growth [3 - 5, 6] In contrast, cortical bone, known as compact bone, serves for the main function of hard tissue structures, support and protection. This bone component is found on the outer exterior of the hard tissue [3].

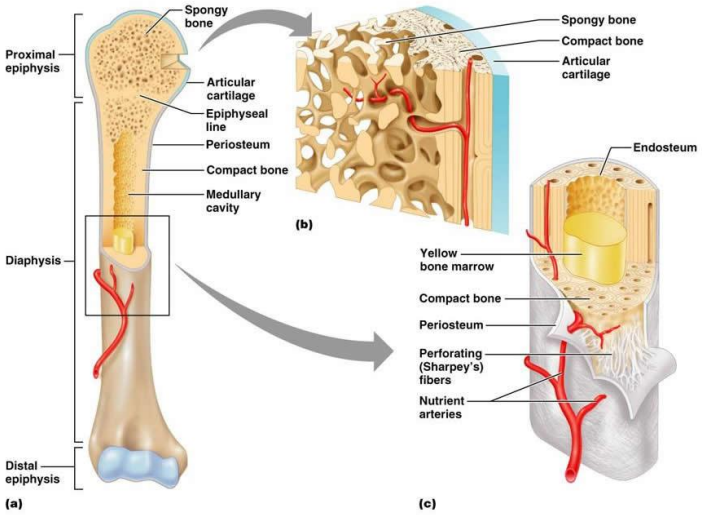

Figure 1: Human bone consists of cancellous bone (b), known as trabecular or spongy bone, and cortical bone (c), known as compact bone. Cancellous bone, although not strong due to the honeycomb nature of the trabeculae and porosity ranging from 50 to 90%, is important to the production of red blood cells and mineral storage. Cortical bone, consists of osteons that are tightly packed together to give the bone porosity of 5 to 10%. Due to the higher density, cortical bone's main function is to protect, and store adipocytes within white bone marrow [4, 7,8].

Mechanically, cortical bone is a composite material comprised of hydroxyapatite crystals bound in a collagen-based polymeric matrix. This allows for the material to behave in a linear elastic manner. Further, due to the composition, bone is anisotropic in nature [5]. This is a key feature as it causes the material properties to change in relation to direction. Specifically, bones have higher toughness strengths in compression and tension longitudinally than transversely. This can also be related to the structure and placement of bones within the body. Lower extremities have much higher toughness strengths than the upper body counter parts [1]. The material properties of bone are shown in table 1. In relation to cancellous bone, the material behaves similar to beams or plates within a structural frame [5]. Since the design of cancellous bone is not the same from one anatomical site to another, the strength and stiffness can vary greatly because of the porosity and trabecular design. Through experimentation, it has been seen that cancellous bone has an elastic modulus ranging from 10 – 2000 MPa, and strength of 0.1 – 30 MPa [5].

	Longitudinal Direction	**Transverse Direction**
Elastic Modulus(GPa)	17	11.5
Shear Modulus (GPa)	3-3.5	
Ultimate Strength, Tension (MPa)	120-130	51
Ultimate Strength, Compression (MPa)	170-180	133
Ultimate Shear Strength	68	

Table 1: Above are experimental results from various tests of human cortical bone in both the longitudinal and transverse directions. Although, depending on the specimen, bone location, and type of testing, the mechanical properties of the bone can vary [5].

The classification and characterization of specific bones is determined by the structural shape. The classifications of bone are: long, short, flat, irregular, and sesamoid [1, 4, 6]. Long bones are tubular in shape with a hollow medullary cavity in the center for adult yellow marrow to exist. Short, flat, irregular bones are consistent of thin periosteum-covered cortical bone and endosteum-covered cancellous bone. The bone marrow within this hard tissue resides in the trabeculae structures of the honeycomb-like formation [4, 6].

Of the main body functions, protection of the internal organs and soft tissues is vital to the survival of the organism. However, it is not possible for bone to accomplish this task without the help of skeletal connective tissues. These tissues are cartilage, ligaments, and tendons.

Articular cartilage is a hydrated hard tissue that covers the connecting surfaces at joints. It functions as a shock absorber to impacts or falls while also lubricating the joint surfaces with synovial fluid. Ligaments and tendons help control placement of contact surfaces within joints by transmitting tensile forces between structures. Ligaments bond two bones together, where tendons attach muscle to bone. Material properties for both ligaments and tendons can be seen in table 2, although research notes that the change in values from anatomical sites vary greatly.

	Tendon	**Ligament**
Elastic Modulus (MPa)	500-1850	50-541
Ultimate Strength, Tensile (MPa)	50-125	13-46
Ultimate Strain (%)	10-60	10-120

Table 2: Similarly to mechanical properties of bone, tendons and ligaments have a wide range. This is dependent upon the anatomical site the specimen is taken from, and the deformation rate of that site. As shown above, tendons have higher elastic moduli and ultimate strength than ligaments due to the necessity of tendons bearing the locomotive actions of muscles. Further, ligaments join bones together, and generally do not bear loads unless in extreme cases of flexion or extension [5].

1.2: Muscular System Review

In order to allow the rigid skeletal system provide locomotion of an organism, the muscular system must be explored. The human body is made up of 630 different skeletal muscles that have been characterized to have fast- and slow-twitch contractions of 1/20 and 1/10 of a second, respectively [1]. In relation to MSK, skeletal muscles attached to various hard tissues enable the movement desired by an organism, as opposed to smooth and cardiac muscle. Within the body, skeletal muscle is organized in antagonistic pairs, for example biceps and triceps of the upper arm. This organization allows for the motion of the joint to be controlled and stabilized. Furthermore, movement is aided through the use of synergists. Synergists are types of muscles that help refine the motion for more specific pathways. As the antagonistic muscles of the leg help bend the joint for walking, synergist muscles help change the path and specific placement of the foot.

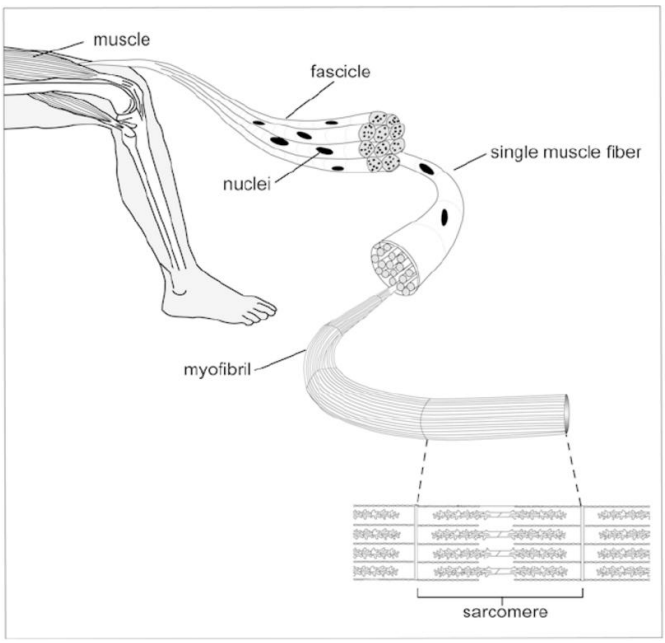

Figure 2: Above the functional decomposition of muscle is broken down to the smallest unit, also known as a sarcomere. Sarcomeres contain actin, a contractile protein, and myosin, a motor protein, which allow for muscular flexion and extension at the presence, or lack thereof, of ATP, among other necessary molecules (i.e. creatine phosphate, calcium, and glycogen). In general, each muscle fiber contains an array of myofibrils that run the entire length of the singular fiber. A bundle of myofibrils, which are surrounded by connective tissue called perimysium, form fascicle of skeletal muscle. From here several fascicles form the overall skeletal muscle [1, 9].

Skeletal muscles enable the movement through shortening. In general, shortening is a force that causes tension within the sarcomeres, the basic unit of striated muscle, and is best explained through the sliding filament theory by Huxley [10]. In this theory, it is suggested that myosin does not change length in muscle contraction. Rather, actin changes in length along the sarcomere. The theory explicitly states, sliding action of actin filaments past myosin filaments, within the sarcomere, causes the necessary tension of muscles [11]. A visual of this theory can be seen in figure 3, as the contraction of muscle occurs, the A band, where myosin are housed, remains constant in length.

Muscles can contract in three different manners, concentric, eccentric, and isometric contractions, depending on the movement being accomplished. Concentric contractions occur during positive, energy-generating work. The energy of the system is increased during this contraction, and, subsequently, the angular velocity at the joint in motion increases. On the other hand, eccentric work decreases the angular velocity of the joint, and ultimately decreases the

energy being produced in the system. This is comparable to the muscles acting as a brake for the joint movement to come to a halt or slow down.

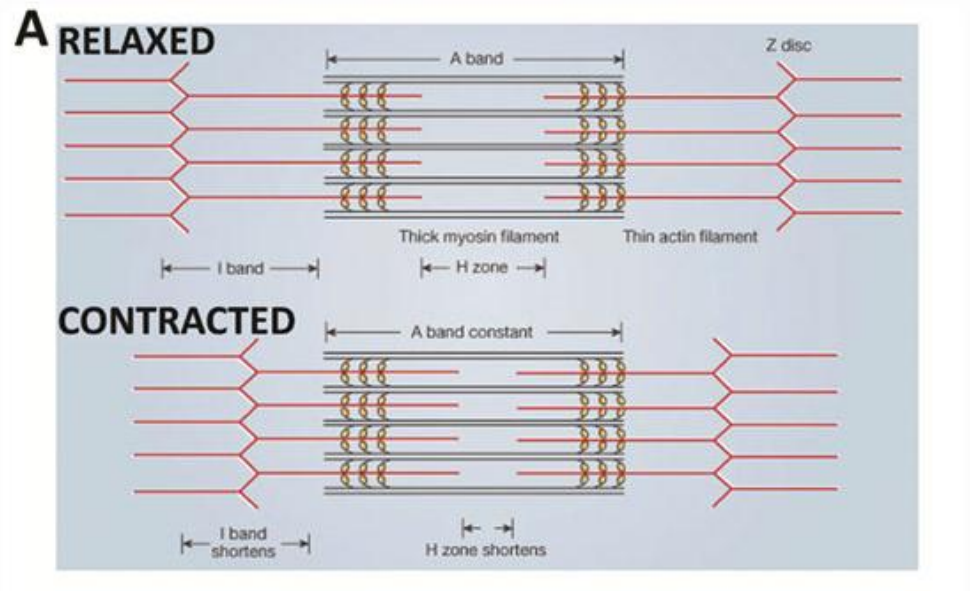

Figure 3: As seen above, relaxation and contraction within a sarcomere is depicted. Experimentation by various researchers showed that the A band (*double black lines*), which is composed of myosin filaments, remains unchanged during the relaxation and contraction of muscle fibers. In contrast, the I band (*red lines*), which is composed of actin filaments, shortens during contraction phases. These key observations lead to the overall proposal of the sliding filament theory; thus, the motion of actin filaments sliding past myosin filaments causes muscle tension [11].

In order to apply the necessary concentric and eccentric contractions to produce the desired motion, it is important to understand the effects of the muscle's fiber length, orientation, and moment arm. As previously stated, joint motion is caused by the contraction, or shortening, of the sarcomeres that make up the myofibrils within a single muscle fiber. Due to the sarcomeres being arranged in series, the total shortening that a single muscle fiber can produce is dependent on the sums of all the sarcomeres shortening lengths. Therefore, the amount a single muscle fiber can shorten is approximately 50 to 60% of the total fiber length, and the total muscle shortening length is dependent on the contracted length of each constituent fiber [12]. These fibers, however, can be oriented in various patterns depending on the muscle that affect the overall motion and force production. There are two different types of filament arrangements: parallel and pennate. Parallel filaments are oriented to be in line with the length of the muscle, and can classify the muscle as fusiform or strap. This muscle classification is based on the

prominence of the corresponding muscle's tendons. For example, fusiform tendons have tendons at both ends of the muscles, for which the fibers taper to. The opposite is true for strap muscles. This classification has less prominent tendons that the muscle does not taper to. In contrast to parallel muscles, pennate muscles have one or more tendons that extend the length of the muscle. This structure causes the fibers to attach into the tendon indirectly and at an offset angle to the desired muscles line of action [13]. The classification within this muscle group is through the number of tendons within the muscle (i.e. unipennate has one tendon the muscles attach to obliquely) [12]. Lastly, the moment arm of the muscle is known as the angle of application. This angle is defined by the insertion point to the bone, and the actuation direction of the muscle and the limb it is attached to, as depicted by figure 4.

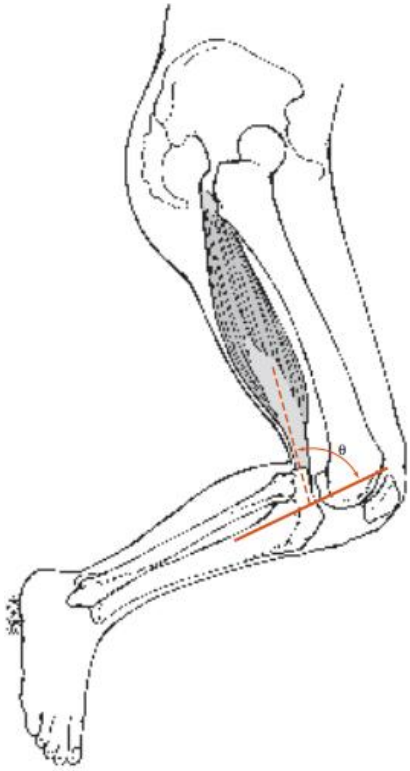

Figure 4: Depiction of the angle of application of the long head biceps femoris that has insertion points along the head of the fibula and the lateral tibia condyle. The angle is clearly depicted in orange. With the insertion point of the lower leg placed at the lateral tibia condyle, in line with muscle is the actuation direction of the muscle contraction to which the angle from the tibia is drawn. This angle is denoted within the figure as Θ [12].

Lastly, muscle force production, also known as muscle strength, is affected by muscle size, muscle moment arm, muscle stretch, contractile velocity, muscle fiber recruitment, and muscle fiber types [12]. For the purpose of this thesis and the understanding of muscle behavior

related to mechanical systems, muscle size, moment arm, stretch, and contractile velocity will be discussed, in depth.

Muscle size is the most important factor that determines the force generated during a contraction because of the cross linkage of myosin and actin filaments along the muscle fibers. Although this correlation can be a little misleading depending on the type o muscle being examined. The anatomical cross-sectional area is the area across the widest portion of a muscle and is perpendicular to the muscle's length. For parallel muscles, this cross-sectional area cuts across the majority of the respective muscle fibers. This concept does not hold true pennate muscles thought. As previously stated, this type of muscle contains fibers that are not attached parallel to the line of muscle action. This causes the anatomical cross-sectional area to not cut across the majority of respective muscle fibers. Thus, it is important to correlate the number of muscle fibers along the anatomical cross-sectional area, but it cannot be inferred that with a higher number of fibers the higher the force production, as determined by the ability of pennate muscle. In a study completed by Baratta et. al., nine load-moving muscles, from cat hind legs with different anatomical architectures, were characterized for force, velocity, and energetics [14]. Among other important characteristics from the study, the key results, in relation to muscle architecture and force production, show that muscles with high angle of pennation achieve optimal kinetic energy and maximal forces for intermediate load bearing scenarios. For parallel fibered muscles, higher maximum velocities, higher elongation, and higher kinetic energy were observed during low-load bearing applications [14]. Further observations suggest muscle performance for low-load and high-load applications is limited by elongation length to accelerate load and force available to accelerate load, respectively.

The muscles' moment arm is directly related to the distance from which the force is applied (r) and the applied contractile force along the moment arm (F_{muscle}). This is given by the cross-product equation of:

$$\vec{M} = \vec{r} \times \vec{F}_{muscle} \quad (1)$$

Equation 1: Resulting Muscle Moment of the Muscles Applied Tension and Associated Muscle Arm from Point of Rotation

From this equation, it can be determined that a larger muscle moment arm the larger the resulting moment produced. Further, the angle of application of the muscle force is extremely

important. This angle is determined through the muscle force component acting perpendicularly to the rotating body. From figure 4, this causes the true acting muscle force to be $F_{muscle}sin(\theta_{application})$, for which $\theta_{application}$ is determined by the angle the muscle makes to the attached skeletal structure being rotated. Using trigonometric principles, the maximum applied moment occurs when the angle between the skeletal structure and muscle is 90°.

As previously stated by the sliding filament theory, the cross-links formed between myosin and actin filaments change the lengths of a single sarcomere within a muscle fiber. The maximum cross-linkage between the two filaments occurs when the muscle fiber is at the resting length. In turn, this is when the muscle has the maximum contractile force. As the muscle contracts, the contracting actin filaments begin to interfere with one another [12]. This interference leads to a decrease in the cross-linkages between myosin and actin and the available contractile force available in the sarcomere. Thus, the stretch within a muscle is dependent upon the sarcomeres cross-linkage and the elasticity of non-contractile muscle components. More specifically, the non-contractile components are associated with the epimysium, perimysium, endomysium, and tendons [12]. Numerous studies have observed the effects of the non-contractile components of muscles. As a muscle stretches without any applied contraction or stimulus, the muscle will begin to apply a resistance force to any further contraction. This resistance is associated with the recoil of passive elements within a muscle, such as the connective tissue and better known as the parallel elastic components. Further, series elastic components are associated with the tendons connecting the muscle to skeletal structures [12]. These components will be further discussed in Chapter 2 and illustrated in Chapter 4.

As previously stated, three different contractions are associated with muscle movement: eccentric, isometric, and concentric. It is imperative to understand the differences between these types of muscle contractions with their respective contractile forces and contractile velocities.

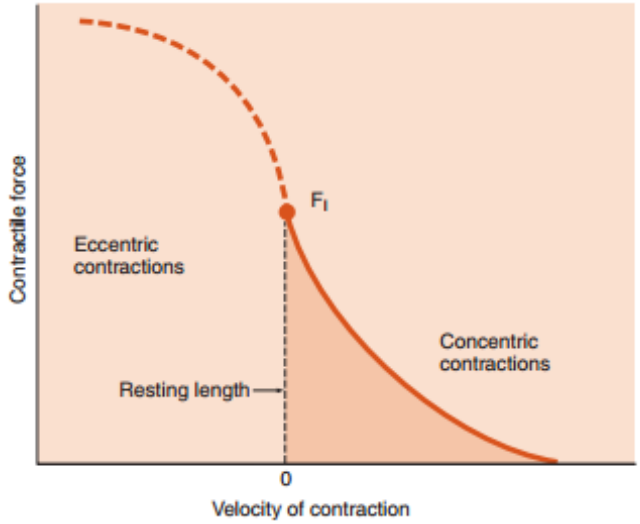

Figure 5: Comparative graph that identifies the change in force between eccentric, isometric, and concentric muscle contractions. The highest force occurs during eccentric contractions where the muscle visibly lengthens, and is the least understood contraction type. During isometric contraction, the contractile velocity is zero, but the contractile force is set at the maximum possible force that can be seen in concentric contractions. In this case, isometric contractions are denoted by a singular point, F_I. Lastly, concentric contractions, also known as shortening contractions, occur when the muscle shortening is apparent. These contractions have a higher muscle shortening velocity, but substantially smaller contractile forces to that of eccentric and isometric contractions [12].

Eccentric muscle contraction occurs as the muscle visibly lengthens. As seen in figure 5, there is a maximum eccentric contractile force that can be achieved, denoted by the plateau. However, this force produced remains much higher than that of the isometric and concentric contractile forces. Isometric can be depicted by F_I on figure 5. At this point the muscle remains at a relatively zero contractile velocity. From this point, the concentric contractions take over increasing the velocity of the shortening, but greatly decreasing the force produced.

1.3: Simple Machines of the Body

Biological musculoskeletal systems (MSK) are comparable to simple mechanical system, such as wheel and axles, levers, and pulleys. These simple machines can be and, historically, have been used to help characterize concepts related to kinetics and kinematics of the biological systems being observed. Each of these three is discussed in the following sections.

1.3.1: Wheel and Axle System

Wheel and axle systems are used to enhance the range of motion and speed within a MSK. This can be functionally comparable to the lever systems discussed previously, but as the wheel turns the axle must rotate, as well, about a designated fulcrum. This rotation must occur in such a manner that both complete one rotation at the same time. An example of this can be seen through the throwing of a ball, shown in figure 6. Biologically, the rotator cuffs of a shoulder act as the point of rotation for humerus, the axle for a bent arm. This causes the hand and wrist to be representative of an outer edge of a wheel. This structure allows minimal rotation of the rotator cuff muscles at the head of the humerus, while the wrist and hand travel a greater distance due to the increased radius from the center of rotation.

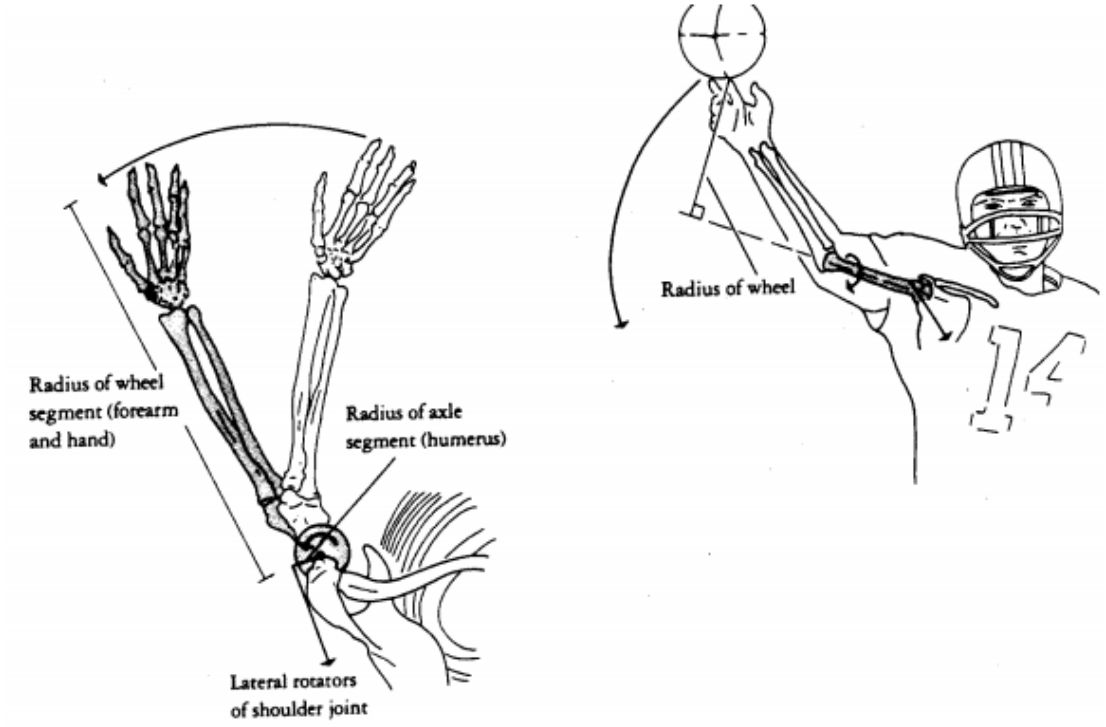

Figure 6: Biological wheel and axle configurations can be seen through the applied force of rotator cuff muscles to the humerus during the throwing of a ball. The length of the forearm and hand are the theoretical wheel radius, which have a greater range of motion than that of the head of the humerus, the inherent force application site [15].

1.3.2: Pulley System

Pulleys can be exemplified within biological MSK's. In mechanical systems, pulleys are utilized to change the effective direction for which a force is applied to enable movement of a weight or object. More specifically, when a skeletal muscle slides over a round bony surface, it is acting as a simple pulley. The knee can act as this type of simple machine when the quadricep contracts to extend the lower leg up. The muscle, connected to the patella by the quadricep tendon, pulls the patella and patellar tendon connected to the tibia.

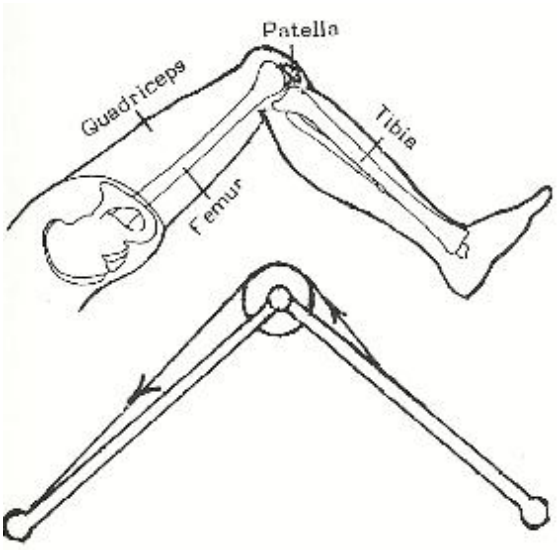

Figure 7: A pulley system within the human body can be exemplified above through the extension and flexion of the lower leg about the patella. In this case, the quadriceps contract or relax to complete the motion. When lifting the left the quadriceps contract. Subsequently, this action causes the quadriceps tendon to pull on the patella and patellar tendons connected to the tibia. This contraction overtop of the knee allows the lower leg to be lifted up similar to a pulley. The opposite is true for extension of the lower leg [16].

1.3.3: Lever System

A levers, which is created by a rigid bar that rotates about a fulcrum, is comparable to the skeletal bone structure which rotates about a joint. However, a lever at equilibrium will not rotate about a given fulcrum unless applied with a force against the systems resistance or weight. For example, a human leg demonstrates the use of a lever system within a biological application. The knee and metatarsophalangeal joints are fulcrums for which the femur and/or tibia can

rotate, as exemplified through models in figure 8. The force to move the bones about the joint is applied from the contraction and relaxation of the hamstrings, quadriceps, and triceps surae.

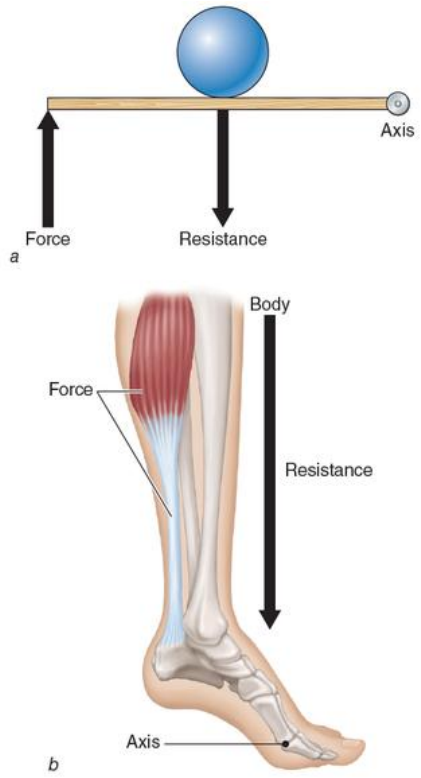

Figure 8: Top panel: An example of a simple FRA lever system. Bottom panel: lifting the body onto toes causes the metatarsophalangeal joint of a human foot to be the axis of rotation of a FRA lever system. As a result, the triceps surae applies the force to lift the resistive body weight [17].

The ability to compare MSK within the body to levers allows for the system's mechanical advantage to be characterized. Mechanical advantage, A, can be determined in relation to system forces or lengths to the system forces. In this case, the distance to the application force is l_{in}, while l_{out} is the distance to the resistive force. The governing equations for mechanical advantage are as follows:

$$A = \frac{F_{resistive}}{F_{application}} = \frac{l_{in}}{l_{out}} \quad (2)$$

Equation 2: Mechanical Advantage in Relation to System Forces and Lengths

From equation 2, the mechanical advantage of the three types of lever configurations, first-class levers (RFA), second-class levers (FRA), and third-class levers (FAR), can be determined for biological applications.

First class lever systems (RFA) are identified by having the fulcrum between the resistance and applied forces. This type of lever configuration can be understood through lifting head movement. As shown in figure 9, when lifting the head from a downward position, the neck muscles apply the force to lift opposing weight resistances of the head and inertia. These muscles are connected to the atlanto-occipital joint located at the base of the skull. This configuration clearly shows that the fulcrum is in between the resistance and applied forces. Further, a head simply being balanced on the neck is another example of this type of configuration. On each side of the head, agonist and antagonist muscles are contracting to help balance the head from falling too far forward or too far back. In this example, agonist muscles produce the force to keep the head from moving too far forward, while the antagonist muscles supply resistive forces.

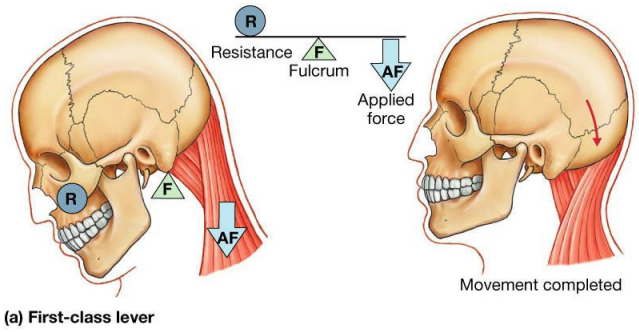

Figure 9: First class lever systems follow the general schematic of resistance-fulcrum-applied force (RFA). In this case, the action of lifting ones head from a downward looking position represents this type of lever configuration. The resistance is the weight of the head being lifted, while the fulcrum is at the atlanto-occipital joint of the skull's base. To complete the action, the cervical paraspinals and upper trapezius apply contractile forces to aid in lifting the head [10].

Second class levers are extremely critical within the body because they allow force movements, as a result of large resistances to be moved with small forces. Figure 10 shows how plantar flexion depicts the change in configuration of resistance to between the fulcrum and applied forces. The triceps surae contracts to pull the heel up off of the ground. As the heal

moves up, muscles attached at the metatarsals further stretch and contract to help balance upon the phalanges.

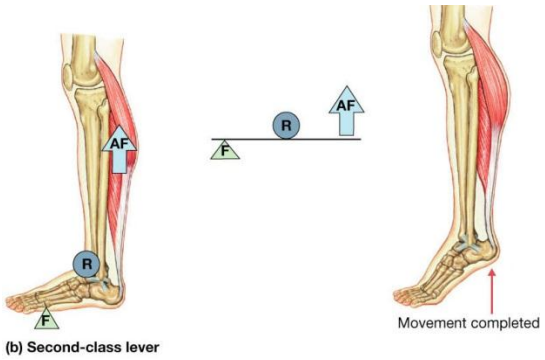

Figure 10: Similar configurations of a second class lever were previously depicted in figure 8. In general, second class levers move the resistance to the middle of the system. Plantar flexion is shown above where the body weight resistive forces act along the length of the leg. While the triceps surae contract to lift the heel, and the motion pivots at the metatarsophalangeal joint [10].

The last lever system configuration, depicted in figure 11, is known as a third class lever system. In this case, the applied force is placed in between the fulcrum and resistance. As seen in figure 11, simple bicep curls can show how this lever configuration applies to biological systems. The bicep applies contractile forces to pull upon the forearm. As the forearm moves upward closer to the shoulder, the bicep continues to apply greater contractile forces to overcome the resistance of the weight in hand. Further, in this case the elbow joint is the fulcrum to the motion of the resistance and contraction of the bicep.

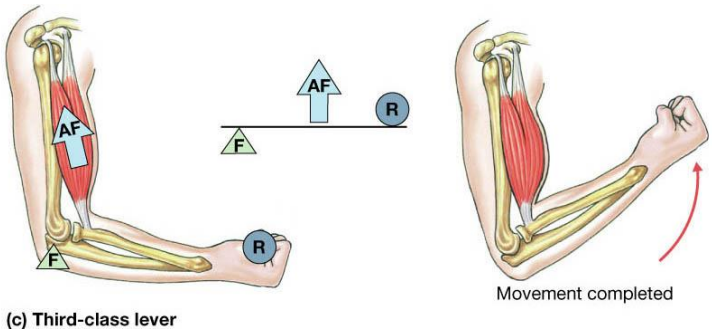

Figure 11: Third class levers, which follow the fulcrum-applied force-resistance (FAR) configuration, can be exemplified through a bicep curl contractile motion. In this case, the resistance is applied at hand. As the bicep contracts, the insertion point (radial tuberosity and bicipital aponeurosis) on the medial forearm is pulled upward, as

shown in the movement completed. This leaves the elbow joint as the fulcrum in this configuration for the contraction and resistance to pivot about [10].

Chapter 2: Mathematical Modeling of Kinetics and Kinematics Review

2.1: Characterization of Muscle Performance in Biological Systems

Although several factors may affect the force development within muscles, the performance of muscles is generally assessed on the muscle shortening rates for various loading scenarios [16]. For passive and active MSK systems, it has been long understood that the relationship between force-velocity can be modeled using Hill-type models. The original Hill equation is as follows:

$$(F + a)(V + b) = b(F_0 + a) \tag{3}$$

Equation 3: Hill Equation [18 - 20]

For this a is the coefficient of shortening heat, while F and V are force and velocity, respectively. It should also be noted that F_0 is the maximum isometric tensile force, and b is defined by the following relationship at which V_0 is the maximum contractile velocity when muscle force is zero.

$$b = \frac{aV_0}{F_0} \tag{4}$$

Equation 4: Derivation of *b* parameter for Hill's Muscle Equation [19, 20]

This equation bases muscle contraction on a single contractile component, activated by an electrical stimulus, and two non-linear springs. One spring is represented to be in series while the other is in parallel [21]. However, modifications to this equation have allowed for a series of modeling schemes to be proposed based on the same principles as those in equation 2. The majority of these enhanced modeling equations are classified as zero-dimensional because of the lack of consideration to mass and inertial body forces. This causes the output to be simplified to one-dimensional forces for crude reasons. Further, the inputs of these equations have, historically, been based on muscle-tendon-complex (MTC) length, MTC contractile velocity, and stimulation from neurons. These components are integrated into the equation through force-

length parameters, force-velocity parameters, and series and parallel elastic energy elements in manipulated configurations [22].

2.2: Modeling Techniques of Biological Systems

2.2.1: Rigid Body Modeling

In general, rigid body modeling is utilized to help simulate the locomotion of animals and humans through looking at specific portions of the body as rigid, non-deformable bodies [2]. This model assumes that joints of a body are completely frictionless ball-and-socket, hinge, or universal joints. Simplicity of the modeling scheme, to which the Hill-type models are accomplished, is thus implied when employing these techniques.

Rigid body modeling can be utilized for a multitude of applications, such as: muscle implantation effectiveness and assessment, multi-segment interaction, and performance of jumping and walking musculoskeletal systems, to name a few [2]. Raabe et. al. completed an investigation of the muscle-skeletal interactions of trunk movement during jogging to create a full body model located within OpenSim, musculoskeletal modeling software, in conjunction with three previously defined models [23]. Specifically, this modeling technique integrated Hamner's full-body model, Christophy's lumbar spine model, and Arnold's model to create the full body depiction of a human for simulation purposes. It was seen that this model was able to predict similar gait kinematics of a jogging motion related to the trunk and lower extremities of the human body, as shown in figure 12. This is crucial for understanding the loads of the lower body and lumbar spine, especially in applications of pain management and artificial implant fitting and/or characterization prior to implantation.

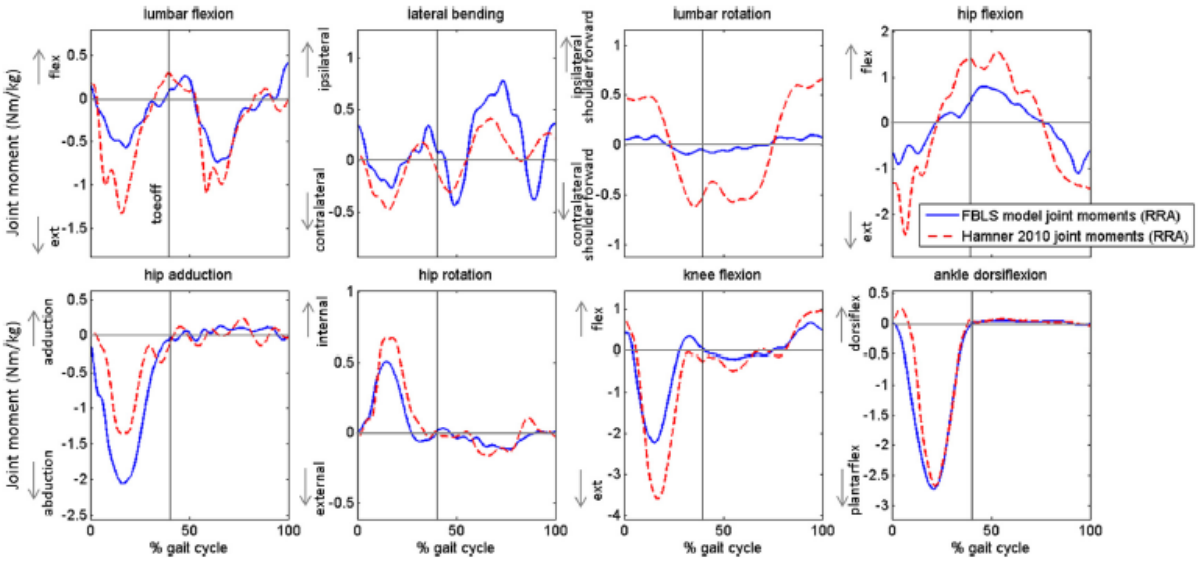

Figure 12: During a jogging motion, the trunk and lower extremities of the human body were simulated by both the full body (FBLS) model created by Raabe et. al., while compared to previous simulations completed by Hamner et. al.. In general, it can be seen that the simulation results produced by the FBLS model are comparable to those previously accomplished by Hamner et. al. However, the two simulations show kinematics of different subjects, which can account for the slight differences in the overall simulated results throughout the gait cycle. The following abbreviations were utilized by Raabe et. al.: extension (ext), flexion (flex), plantarflexion (plantarflex), and dorsiflexion (dorsiflex) [23].

It should be noted that the simulated model involved the use of 21 segments, 30 degrees of freedom, and 324 musculoskeletal actuators, which is simpler in design than other full body models. Given that the model created by Raabe et. al was compared to a model of 0 degrees of freedom (Hamner's model) in figure 12, it is promising that this model can be used to, somewhat, accurately describe trunk and lower extremity loading scenarios based on the joint movements. However, making a model to accurately predict an individual's precise motions is limited due to the lack of anatomical data, and variance between anthropometric data.

Works completed by Monsabert et. al. provide further exemplification of rigid body modeling in relation to muscle force production of hand grips and simulations of the motion being done [24]. Physical experimentation of healthy patients was initially conducted to understand force analysis of two gripping tasks (power grip and pinch grip), kinematics of the joint movement, and MRI measurements of the healthy hands. A previous hand model was employed, to use the hand modeled as a rigid body, frictionless joints, 23 degrees of freedom,

and 42 musculoskeletal actuators. Muscle tension was predicted through the use of equations 5, 6, and 7 below.

$$[R] * \{t\} + \{m_L\} + \{m_f\} = \{0\} \tag{5}$$

Equation 5: Muscle Tension [24]

Equation 5 cannot be solved without the use of the "muscle-stress" criterion stated in equation 6 as:

$$min \sum_m \left(\frac{(t_m)_s}{PCSA_m}\right)^n \tag{6}$$

Equation 6: "Muscle Stress" Criterion [24]

Once the muscle tension was achieved through the use of equations 5 and 6, the joint forces could be estimated. This estimation is achieved through the use of the joint reaction forces, muscle tension, experimental grip forces, and passive MCP collateral ligament forces. Equation 7 represents these components to calculate the joint forces.

$$\{J_R\}_j + \sum_m \{T\}_m + \sum_a \{F\}_a + \sum_l \{L\}_l = \{0\} \tag{7}$$

Equation 7: Joint Force Estimation [24]

As a result of this study conducted, it was seen that a significant relationship is present with the effect of grip and joint for the index and thumb with relation to the joint forces. Further, during the pinch grip and power grip tasks, the forces exerted were 60N and 130N each, respectively.

Although this technique is successful and helpful, there are drawbacks. First, the simplicity of the simulated joints is not ideal or comparable to natural, biological joints. Second, prediction calculations of the kinematics of musculoskeletal systems with a lack of multiple inputs are a challenge that remains. Through the determination of compliant artificial muscle actuators, experimental and theoretical data can be determined to create viable simulation methods for biological muscles.

2.2.2: Inverse and Forward Dynamic Modeling

Inverse and forward dynamic modeling techniques are extremely common in attempting to calculate various musculoskeletal movements of muscle/joint forces/torques. Inverse techniques look at the joint positions during the movement. These movements are then differentiated to acquire the velocities and accelerations of the motion, and utilized to find forces and torques of a given body. Inverse dynamics modeling is valuable due to the simplistic nature, and quasi-experimental results. However, the downside of this modeling requires further optimization for understanding and exploration of muscular contributions, and restricts the ability of theoretical scenarios to be simulated. Basafa et. al. utilized inverse dynamics modeling to identify methods of better facial implantation planning through the use of inverse dynamics simulations with swine specimen [25]. Overall, inverse dynamics modeling techniques were relatively similar with experimental data of swine mastication. However, moving forward, theoretical simulations and experimental data need to be completed hand in hand with the same specimen to identify better congruency between the two methods.

Alternatively, forward dynamic modelling is the opposite of the inverse dynamic technique. In this case, muscular movements are directly characterized through theoretical simulations. This allows for muscle torques to be identified through the forces and muscular moment arms. Subsequently, the acceleration, velocity, and position can be determined. Although this modelling technique can help predict the muscle performance from various individuals and provide a valuable design tool, there are several disadvantages. First and foremost, this modelling is not based on experimental data, such as the inverse dynamic models. It also can use parameters that are not necessarily easy to obtain or estimate, especially those related to individual muscle parameters. Lastly, this technique is restrictive in the simulations being evaluated. For example, only simplistic patient locomotion and muscle movement scenarios can only be simulated.

Combinations of inverse and forward dynamics models, such as inverse-muscular forward-skeletal dynamics and forward-muscular inverse-skeletal dynamics have been explored. Sharif Shourijeh et. al. studied inverse-muscular forward-skeletal dynamics for creating at 2-dimensional full-gait, human model [26, 27]. Optimization was required during each of the simulations, to help provide proper outcomes of the calculations, which can be seen through

figure 13. Through this combination of modelling, it was determined that lower extremity kinematics, muscle activation, and ground reaction forces through the two step gait cycle simulated were congruent with experimental results during gait.

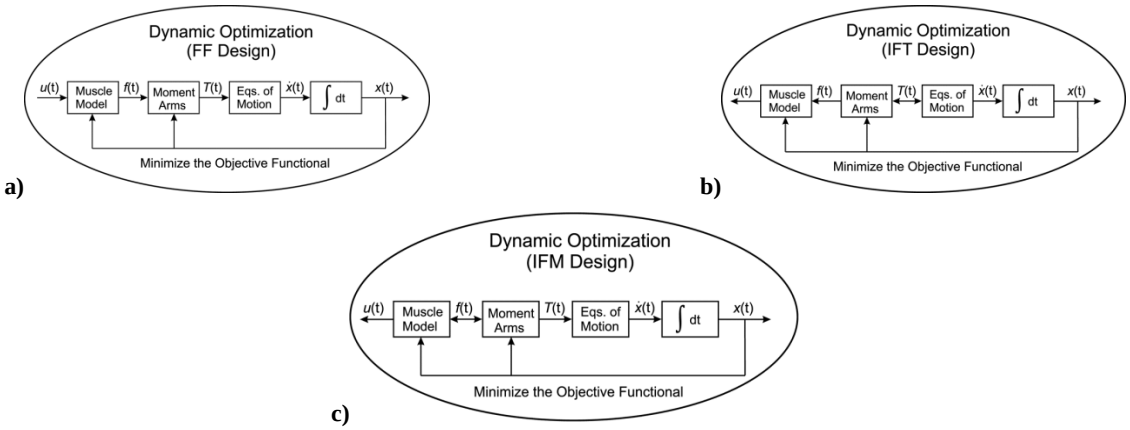

Figure 13: Dynamic optimization is utilized by many studies that employ forward and inverse dynamics modelling of musculoskeletal systems. Sharif Shourijeh et. al. completed simulations for: **a)** fully forward (FF), **b)** inverse-forward starting at joint torques (IFT), and **c)** inverse-forward starting at muscle forces (IFM). The schematics for each follow the same design; however, the forward dynamics approach requires the initial muscle activations and lengths to complete the simulation. For the simulations proposed by IFT and IFM, utilized inverse dynamics for which the simulations solved for joint torques and activation of muscle-tendon force and length, respectively [26].

On the other hand, Lloyd et. al. utilized a forward-muscular inverse-skeletal dynamic method to estimate the muscle forces of knee joints [28]. In general, electromyography (EMG) driven models were utilized to predict the muscular moment of human knees through the use of inverse dynamics. Physiological based parameters, such as those related to muscular set-up, were obtained through specific patient parameters, in order to measure the muscle moments to the skeletal system through inverse dynamic calculations. Through this experimentation, it was determined that EMG driven models can accurately predict the muscle moments, when calibrated to specific patients.

2.2.1: Finite Element (FE) Modeling

Finite element modelling, along with musculoskeletal rigid body modelling schemes, has been historically used to help provide information of loading scenarios at joints during dynamic

activities. This is crucial in understanding joint interactions during normal locomotive actions of various specimens.

Fitzpatrick et. al. [29] experimented with joint loading ratios of internal-external to compression and anterior-posterior to compression force ratios were estimated to help aid design and implantation modelling of total knee replacement devices and surgeries. This study, even though utilizing different methods than those presented previously, proved to show that it is imperative to have accurate data to that of patients with specific loading scenarios seen in vivo. Although they use telemetric data from patients, the availability of information is generally scarce.

2.3: Modeling Techniques of Jumping in Biological Systems

The mechanics of jumping have been studied extensively to understand the energy storage within animal legs, and take off velocities. One of the governing equations of this type of locomotion is as follows:

$$U = \sqrt{\frac{2\Pi}{m_{body}}} \tag{8}$$

Equation 8: Instantaneous Take-off Velocity of Jump [30]

In this case, velocity is correlated to an animal's legs and body mass with relation to the stored energy per unit of body mass, denoted by Π [30]. Understanding these components allows for the calculation of maximum attainable jump height, assuming no losses to surrounding fluid and all kinetic energy is changed to gravitational potential energy. The maximum height of the jump can be determined as that shown in equation 9.

$$H = \frac{\Pi}{m_{body}g} = \frac{U^2}{2g} \tag{9}$$

Equation 9: Maximum Height of Jump Attainable [30]

Understanding that the stored energy per unit of body mass, Π, has been explored by Bennet-Clark who proposed that the number of this parameter is roughly 20 J/kg [30]. From this, it can be determined that the maximum height of a jumping animal is not a function of the animals mass or length, due to the interpreted relations of equation 8 into equation 9. However,

the maximums, of both velocity and height, are greatly dependent on the stored energy per unit of body mass. In relation to muscle gearing, this energy based approach brings up an interesting point of view; there must be an optimal muscle shortening velocity to maximize power produced from the muscle, and maximize the take-off velocity, *U*. In this case, this maximum power produced causes the velocity at take-off to be maximized and, subsequently, the jump height to be maximized.

Gregersen and Carrier, completed a study that: 1) calculated the gear ratios of canine extensor muscles of major limb joints to verify signs of increasing gear ratios during jumping, 2) measured length changes of the extensor muscles that exhibited this increasing gear ratio, and 3) computed the contributions of this increasing gear ratio joint to the overall work produced during the jump [31]. This study defined the gear ratio as the out-lever length of the ground reaction force moment arm (distance to the application force) divided by the in-lever of the muscle moment arm (distance to the resistive force), similar to that provided by equation 2.

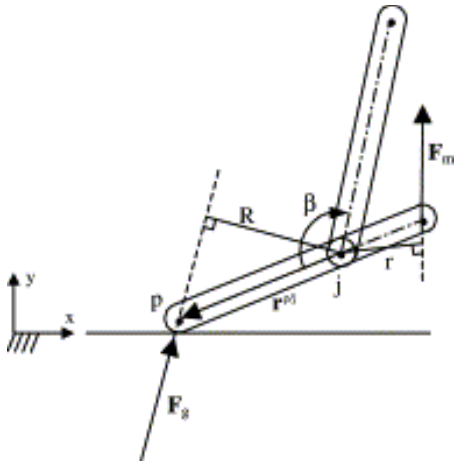

Figure 14: The simplified limb segment utilized for calculating the gear ratio of canine jumps is shown. R represents the ground reaction force moment arm, while r is for the muscle moment arm. Further, the following variables are defined as such: β is the angle of the joint, p is the center of pressure, j is the center of the joint, $r^{p/j}$ is the position of the center of pressure, and $F_g$and F_m are the force vectors of the ground reaction moment and muscle moment, respectively [31].

As a result of this study, it was seen that in the canine knee and shoulder joints, there is gearing that matches the original theory that at some point there is an optimal gearing ratio to produce maximum power output from a muscle as it shortens. This is depicted below in figure 15, as the contact time increases on the force pad, the gearing ratio of knee and shoulder begin to

increase greatly in a somewhat linear fashion as the joint extends during the initial jump [31]. Further, Gregersen and Carrier studied the length changes of the canine's vastus lateralis, a muscle of the hind leg. It was seen to undergo shortening of 17 to 29% of the standing length at rates of 2.7 to 3.8 muscle lengths per second, and was observed to be relatively constant for two of the canine subjects. From previous studies, it was determined that the observed shortening length is approximately 30% of the maximum shortening velocity, and suggests that the maximum shortening velocity is approximately 10.7 muscle lengths per second. This is similar to studies that predict the maximum shortening velocity to be 12.5 muscle lengths per second. These findings and observations help confirm that there is an optimum of muscle gearing to produce maximum power output in a jumping system [31].

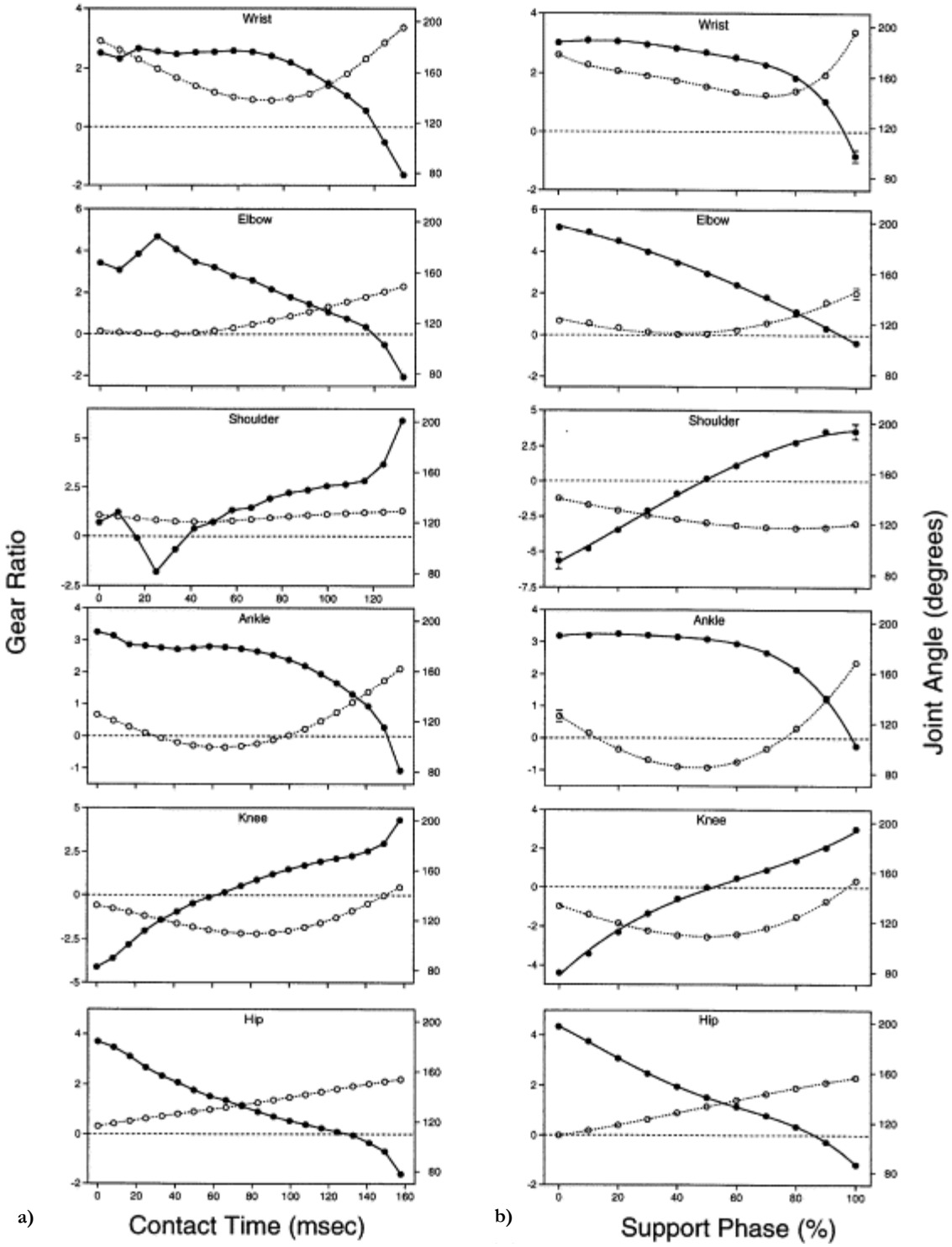

Figure 15: The wrist, elbow, shoulder, ankle, knee, and hip joints of three different canines were examined during a jump. Dark solid lines represent the gear ratios, while the light dashed lines represent the joint angle. These are both shown in correlation to the contact time and support phase of the jumping motion. In these graphs, the data of **a)** comes from a single canine specimen, while **b)** comes from the means and standard deviations of all three canine.

Further, gear ratios above zero show positive muscle moments during extension, and decay of joint angles show flexion of the joint [31].

One major implication to this theory of muscle gearing though is the fluid mechanics around the animal jumping in question. For larger animals, the medium for which their primary locomotion occurs does not greatly affect the overall height and body length jumping ratio. For smaller animals, this is a large consideration where drag is a large factor in the overall jump [30]. In relation to locomotive performances, based on force and velocity outputs, this is a point of argument. It has been heavily understood that there is an inherent trade-off between force and velocity of musculoskeletal systems. However, arguments related to this theory, on the basis of absolute velocity and force, are proposing that there is no such trade-off. Theoretical modeling is accomplished below to help observe this new contradictory claim.

2.4: Modeling Techniques that Consider Environmental Conditions on Locomotion

While previously discussed research targets the anatomical structure, biological reaction, and physiology to understand motion of organisms through specific actions, the effects from the environment are relatively substantial on the performance of a MSK. This can be initially exemplified through studies of guinea fowl funning over unpredictable terrain that requires the animal to compensate for unexpected changes in height through either dissipating or converting energy. Daley et. al provided camouflaged terrain to understand the muscle control during sudden drops in terrain height [32]. It is suggested that three outcomes can be possible: 1) the sudden drop is fully compensated for to maintain the steady, spring-like route without any net changes in energy components (i.e. E_p, E_{Kh}, E_{Kv}) 2) change in E_p, total potential energy, was converted to change in totally kinetic energy to increase the velocity, while still following conservation of mass-spring dynamics, and 3) change in E_p results in change in center of mass energy and is absorbed through negative work. It was observed that although the guinea fowl were able to maintain stability throughout the unexpected height changes, delays in the muscular loading and decreases in the muscular tension occurred. This suggests that there is a connection between the actuating system and the environmental conditions associated with it. Most

importantly, this verifies that the effects on the mechanical output and system movement do not relate only to the biological system responses, but environmental factors.

Continuing observations related to environmental conditions, Richards aimed to understand the effects of environmental factors through the experimentation of frog leg muscle activation. Male *Xenopus laevis* , an aquatic frog, were dissected to obtain the plantaris longus (PL) muscle. Two test fixtures were then made. The first related to the robotic leg, to be activated through PL muscle activation, and a 'work loop' ergometer, to measure *in vitro* muscle data. The robotic foot was actuated within air, for inertial loading cases, and water, for hydrodynamic exploration. Various gearing multipliers, essentially gearing ratios, were used to observe changes in gearing ratio of the force and displacement data within the software feedback loop [33]. These changes and conditions allowed for loading, gearing multiplier, and foot size to ultimately be tested. Environmental loading cases, between inertial and fluid effects, demonstrated that an immersed robotic foot would produce forces to mainly overcome the hydrodynamic drag, in addition to the mechanical and hydrodynamic inertial forces. Additionally, peak force and shortening velocities were observed with the fluid cases. However, muscle work output between the cases remained fairly consistent, with 5.30 ± 2.12 and 6.67 ± 2.93 $\frac{J}{kg}$ for air to water cases, respectively, while net power output was higher within the air trials [33]. The force-length dynamics were sensitive to any gearing ratio change, in addition to the effects of gearing between inertial and fluid cases. Increases in gearing, significantly decreased the shortening velocity, but increased the power output in the air loading cases.

In general, from the experimentation of Richards, it was concluded that peak forces seen in the hydrodynamic cases are much more sensitive to the muscles intrinsic force-velocity relationship, as opposed to those seen within the inertial loading cases. Further, changes in anatomical structure of a limb, not only decrease or increase the velocity per the loading scenario, but are directly dependent upon the mechanical advantage of the system [33].

Chapter 3: Problem Statement

Since the early 1900's, it has been understood, and accepted, that with small mechanical advantages (ratio of in-lever length to out-lever length) produce fast movements with small application forces. Conversely, large mechanical advantages produce slow movements with larger forces, as explicitly stated by Smith and Savage [34, 35]. This relationship is regularly used in interpreting function and performance of MSK systems of locomotion, evasion, and feeding. Further, numerous groups have exemplified understanding of MSK function and performance through studies with the objective to understand evolutionary enhancements of species ability to capture prey [36-40]. However, these studies are divided between observing a trade-off in the force-velocity relationship that is widely accepted, versus not. Although the above research areas have targeted feeding habits of various species, locomotion of organisms has also been a primary research field.

In 2010, modeling works of locust hind legs, by McHenry, challenged this perception of mechanical advantage to the force-speed relation [35, 36]. It is stated that there is no trade-off between the force and absolute speed of the system due to the inability to fix the rate of shortening of the actuator (muscle or biological spring), and the change in geometry of the system being observed. This research focuses on developing a theoretical system model and experimental model to validate the longstanding characterization of musculoskeletal systems.

The objectives of this research topic were:

- Develop a mathematical system model for various actuators and loading scenarios
- Identify and design modifications to an existing McKibben air muscle test fixture
- Implement and integrate modifications to study various loading cases and environmental conditions and validate theoretical data
- Identify, from an engineering perspective, the relationship and effects of load, gearing, and actuator type on the force-velocity curve of dynamic lever systems

The system model was created from locust leg geometry that consists of a muscle, rigid upper leg bone, knee joint, and rigid lower leg bone geometry. A simple schematic of this geometry can be observed in figure 16. The model was implemented using Simulink, a

graphical programming environment for modeling within MATLAB, and the ODE45 solver. This model allowed for the addition of various actuators to be implemented and various force scenarios to be observed. Schematics and additions to the generalized model of figure 16 will be presented in Chapter 4 for each case and loading scenario. It should be noted that the upper and lower leg links move as one body, when applied with the actuator force. Further, this modeling method enabled various components of the theoretical cases to be observed individually for contributions to the overall leg kick.

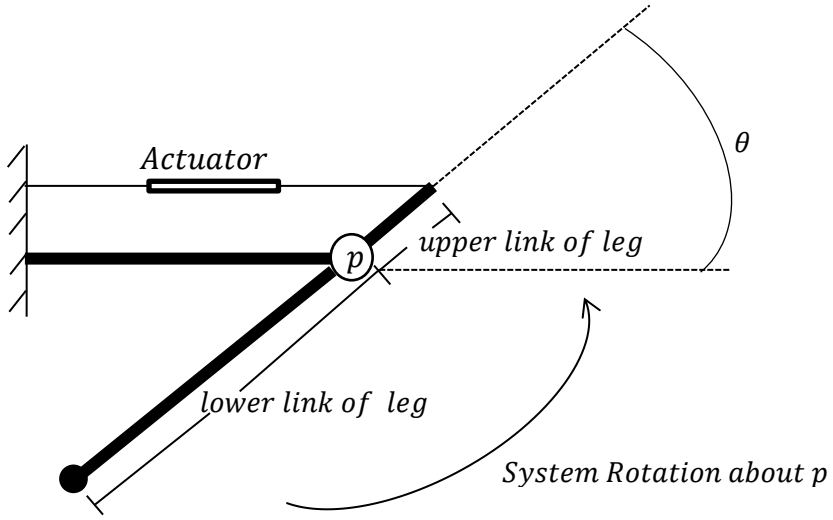

Figure 16: Generalized Locust Leg Geometry for Various Loading and Actuator Case Scenarios

Experimentation was accomplished on an existing test fixture used to observe the compliance and comparability of McKibben air muscles to biological muscle through the force-velocity relationship curve. Modifications were made to allow for force, inertial, and viscous loading cases to be observed, while using a damper in parallel with the existing McKibben air muscle. Collection of the data was accomplished with a previously designed LabView code and interface that allows for the data to be collected in an Excel spreadsheet for post-processing. Although this experimentation does not directly correlate to a dynamic lever system, it demonstrates the ability to utilize a commercially available pneumatic air muscle, in conjunction with a damper, under varying loading scenarios to determine the usability of such a test fixture for musculoskeletal characterization. In addition to characterizing varying loading

cases, the damper and pneumatic air muscle system can be tuned to create different "muscles" to be tested under varying loading conditions. A simple schematic of the system, without relation to a specific loading scenario, is shown below in figure 17.

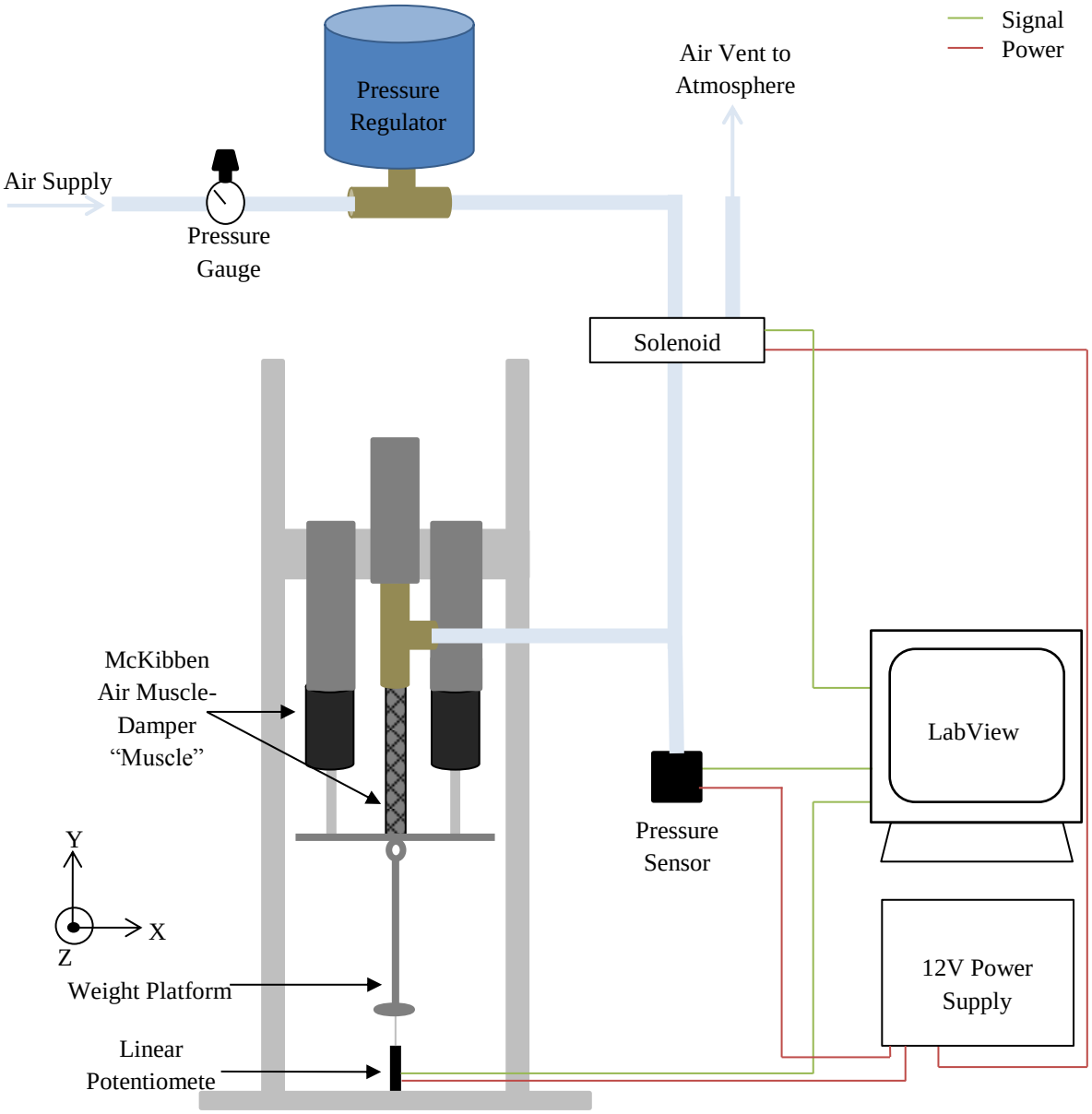

Figure 17: Simple Schematic of Experimental McKibben-Damper Muscle Test Fixture

Later in Chapter 5, modifications for varying loading conditions will be presented and depicted, but will still follow the generalized schematic presented in figure 17.

Chapter 4: Musculoskeletal Theoretical Model

The mathematical model was developed in MATLAB (R2015b) using Simulink. Simulink model configuration parameters were set to solve for the solution using a variable time-step with ODE45. Each simulation was set to run for 1 second, but depending on the angular displacement, the simulation would stop before getting to this time. This is due to a built-in conditional parameter within each of the Simulink block diagrams. Looking at the generalized geometry of figure 16, it is not possible for the rotating leg to exceed an angular displacement,θ , of 180°. With this being known, a conditional stop was placed within the derived block diagrams for each case. As the solution iterates for each time-step, the value of the angular displacement is checked against the maximum angular displacement parameter of 180°. If the solution in the time-step exceeds 180°, then the solver stops. Further, within the MATLAB code, a correction was made for the data coming from the Simulink block diagram. The last data point, within each relevant variables data vector, exceeds 180° prior to the simulation stopping. A for-loop was created in MATLAB to correct all relevant variable data vectors by deleting the last data point. Further, the relative tolerance and absolute tolerance for ODE45 were set to $1e^{-8}$ for each simulation. This allows for better accuracy and error of integration, in this case from $\ddot{\theta}$ to θ, throughout the simulation. More specifically, absolute tolerance refers to the point at which anything smaller than the set threshold value does not need higher accuracy. At this point, the simulation assumes there is no need for higher accuracy, as it can be assumed these values are so small they represent zero. Relative tolerance, on the other hand, is the error of the integration within a single time-step. Given that each case deals with integrating twice in one time-step, the error needs to be minimized. Each iteration not only compounds integration error for a single step, but all subsequent time-steps.

The models were derived from the generalized geometry previously proposed by figure 16. As the models started off simplistic, they began to increase in complexity, until the inertial loading, reactant force loading, and viscous force loading cases were obtained and quantified in a graphical manner. Below the models are presented and discussed by each case, and the governing equations are identified.

4.1: Case 1: Constant Applied Force

Case 1 is the most simplistic of all the models. It begins with the base geometry shown in figure 18, but has a constant force applied as the comparable muscle actuator as shown in figure 16. The purpose of creating this model schematic as a first step helped to identify how the system, built within Simulink, reacts under a constant, controllable force. In this case, it was hypothesized and observed that the model has a constant force throughout the actuation time of the model.

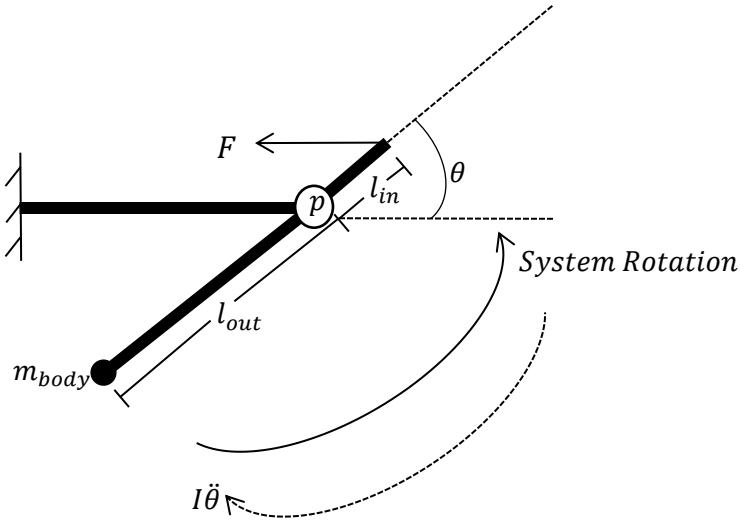

Figure 18: Model schematic of case 1, which has a constant controllable force applied at the top of l_{in}. When the force is applied, the lower leg, consisting of l_{in} and l_{out}, rotate in their fixed positions around the knee joint. This knee joint is depicted by the white circle attached to the rigid link defining the upper leg.

From figure 18, the governing equation of the system is derived by summing the torques of the system about the pivot point, p.

$$I\ddot{\theta} = F\,sin(\theta)\,l_{in} \tag{10}$$

Equation 10: Governing Equation of Constant Force Applied (Case 1)

The system has an initial angular displacement of 6°, this consideration is noted by resolving the applied force, F, for the y-component, given by $Fsin(\theta)$. Further, the force of the system is relatable to a spring force by being determined through equation 11:

$$F = kL \tag{11}$$

Equation 11: Constant, Controllable Force

, where L is defined the by spring stretch, *sstretch*, of 1.5e^{-3}m that is measured from the rigid wall. It should be noted that with this simulation, the mass of the leg was treated as acting about the base of the lower leg distance, l_{out}. In this case, the moment of inertia was based on the rotation of a rod about the end.

$$I = \frac{m_{body} l_{out}^2}{3} \tag{12}$$

Equation 12: Moment of Inertia for a Rod

In applying this moment of inertia, it is assumed that the geometry of the leg, other than in viscous loading simulations, is deemed to be unimportant in the overall modeling of the locust leg kick. The key parameters moving forward are in relation to the characterization of the muscle actuator proposed (i.e. spring and spring-damper actuators), the weight applied to the muscle for inertial consideration, and external forces (i.e. reactant and viscous forces).

As previously stated, the constant, controllable force was defined by the spring stretch length, which is the maximum length the spring can be stretched in these models. Although, in this model it is not truly representative of a muscle behavior because the force does not die out over the duration of the kick, it was important to help define, L, for the subsequent models and performed in Case 2a.

4.2: Case 2a: Spring Muscle Force in terms of l_{in}

In order to determine the proper expression for L that relates it to the change in position of l_{in}, it is necessary to look at the change in geometry through a series of key angles, 0°, 90°, and 180°. As depicted in figure 19, the maximum stretch possible for the muscle in this orientation occurs when the angle between l_{in} and the horizontal axis. For these simulations the maximum stretch was correlated to $2l_{in}$, and is equivalent to the spring stretch value of 1.5e^{-3}m

previously used in Case 1. It should be noted for the initial stages of this case, the lower leg, l_{out}, is not taken into consideration for the derivation of L, but is utilized within the simulation for inertial contributions.

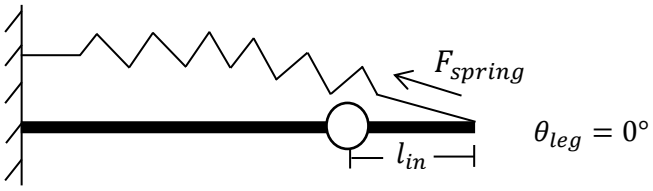

Figure 19: Spring Stretch at Maximum Length of $2l_{in}$ when Initial Angular Displacement is 0°

Further looking at the relaxed state of the spring, the stretch is required to be 0m. This is a key factor into the derivation of the equation for L, and helps signify the importance of the angular displacement of l_{in} during the kick. As seen above for the maximum spring stretch consideration and figure 20 for the requirement of the spring stretch to be 0m at 180°, the spring force is resolved only for the forces along the y-direction.

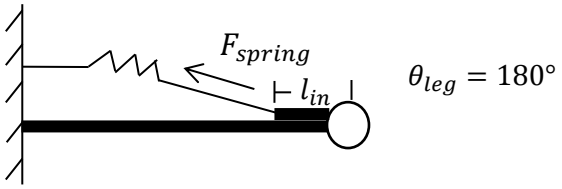

Figure 20: Spring Stretch at Maximum Rotation Allowable (180°) where Spring Stretch is 0m and Spring Force is 0N

However, the length for the stretch must be resolved in x-direction because of the orientation to the leg. This causes the length to be associated to $\cos(\theta)$ for each of the two cases presented with the derived equation as follows:

$$L(\theta) = l_{in} + l_{in}\cos(\theta) \tag{13}$$

Equation 13: Derivation of Spring Stretch with Relation to Upper-Leg Angular Position

This equation can be verified along with the two previous scenarios suggested for maximum and minimum stretch through the following simple hand calculations:

Scenario 1: Maximum Stretch at Minimum Angular Displacement of Leg:

$$L(0°) = 2l_{in} = l_{in} + l_{in}\cos(0°)$$

$$L(0°) = 2l_{in} = l_{in} + l_{in}(1)$$

$$L(0°) = 2l_{in} = 2l_{in}$$

Scenario 2: Minimum Stretch at Maximum Angular Displacement of Leg:

$$L(180°) = 0 = l_{in} + l_{in}\cos(180°)$$

$$L(180°) = 0 = l_{in} + l_{in}(-1)$$

$$L(0°) = 0 = 0$$

Lastly, an intermediate step can be taken to represent the leg as it moves through 90° to verify further that equation 13 holds true for all angles along the kicks angular trajectory. Figure 21 shows the simple schematic to represent this intermediate scenario.

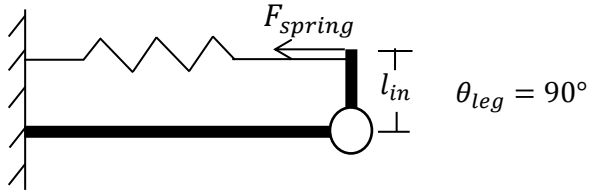

Figure 21: Intermediate Scenario Schematic of Spring Stretch Derivation

It can be inferred from the previous scenarios that the angular displacement of the leg at 90° represents the halfway point of the kick motion and energetics. Thus, the stretch of the spring should be equivalent to l_{in}. This hypothesis can be verified through the following hand calculations:

Scenario 3: Intermediate Step with Half the Maximum Stretch and Half the Maximum Angular Displacement of the Leg

$$L(90°) = l_{in} = l_{in} + l_{in}\cos(90°)$$

$$L(90°) = l_{in} = l_{in} + l_{in}\cos(0)$$

$$L(90°) = l_{in} = l_{in}$$

The remainder of Case 2a follows a similar format to Case 1, other than the representation of the force actuator as a spring rather than a constant applied force. This changes the governing equation to be defined as:

$$I\ddot{\theta} = F_{spring} \sin(\theta)\, l_{in} \tag{14}$$

Equation 14: Governing Equation of Constant Force Applied (Case 2a and 2b)

, and the force of the spring, F_{spring}, is defined by that given previously as just a constant controllable force in equation 10. The case schematic is illustrated below for reference.

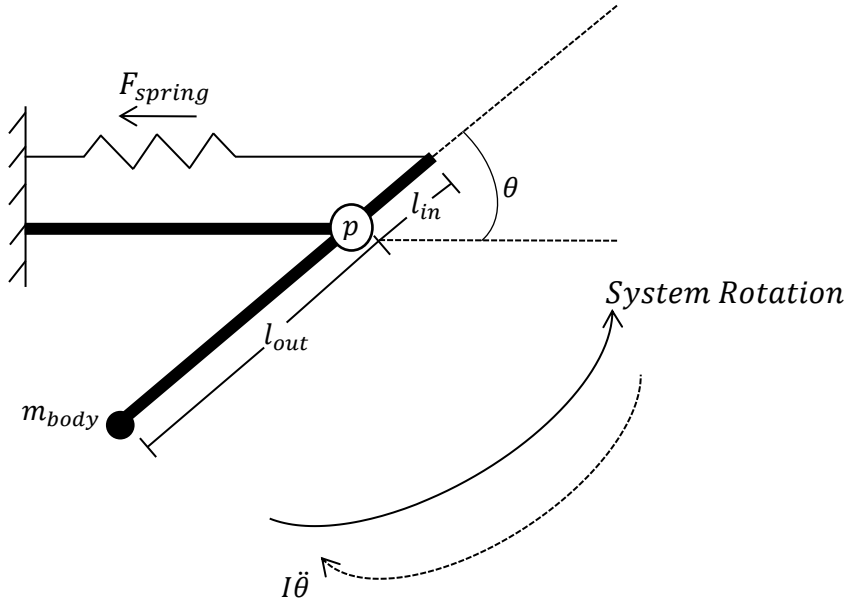

Figure 22: Schematic of Case2a and Case 2b with an applied spring as the mode of actuation is given. The spring attaches at the top of the upper leg, denoted by a length of l_{in}. As the spring applies a force, due to its maximum stretch at the initial 6° angular displacement of the upper leg, the rotational component associated of both the upper and lower leg, denoted by a length of l_{out}, rotate about the pivotal joint connection between the two anatomical structures.

The main drawback of this case is the correlation of the spring stretch to the length of the upper leg, l_{in}. The key purpose of this thesis is to understand the effects of mechanical advantage, or gearing, within a simple lever system. For this system, when l_{in} is increased or decreased in numerical length value the spring stretch is affected. Graphical results and

discussions will be presented later, but this dependent relationship between the spring stretch and mechanical advantage are corrected for in the subsequent Case 2b.

4.3: Case2b: Spring Muscle Force in terms of θ

As previously discussed, the maximum length of the spring stretch is related, numerically, to 1.5e^{-3}m. In order to get the spring stretch equation, equation 13, independent of the l_{in}, this value needs to be utilized. Since l_{in}, is exactly half of this maximum stretch value then the two can be related by the following correlation:

$$sstretch = 2l_{in}$$
$$\frac{1}{2}sstretch = l_{in}$$

, which can be replaced within equation 13 derived in Case 2a. This allows for the new spring stretch equation to be defined as:

$$L = \left(\tfrac{1}{2}sstretch\right) + \left(\tfrac{1}{2}sstretch\right)\cos(\theta) \tag{15}$$

Equation 15: Redefined Equation 14 for the Spring Stretch Length during a Kick without l_{in} Dependence

Equations 15 can be tested to hold true for all of the constraints previously determined for the stretch of the spring actuator throughout the simulated kick.

Scenario 1: Maximum Stretch at Minimum Angular Displacement of Leg:

$$L(0°) = 2l_{in} = \left(\frac{1}{2}sstretch\right) + \left(\frac{1}{2}sstretch\right)\cos(0°)$$
$$L(0°) = 2l_{in} = \left(\frac{1}{2}sstretch\right) + \left(\frac{1}{2}sstretch\right)(1)$$
$$L(0°) = 2l_{in} = sstretch$$

Scenario 2: Minimum Stretch at Maximum Angular Displacement of Leg:

$$L(180°) = 0 = \left(\frac{1}{2}sstretch\right) + \left(\frac{1}{2}sstretch\right)\cos(180°)$$

$$L(180°) = 0 = \left(\frac{1}{2}sstretch\right) + \left(\frac{1}{2}sstretch\right)(-1)$$

$$L(180°) = 0 = \left(\frac{1}{2}sstretch\right) - \left(\frac{1}{2}sstretch\right)$$

$$L(180°) = 0 = 0$$

Scenario 3: Intermediate Step with Half the Maximum Stretch and Half the Maximum Angular Displacement of leg

$$L(90°) = l_{in} = \left(\frac{1}{2}sstretch\right) + \left(\frac{1}{2}sstretch\right)\cos(90°)$$

$$L(90°) = l_{in} = \left(\frac{1}{2}sstretch\right) + \left(\frac{1}{2}sstretch\right)(0)$$

$$L(90°) = l_{in} = \left(\frac{1}{2}sstretch\right)$$

Following, similar simulation schemes as Case 2a and the schematic in figure 22 are utilized for the remainder of this case. However, up until this point the actuator utilized within the simulation is not truly representative of a theoretical muscle. As proposed earlier, Hill-type muscle models involve the use of two springs, one in series with another in parallel to the contractile element, as represented below in figure 23.

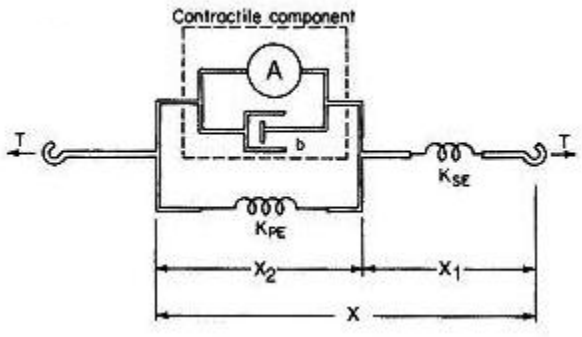

Figure 23: Representation of a Hill-type muscle with all components visualized. There are two springs within the system, one being in series (K_{SE}) and the other being in parallel (K_{PE}) to the contractile component. The contractile component is composed of a damping component with damping coefficient of b and a muscle stimulus component. When this component fires, the muscle actuates through the contraction and elongation of muscle fibers within the muscle [19].

Since, this model lacks the use of a force damping element, the next iteration of simulations employs the use of damper in parallel with the spring actuator presented in Case 2a and Case 2b.

4.4: Case 3: Spring – Damper Muscle Force

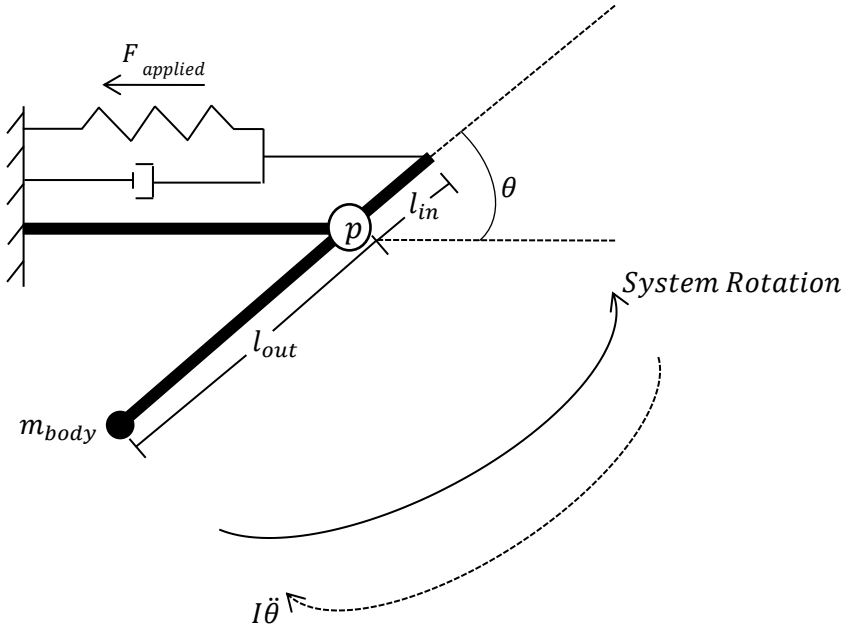

Figure 24: Case 3 problem schematic with an applied force composed of a spring and damper in parallel to represent the muscle actuator. Similarly to previous case schematics, the rotation occurs about the pivot joint connecting the upper leg to the lower leg. The mass acting at the base of the lower leg is still considered to be a point mass that only adds to the effects of the applied moment of inertia about the pivot joint.

For this case to be more representative of a muscle actuator, an energy producer and energy absorber are placed in parallel as a spring-damper actuator, illustrated above in figure 24. Due to the addition of the damper in parallel, the governing equation, therefore, becomes the following:

$$I\ddot{\theta} = F_{applied} sin(\theta) l_{in} \tag{16}$$

Equation 16: Governing Equation of Applied Spring-Damper Muscle Force (Case 3)

, where the applied force, $F_{applied}$, is the addition of the spring force,F_{spring}, previously defined, and damper force,F_{damper}, given by:

$$F_{damper} = cV_m \tag{17}$$

Equation 17: Force due to an Applied Damper

In equation 17, the damping coefficient, c, is varied through this simulation to understand the effects the damping has on the simple kinematics, system energetics, applied force, and actuation velocity. The range was determined from nearly zero damping to a damping effect that caused drastic decreases in the output muscle force. The mass of the leg was held at 10mg for this simulation in its entirety. It should be noted that for the duration of this simulation and subsequent simulations, the muscle velocity associated to the damping force was derived from the following equation:

$$V_m = \dot{\theta} l_{in} \sin(\theta) \tag{18}$$

Equation 18: Horizontal Muscle Velocity during Actuation of Leg Kick

The muscle is defined as such because of two reasons: 1) the importance of the muscle's velocity depends on the change in angular velocity of the rotating leg components and 2) the position of the resolved applied force during the kick. Without the consideration of these two components the muscle velocity would not be properly defined for the resulting data and the cases that build on top of this case's simulation. However, this is changed in Case 4.

4.5: Case 4: Spring – Damper Muscle Force with Consideration of Gravity

Previous simulation iterations did not explore the effects of gravity on the theoretical kick of a locust leg. In this case, the mass of the leg is an evenly distributed along the lower leg. The center of mass, denoted by $m_{body}g$, is located $\frac{lout}{2}$ away from the pivot joint of the rotating leg geometry, as seen in figure 25. In order to take the summation of the torques in this simulation, the leg weight is resolved to use the contributions of the force acting perpendicularly to the leg geometry. The consideration of the torque within the governing equation for this simulation is as follows:

$$I\ddot{\theta} = \left(F_{applied}\sin(\theta)\, l_{in}\right) + \left(\frac{l_{out}}{2} m_{body} g cos(\theta)\right) \quad (19)$$

Equation 19: Governing Equation of Spring-Damper Muscle Force with Gravitational Effects (Case 4)

, where the force applied is still related to the spring and damper acting in parallel as the muscle force.

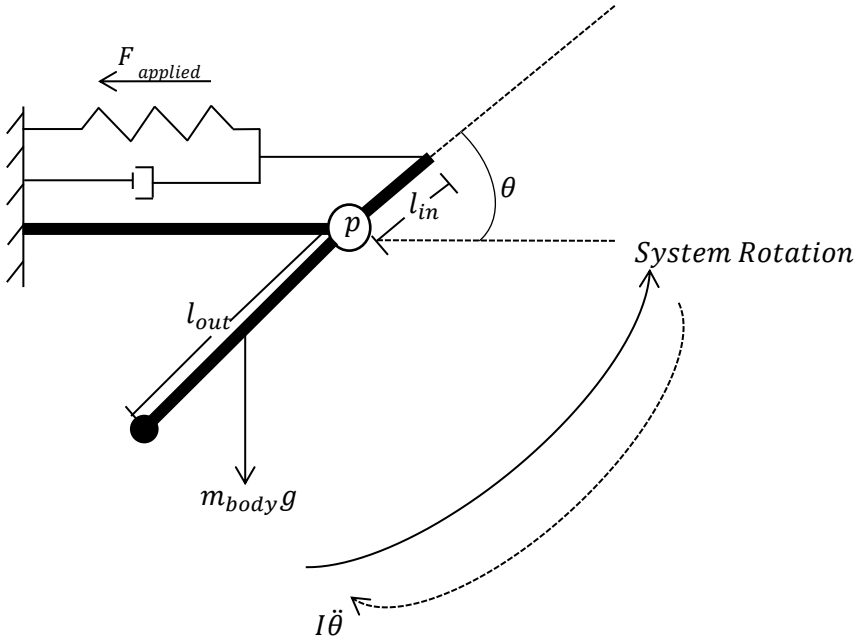

Figure 25: Case 4 problem schematic with an applied force composed of a spring and damper in parallel similarly to Case 3, but with proper leg mass contributions. The mass of the lower leg is evenly distributed along the lower leg length, l_{out}, but then resolved for a single applied force at a distance of $\frac{l_{out}}{2}$ from the knee joint.

With the proper loading of the lower leg mass, this simulation represents the first case that is somewhat comparable and representative to an actual MSK system. This simulation case allows for the characterization of the system under force based loading. In this case, the leg mass was assumed to be the weight load applied to the system. Each load was run for damping coefficients of 0, 0.0001, 0.001, 0.01, 0.1, 0.5 kg/s.

The drawback with this simulation is the lack of consideration for the reaction force associated with a jump. All simulations up to this point have disregarded an actual jump, and aimed to characterize a leg kick. This is taken into consideration during Case 5, which adds a ground reaction force acting on the base of the lower leg.

4.6: Case 5: Spring – Damper Muscle Force with Consideration of Gravity and Reaction Forces

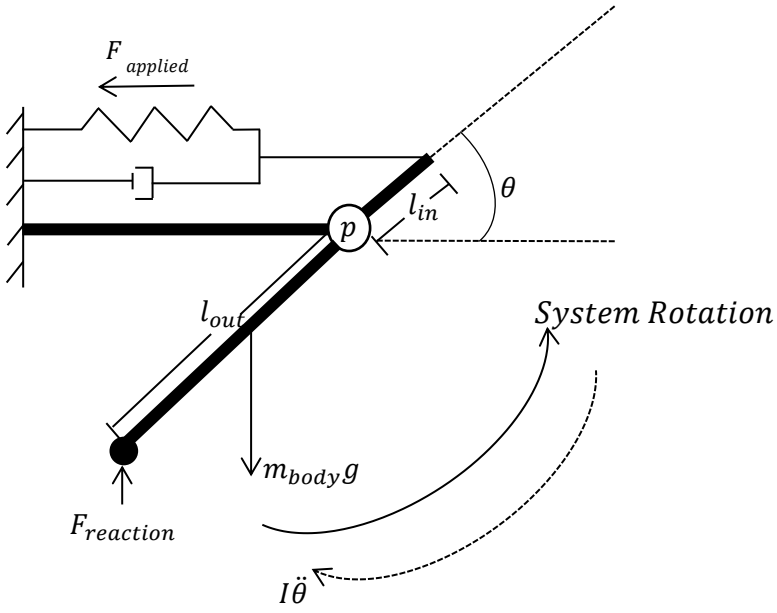

Figure 26: Model schematic of Case 5 which follows the proper weight loading as proposed previously in Case 4, but add the ground reaction force acting on the leg. This is denoted by $F_{reaction}$ that acts at the base of the lower leg, and assumes the leg does not slip from the ground and friction does not play a factor.

As previously suggested in Section 4.5, all previous models and simulations of the locust leg neglected the effects of ground reaction forces. Without this consideration previous models represent a leg kick, not a leg jump. This simulation looks to resolve all the forces acting on the leg, with the addition of a ground reaction force, to represent a leg jump. In this case, the governing equation is defined as such:

$$I\ddot{\theta} = \left(F_{applied}\sin(\theta)\, l_{in}\right) + \left(\frac{l_{out}}{2} mgcos(\theta)\right) - \left(l_{out} F_{reaction}\cos(\theta)\right) \quad (20)$$

Equation 20: Governing Equation of Spring-Damper Muscle Force with Gravity and Ground Reaction Forces (Case 5)

, where the ground reaction force needed to be resolved into the y-component, as previously accomplished for the weight force applied in Case 4. If the steps to resolve the forces in the

appropriate direction are not taken, then issues will arise during the summation of torques process to get the appropriate governing equations 19 and 20.

Furthermore, the ground reaction force was assumed to be 10 times the weight ($m_{body}g$) of the leg for the nominal case. This assumption stems from the weight of the entire locust being some constant multiple of the leg mass. Further, acceleration was considered to be used to determine the ground reaction force, but, due to the solution method, it was much easier to get proper data using the mass of the leg multiplied by the gravitational acceleration. Furthermore, this assumption makes sense due to the acceleration output of the rotating leg from the simulation being related to the leg rotation not gravitational affects.

During the simulation two other ground reaction forces were examined: 50 times the leg weight and 100 times the leg weight. The effects of an organism's weight during a jump wanted to be determined, in order to understand how the force-velocity curve would be changed. The damping coefficient was held at 0.5 kg/s as this applied a great enough resistive force for the addition of the reaction force to the modeled governing equation 20.

4.7: Case 6: Spring – Damper Muscle Force with Consideration of Gravity and Drag Forces

The last simulation utilizes the model derived in Case 4, but adds a drag force, F_{drag}, to study the effects that varying viscosities have on the simulation model. As the model has been previously used and assumed to be two-dimensional, there was no need to define the shape or dimensions of the lower leg. However, it is now necessary to designate the shape to solve for the drag force applied. Further, for better understanding on the effects that viscous forces have on the actuator and solution method, the model will be compared to a fin of a fish.

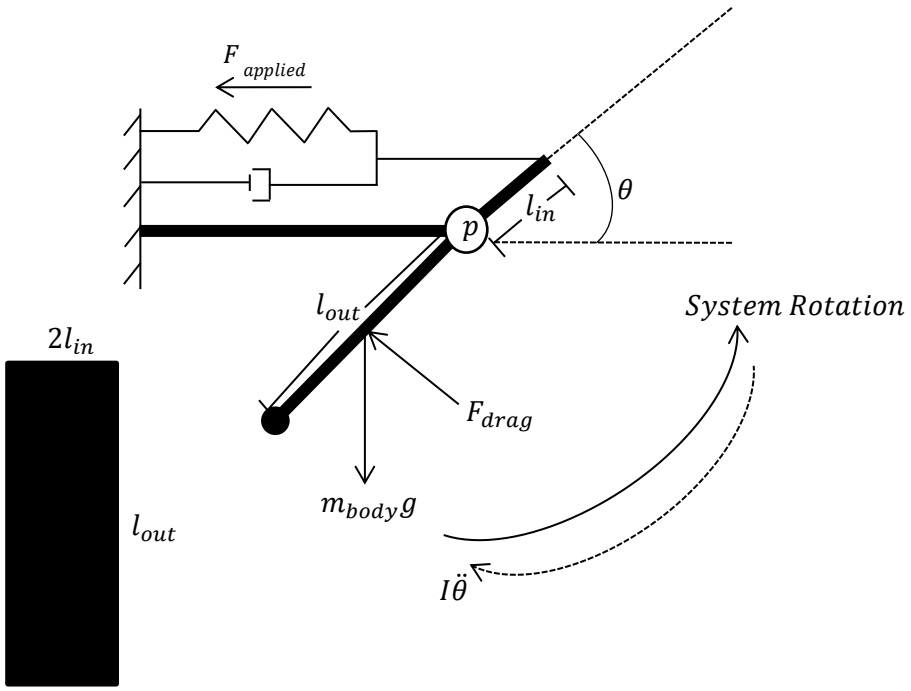

Figure 27: Case 6 model schematic with applied drag force and weight acting at $\frac{l_{out}}{2}$ of the fin. The drag force, F_{drag}, acts normal to the fin surface, that has dimensions of $2l_{in}$ by l_{out}., while the gravitational force still needs to be resolved for the y-component prior to summing all torques about the pivot point.

From understanding basic principles of fluid mechanics, the drag force, F_{drag}, acts perpendicularly to the surface area regardless of position/orientation of the area. Moreover, the drag forces acts uniformly across the entire surface, but for this case, the drag force is resolved to act in the center of the fin geometry, denoted by the all black piece in figure 27. This leaves the summation of torques to be fairly easy to get equation 21.

$$I\ddot{\theta} = \left(F_{applied}\sin(\theta)\, l_{in}\right) - \left(-\frac{l_{out}}{2}\left(mgcos(\theta) + F_{drag}\right)\right) \tag{21}$$

Equation 21: Governing Equation of Spring-Damper Muscle Force with Gravity and Drag Forces (Case 6)

Due to the actuator not changes from previous cases, $F_{applied}$ is still defined by the addition of the spring and damper force. The only addition for this case is the drag force, defined by equation 22 below.

$$F_{drag} = \frac{1}{2} C_d \rho {V_{l_{out}}}^2 A_f \tag{22}$$

Equation 22: Drag Force

For this equation, C_d is the coefficient of drag that was determined through commonly used shapes [42]. A flat, rectangular plate was assumed to be representative of the fin for this case and has a coefficient of drag of 1.28. The density was determined from varying percent glycerine solutions at 20°C, roughly room temperature [43]. These densities and associated percent glycerine solutions can be found in table 3. The velocity, $V_{l_{out}}$, is the velocity of the fin as it moves through the varying glycerine solutions. Lastly, the frontal area, A_f, is obtained from the area of the theoretical fin, depicted in figure 27, as $2l_{in}l_{out}$.

Density of Glycerine-Water Solutions		
Glycerin	**Density at 20°C**	**Density at 20°C**
%	*(g/mL)*	*(kg/m³)*
0	0.99823	998.23
25	1.0598	1059.8
50	1.1263	1126.3
75	1.19485	1194.85
100	1.26108	1261.08

Table 3: Percent Glycerine Solution and Associated Density at 20°C [43]

Similarly to Case 5, the damping coefficient was held at 0.5 kg/s to understand the effects of viscous drag on the model rather than the effects of damping in addition to the viscous drag on the rotating geometry. Further, only 10mg and 80mg leg masses were observed for this simulation. It was assumed that the variance would be greater observed between the 10mg and 80mg cases, rather than completing the simulations with more varying loads between the minimum and maximum leg weight.

Chapter 5: Experimental Set-up

Experimentation involved the use of a McKibben air muscle test fixture and LabView interface created by Phatak to identify the force-velocity relation under varying air pressures [44]. Overall, the test fixture remained the same for components used to measure absolute pressure changes and contractile distance, data processing from the LabView program, and hardware. Slight changes, however, were made to create a better comparison to the theoretical models and simulations presented in Chapter 4. The main change was the addition of two dampers in parallel with the McKibben air muscle. This causes the experimental test fixture to not only be synonymous to the simulated 'muscle', but comparable to Hill-type muscles shown in figure 23. The use of two dampers further allows for better control of contraction and expansion of the McKibben air muscle. As the solenoid valve is opened or closed, the test fixture 'muscle' is limited to two-degrees of freedom: the z-axis and rotation about the z-axis. The axes can be seen in figure 17. It should be noted that for the inertial and viscous loading conditions an additional test fixture was employed that enabled linear movement along the y-axis and rotation about the x-axis.

For all loading conditions tested, the following were held constant:

Testing Conditions	
Gauge Pressure	40 psi
Contractions per Weight/Case Trial	3 contractions
Flow Rate	¼ turn from fully closed

Table 4: Test Conditions for Force, Inertial, and Viscous Experimental Tests

Set-up for the experimental testing started by turning on the air supply and checking the pressure gauge of the air compressor to ensure it is set to 40 psi. To guarantee the flow valve is placed at the proper opening value, it is first placed in a fully closed position. From here the valve is opened a ¼ turn. The system is run for 5 minutes prior to testing the system, so it has reached a steady state. During this time, the power supply is turned on to 12V, the excitation voltage for the linear potentiometer, and the LabView program is launched. Once set-up is complete, the resting length and diameter are measured using calipers between specified points on the McKibben air muscle. This is done prior to each test, and start-up of the test fixture.

Depending on the testing case, the appropriate damping and weight is applied to the appropriate test fixture modification. An initial contraction is held after the addition of weight. A contractile length and contractile diameter are measured with calipers, and recorded in the appropriate post-processing Excel sheet, along with the testing conditions and any other data pertinent to the test.

In general, each scenario used the same post-processing data method. An Excel spreadsheet collected all data related to time, absolute pressure, and linear potentiometer voltage readings. The linear potentiometer voltage was then changed into a displacement length using the relationship that 1 volt is equivalent to 0 inches, while 10 volts is related to 1 inch. The length was then converted from English units to metric for the contractile velocity to be determined. The contractile velocity was obtained by dividing the change in linear potentiometer length by the change in time. However, due to the actuation of the muscle, the velocities associated with the contraction are negative, while those associated with expansion are positive. In order to obtain the contractile velocity as positive, the determined velocity was multiplied by -1. The data associated to time and contractile velocity were then read into MATLAB using the code found in Appendix H. This code plots the contractile velocity versus time, but due to the noise associated with the data a moving average filter was applied to obtain a smoother curve from the data. The maximums were taken from the filtered data to be the maximum contractile velocity for the load scenario and applied loading trial. Force velocity curves for each loading case were then acquired.

5.1: Force Loading Modifications

Force loading used the addition of a basket for the weights to be placed on. This allowed for direct loading onto the ‘muscle’. Masses of 500g were added one by one onto the basket to allow force loading of masses 500g to 4000g to be observed. Placement of the weight basket can be observed in figure 28.

Three contractions were taken for each weight trial and damping force applied. For this experimental case, two damping scenarios were observed. Adjustment for increased or decreased damping is applied through the knobs at the top of both dampers acquired from Airpot (Model: 2KS325A2.0TX). For minimal damping a single turn from the no-damping condition was applied, while for maximum damping, four turns from the no-damping applied condition

were applied. A total of three experimental tests were completed for both the minimal and maximum damping cases for all weights.

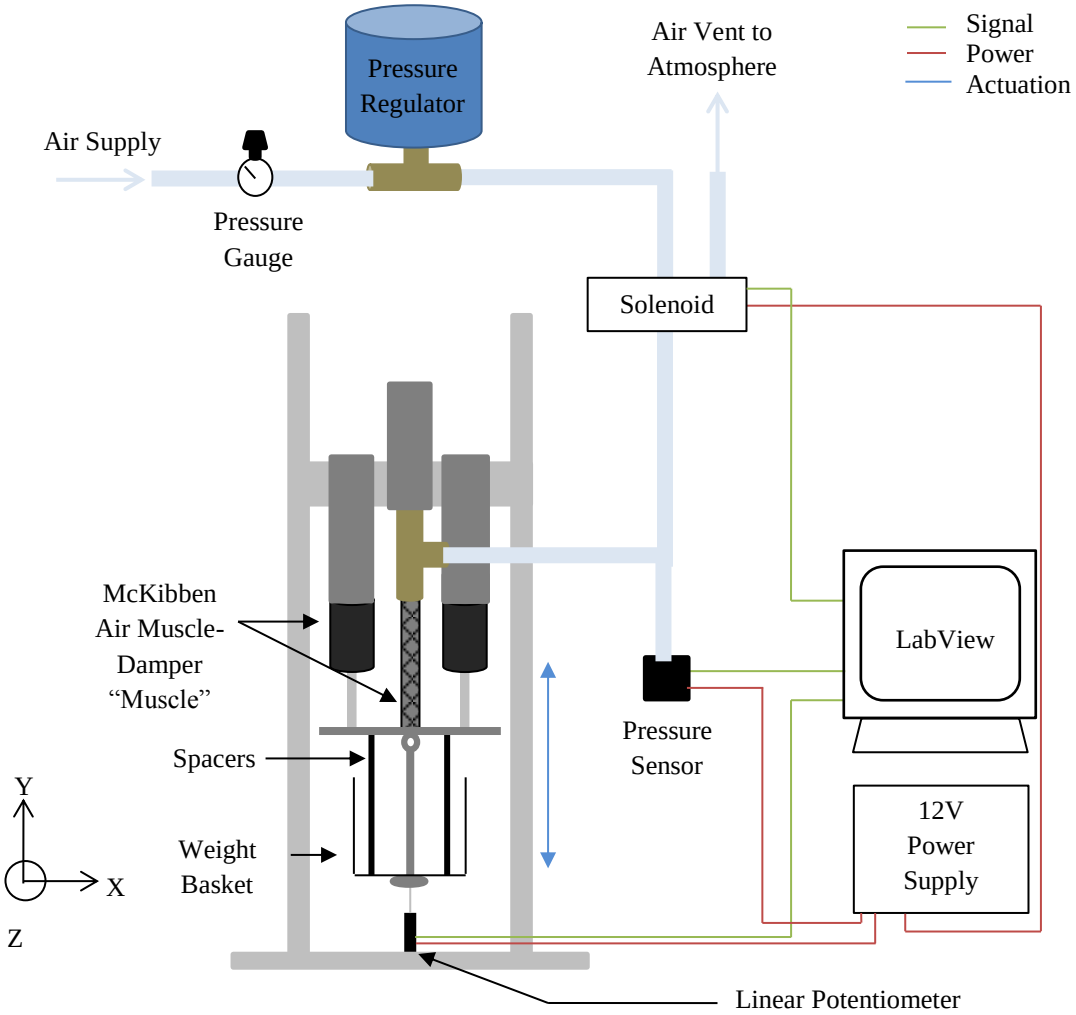

Figure 28: Schematic of force loading experimental test fixture with modification of dampers in parallel with the pneumatic air muscle and the addition of the weight basket. Actuation of the muscle occurs only about the Z-axis, shown previously in figure 17. After the completion of each trial, per weight, data was exported from the LabView code into a data drop excel file, and then copied into the appropriate data processing spreadsheet.

5.2: Inertial Loading Modifications

The inertial loading experiment aimed to determine the effects of indirect loading on the 'muscle' performance. In doing so the same test fixture, shown in figure 28, was used for this case. However, the addition of an inertial loading test bed was accomplished. This test bed utilized linear bearings and rails for the weight to be applied, while being attached to the muscle

by the use of heavy-duty rope. As previously suggested at the beginning of Chapter 5, the addition of this test bed allows for movement in the Y-axis, due to the placement of the inertial test bed to the overall test fixture, in figure 30. A diagram of the inertial test bed is shown below in figure 29.

c

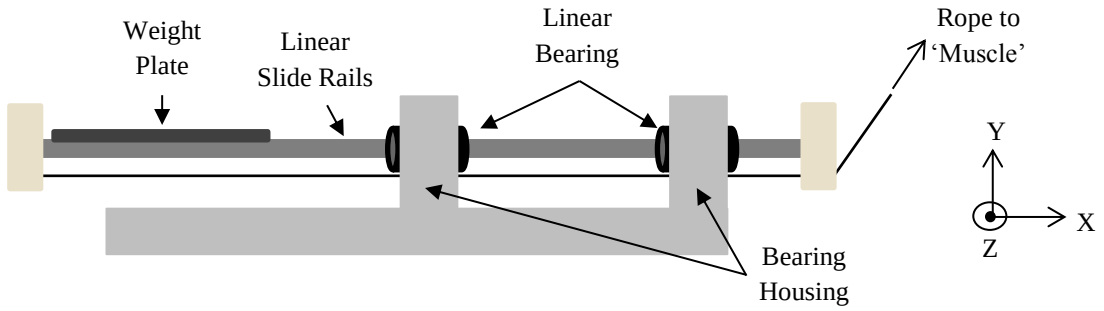

Figure 29: Inertial test bed fixture that allows for linear motion along the Y-axis through the use of linear slides and linear bearings. A weight plate was attached directly to the linear slide rails to enable the indirect force loading. Not shown in the picture above are the pulleys within the bearing houses. The pulleys allow for placement of the rope, and ensure that the rope moves without resistance to the contractile force from the 'muscle'.

Similarly to the force loading case, weights ranging from 500g to 4000g were applied to the test fixture, and data was processed using methods suggested at the beginning of Chapter 5.

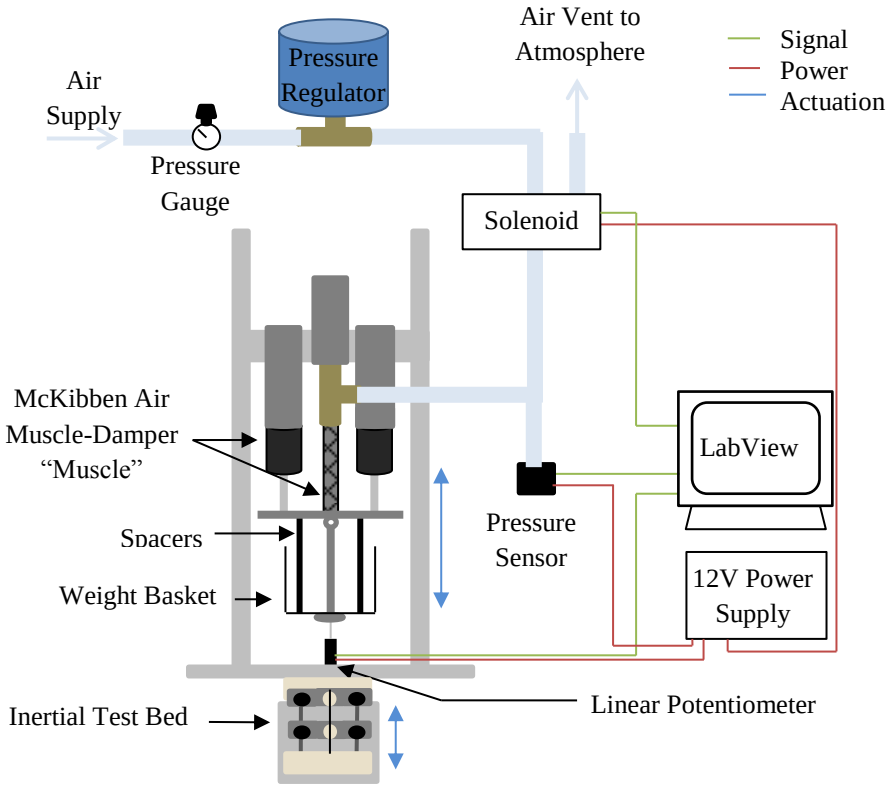

Figure 30: Integration of inertial test bed with overall test fixture that allows two degrees of freedom at the 'muscle', but linear motion of the inertial test bed along the Y-axis. Weighs varying from 500g to 4000g were placed on the test bed's linear rails.

5.3: Viscous Loading Modifications

Previously, weight was added to the test fixtures of figure 28 and 30. For the viscous loading experimental case, weights were not added to the test fixture. Instead, the actuation of the muscle under viscous loading was observed through the addition of a paddle to the inertial test bed. The inertial test bed was machined to allow a 3/8 inch linear rod to be fitted through the base structure. The paddle was created to be 6inches by 6inches in frontal surface area from 3d printed ABS. The paddle is able to slide onto the 3/8 inch linear rod with the addition of a pulley for rope placement. This allowed the paddle to rotate about the X-axis by the attachment of the heavy-duty rope to the base of the paddle and the base of the experimental 'muscle', shown in figure 31.

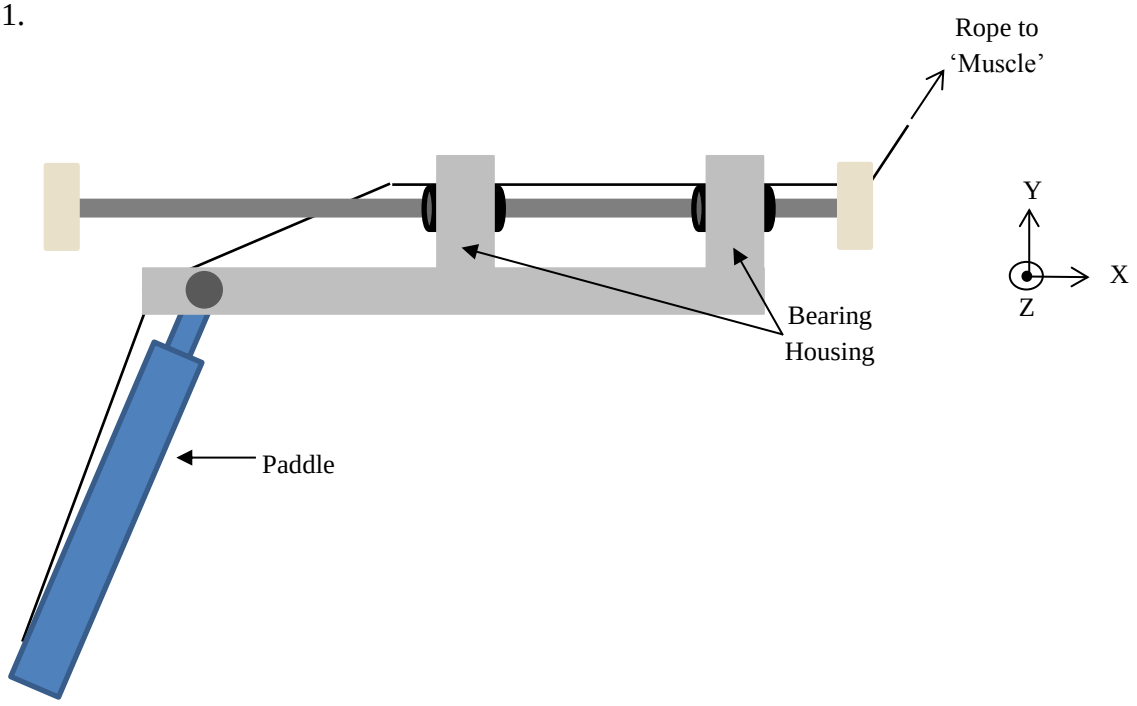

Figure 31: Modifications associated with the inertial test bed include the 3/8 inch through hole for a linear shaft, pulley, and paddle attachment. The paddle rotates about the X-axis, and allows for two degrees of freedom for the entire test fixture to actuate. The paddle was tested under air and water viscous cases. Water, at room temperature, was placed in a bucket for the paddle to actuate in. The rope utilized the pulleys along the bearing houses to decrease the resistance to contractile actuation.

The paddle was observed under water and air actuation, both assumed to be 20°C. This allowed for proper calculation of the drag forces acting on the paddle through the use of equation 22.

Chapter 6: Results and Comparisons

Results per each theoretical simulation and experimental case are presented within this section. Comparisons are made on the effects of varying actuator types and external forces, while presenting validation data to support both the work presented throughout this thesis.

6.1: Case 1: Constant Applied Force

As discussed in Section 4.1, an applied force, resembling a spring force, was used for the first simulation. However, this force was held constant throughout the entirety of the simulation, as represented by figure 32. The purpose of this case was to understand how the simulation acts under varying loads and mechanical advantages as a baseline for the subsequent theoretical cases. Further, this force did not change with the variance of leg masses, 10mg, 20mg, 40mg, 60mg, and 80mg, and nominal in-lever, l_{in}, length.

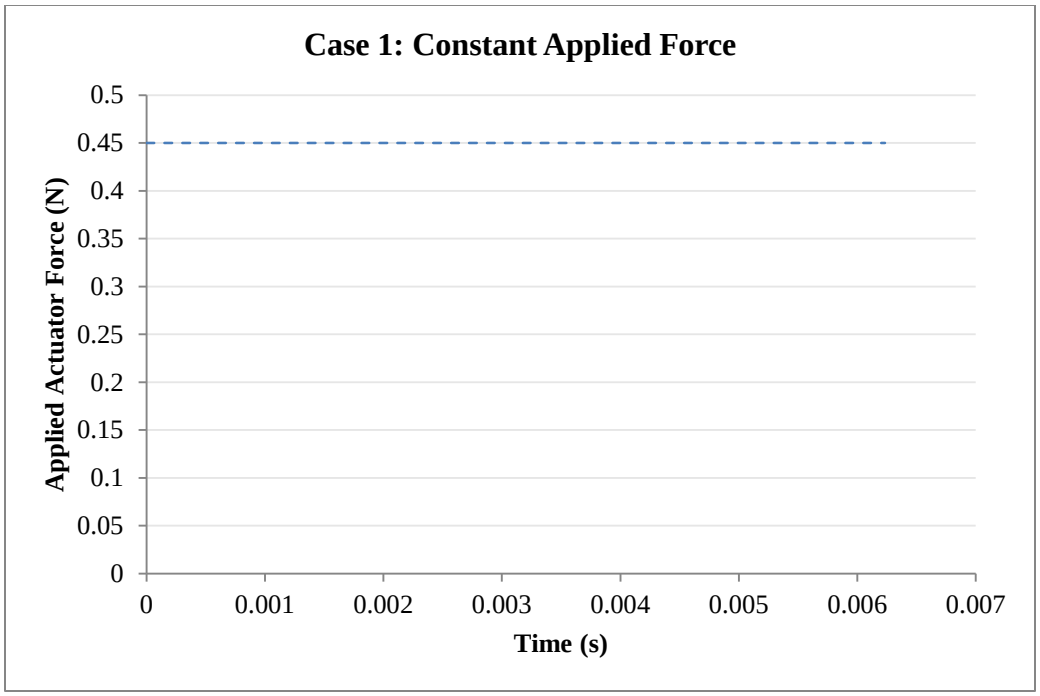

Figure 32: Applied actuator force during the entirety of a leg kick, under constant force application. The force was calculated using equation 11, which is synonymous to a spring force. However, the force was calculated using a constant, L. This value was held at the maximum possible stretch value, $1.5e^{-3}$m, because this is equivalent to the maximum possible force output of the system.

However, the simulation did show changes along the angular displacement attributed to each leg mass applied in figure 33. This is to be expected because the leg mass is assessed within the simulation through the moment of inertia about the lower leg, a distance of l_{out} from the pivot point. With an increase in the leg mass, there is ultimately an increase in the moment of inertia and, subsequently, a decrease in the angular displacement of the system at a given time.

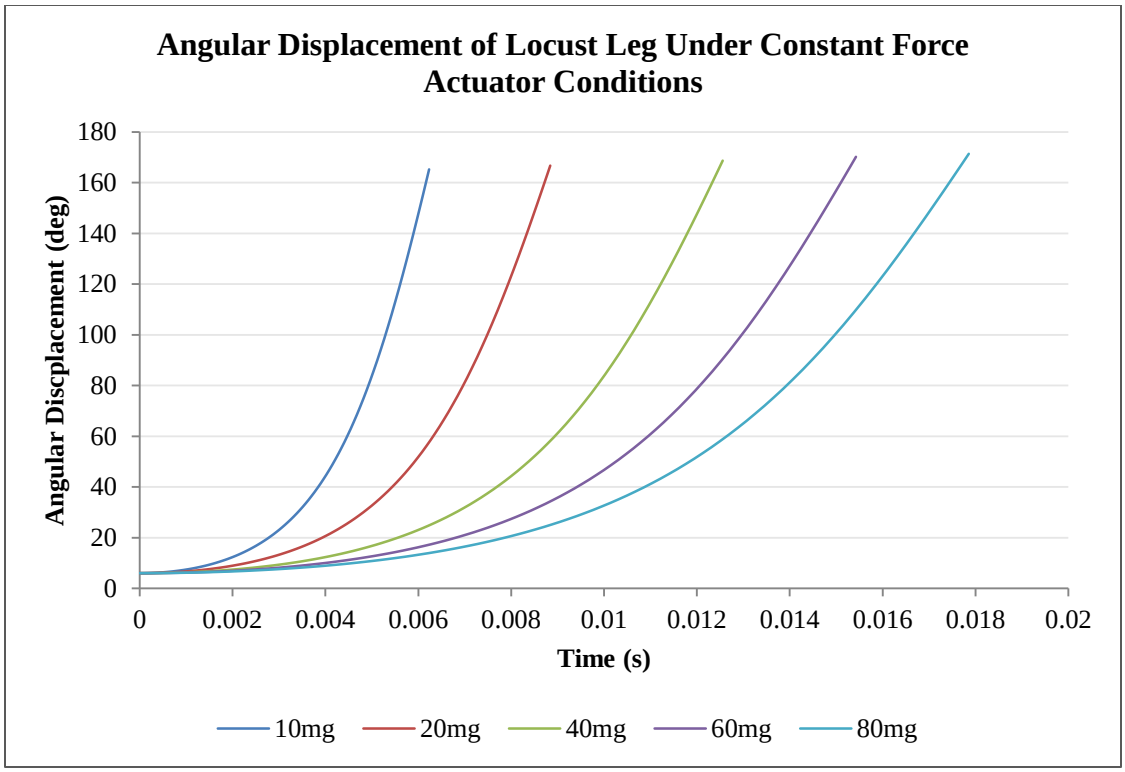

Figure 33: Variation in the angular displacement of the locust leg kick with a constant, controllable applied force. In this case, the maximum possible angular displacement increases slightly from 165.2201° with a 10mg load to 171.3678° with a 80mg load. Further, the time to get to this maximum angular displacement slowly increases over the increase in applied load. This is to be expected as the load slows down the speed of the translational velocity of the lower leg geometry. It should be noted for this graphical interpretation and comparison, the in-lever length, l_{in}, remained at the nominal length of $7.6e^{-4}$m.

Increases in the simulation time, as the load increases, occurs due to the change in translational velocity of the lower leg, more specifically the linear velocity in the y-direction. This can be depicted by figure 34, where the translational velocity of the lower leg, is compared not only to nominal in-lever length, but percent changes of -75%, -50%, 50%, 75%, and 100%. For loads of 10mg and 80mg, increases of 200% and 300% in-lever length were further assessed. The purpose of changing the in-lever length was to assess the changes in mechanical advantage, previously defined by equation 2. It is observed that the translational velocity increases relative to the mechanical advantage, in addition to the already apparent differences in maximum translational velocity for a given applied lower leg mass.

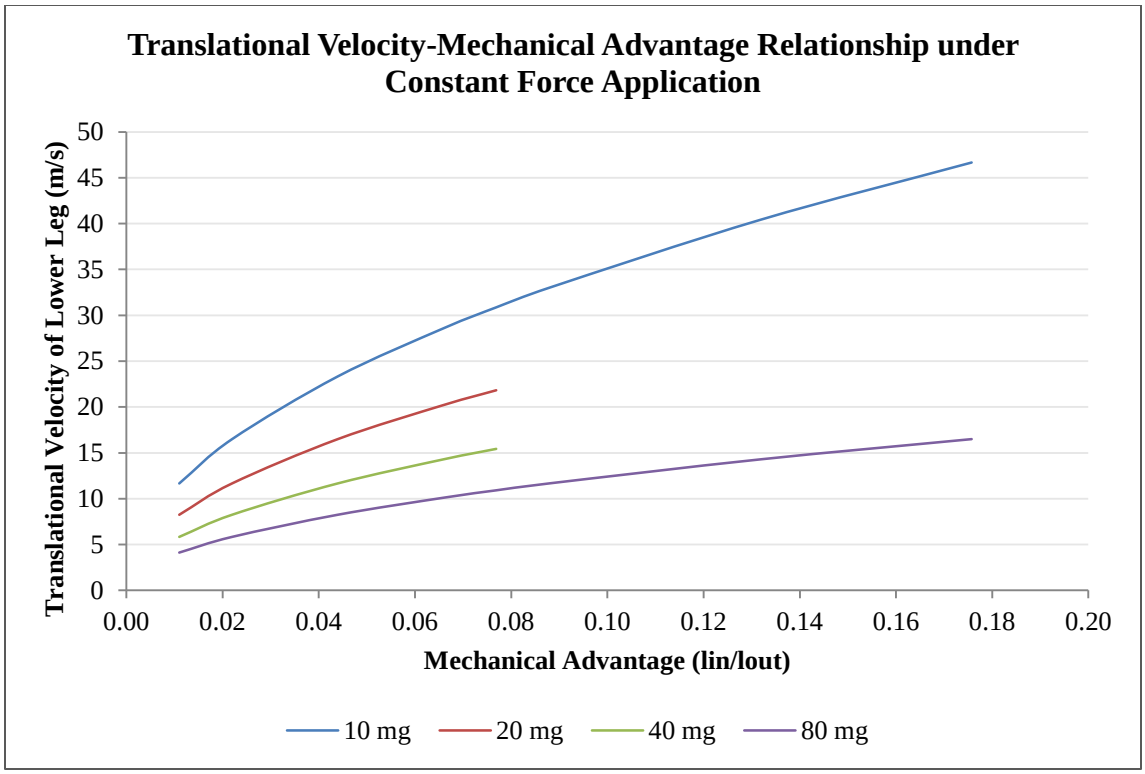

Figure 33: Relationship between translational velocity changes of the lower leg and mechanical advantage increases and decreases. It is observed that not only is there apparent increases between the loads applied under the nominal case, but increases due to the increase in mechanical advantage. Leg masses of 10mg and 80mg have longer resulting graphs due to the calculation of 200% and 300% increases of in-lever length.

Lastly, the rate of change in angular momentum about the pivot point, p, was observed in relation to the mechanical advantage. This value is the torque of the system as it rotates about the knee joint in the locust leg. It can be defined by the following:

$$RoCAM = I\alpha \tag{23}$$

Equation 23: Rate of Change of Angular Momentum about Pivot Point, p

It has been previously suggested by other researchers, that due to the inability to hold the muscle velocity of a system constant, the torque produced by the rotation of the system will remain constant with increases in mechanical advantage. This simulation disproves this theory through the use of figure 34. With an increase in mechanical advantage the torque of the system increases linearly for all loads. This is to be expected based on the very definition of $RoCAM$ given by equation 23. The moment of inertia is based on the variance in the load, while the

angular acceleration is subsequently solved from the changes in load applied through this inertia. Thus, is understandable that the two will increase linearly as they do in figure 34.

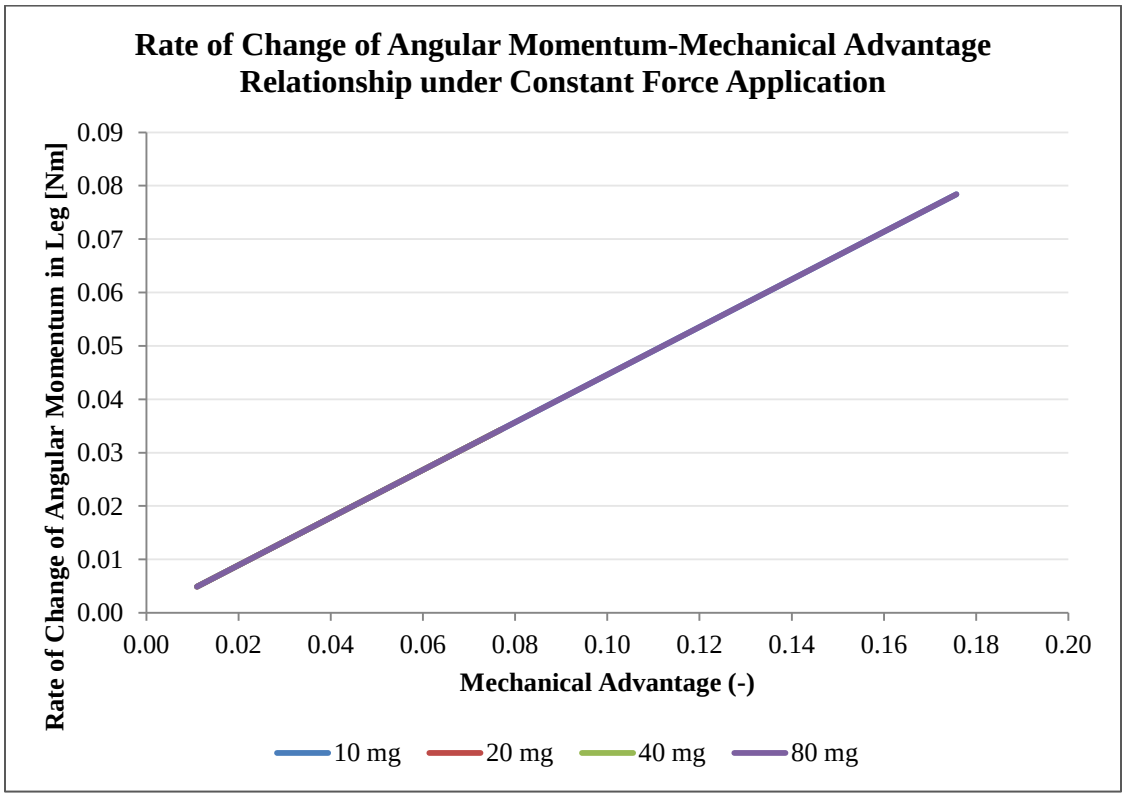

Figure 34: Depiction of linear relationship between rate of change of angular momentum, better known as the leg kick's torque, and mechanical advantage. It is shown that regardless of the mass, the rate of change of angular momentum is the same for all leg masses. This can be justified through the understanding of equation 23. Even though the loads vary, the moment of inertia and angular acceleration can be comparable between each of the loads by a constant multiplier. For this system the rate of change of angular momentum cannot be changed unless a different muscle is used for each of the loads.

6.2: Case 2a and 2b: Spring Muscle Force in terms of l_{in} and θ

Case 2a and 2b were the first cases that employed the use of a spring within the simulated locust leg kick. The difference between the two stemmed from the definition of the springs stretch as it related to time, L. Case 2a related L to the length of the upper leg, l_{in}, while Case 2b corrected for the errors in defining L through the upper leg length by associating it only with θ, the leg's instantaneous position. The errors suggested with Case 2a are related to the direct relation created between the translational velocity and mechanical advantage when defining L

with respect to l_{in}. However, mechanical advantage should not be directly related to the change in velocity. In turn, it should still be related but in a less direct manner. Using θ to correct for this in the applied force equation 15, enables the force, velocity, and mechanical advantage to present proper data seen in Case 1. This effect and comparison between Cases 2a and 2b can be seen below in figure 35.

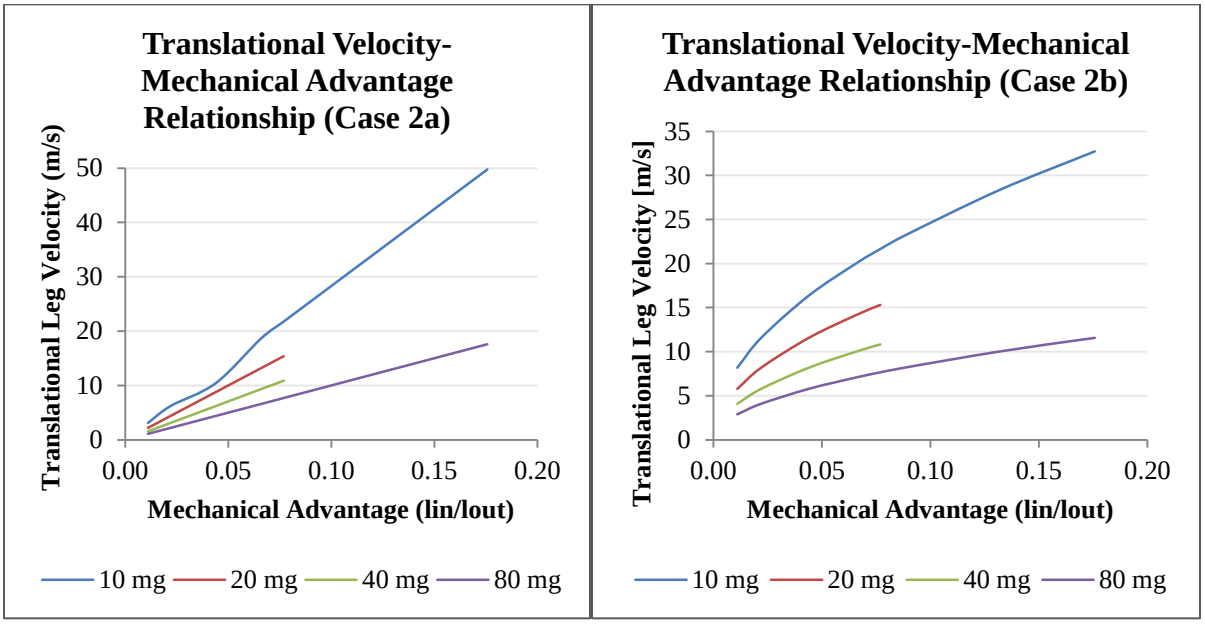

Figure 35: Result comparison of the translational velocity-mechanical advantage relationship between Case 2a and 2b. As it is observed, using l_{in} to define the spring's change in length over the kick, causes a linear relationship between the translational velocity and mechanical advantage. However, with the change in spring's length being defined by θ, allows for the two variables to not be directly related. Further, the results from Case 2b resemble those derived from Case 1 in figure 33.

Further on top of there being a difference between the translational velocities, there were differences between the comparison results of the rate of change of angular momentum and mechanical advantage. Similarly to the translational velocity-mechanical advantage relationship from Case 2a, errors were observed in the relationship between rate of change of angular momentum and mechanical advantage. However, this was corrected for again by redefining equation 13 with the use of θ in equation 15. The results between the cases can be observed below in figure 36. Further, it should be noted the discrepancies in values of translational velocity and rate of change of angular momentum between the Cases 2a and 2b with Case 1.

This is due to the change in actuator. The first case only dealt with an actuator that did not 'die out' over the course of the kick. In this case, the force applied by the actuator decreases overtime until there is no force left to cause further rotation of the leg geometry. This allows for decreases to be seen in the translational velocities observed and the rate of change of angular momentum observed within Cases 2a and 2b.

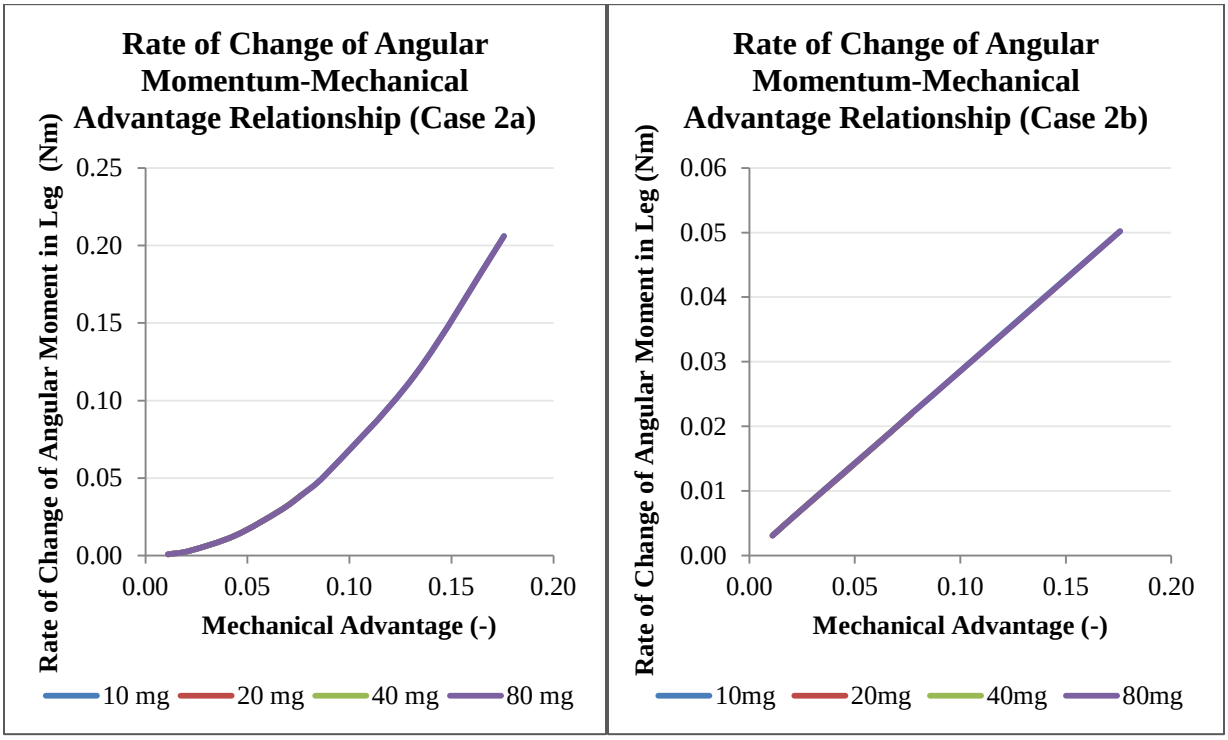

Figure 36: Comparison between the rate of change of angular momentum-mechanical advantage relationship between Case 2a and 2b. Once again, due to the use of l_{in} in defining the spring's instantaneous stretch throughout the locust leg kick, it is apparent the effects are related to mechanical advantage changes, defined by equation 2. The use of θ in defining the spring's instantaneous stretch, by equation 15, eliminates this direct correlation to obtain the proper data observed in figure 34. Further, the differences between the values of the rate of change of angular momentum are attributed to the change in actuator used between Case 1 and Cases 2a and 2b.

6.3: Case 3: Spring – Damper Muscle Force

After the completion of properly defining the spring by the change in angular position during a kick, the application of an ideal damper in parallel with a spring was observed. For this case, the main variation was related to the damping coefficient and the effect that increasing or

decreasing the damping coefficient has on the model. In this case, a mass of 10mg was used throughout to understand the effects on the spring-damper 'muscle'.

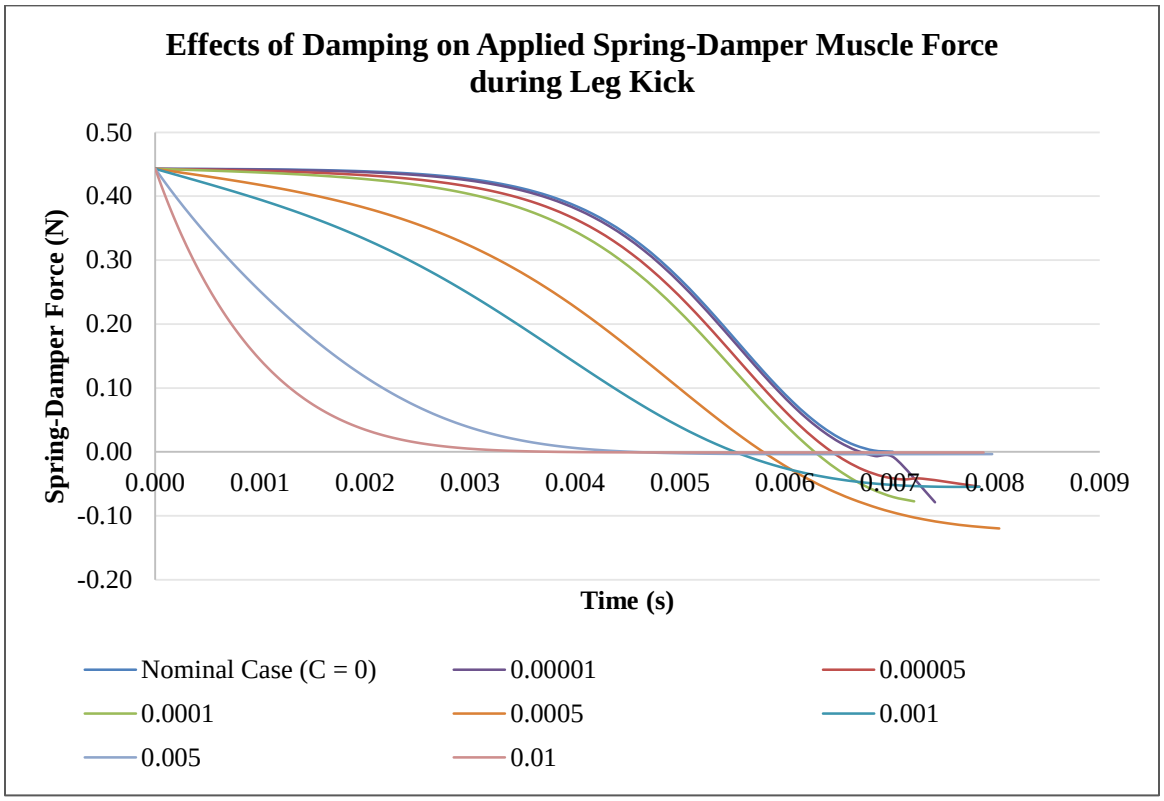

Figure 37: Effects of the damping coefficient on the spring-damper muscle show that very little change occurs with a damping coefficient of 0.0001, 0.00005, and 0.0001 kg/s. However, once 0.0005 is applied to the system, the simulation outputs data that proves the damping coefficient effects the muscle force overtime greatly. Further, damping coefficients of 0.005 and 0.01 kg/s dramatically affect the muscle actuation force, and cause the force to go to zero almost immediately.

As seen in figure 37, the effects of the damper greatly affect the muscle output force. In this case, damping coefficients of 0.01 and 0.005 kg/s drastically decrease the output force. On the other hand, damping coefficients of 0.00001, 0.00005, and 0.001 kg/s hardly affect the overall force output of the theoretical muscle. These effects lead to the investigation into the translational leg velocity and muscle velocity affects. It was hypothesized from the effects of damping that the translational velocity would decrease the maximum possible rotational velocity output, subsequently the translational velocity of the leg during a kick. Further, due to the addition of the damper, the time for the actuation to complete will increase. These hypotheses

were confirmed through figure 38, a comparison between the muscle velocities over time due to changes in damping coefficients.

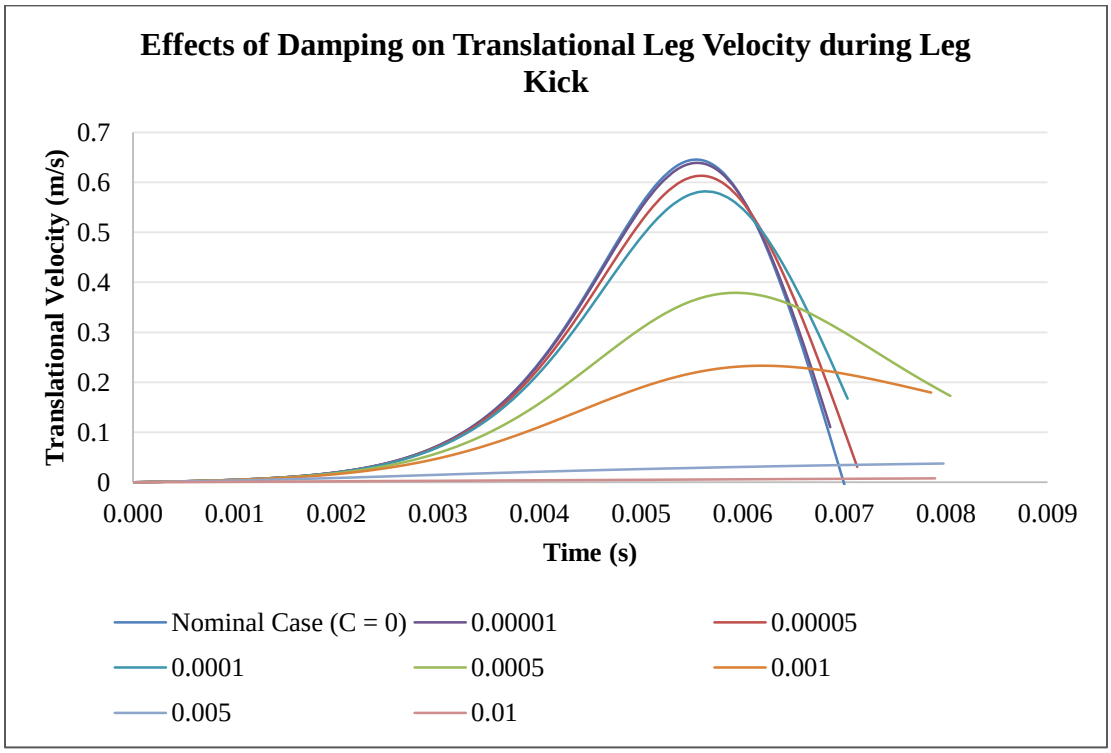

Figure 38: It can be observed that the previously stated hypothesis holds true. The increasing the damping coefficient causes increases in actuation time of the leg rotation during a locust leg kick. Further, the translational leg velocity observed decreases with the increase of damping coefficient. This is understandable because as the damper is resisting the contraction of the spring during a kick, the maximum achievable velocity of the leg during rotation will decrease from this resistance.

In addition to the effects of translational velocity due to damping, it is very clear that there are effects on the muscle velocity itself. As previously defined by equation 18, muscle velocity is related to angular velocity, and change in position of the upper leg. Further from equation 17, the velocity of the muscle is directly proportional to the damping force. In this case, due to this direct relationship from equation 17, the graphical representation of these two should be linear. This linear relation can be seen in figure 39 below. Not only from equation 17, but figure 39, it is apparent that the slope of the linear line between the two is equivalent to one divided by the damping coefficient. More so, this relationship shows that the damper acts as an ideal damper within these simulations and the muscle force can be interpreted as an ideal muscle for the remaining simulations.

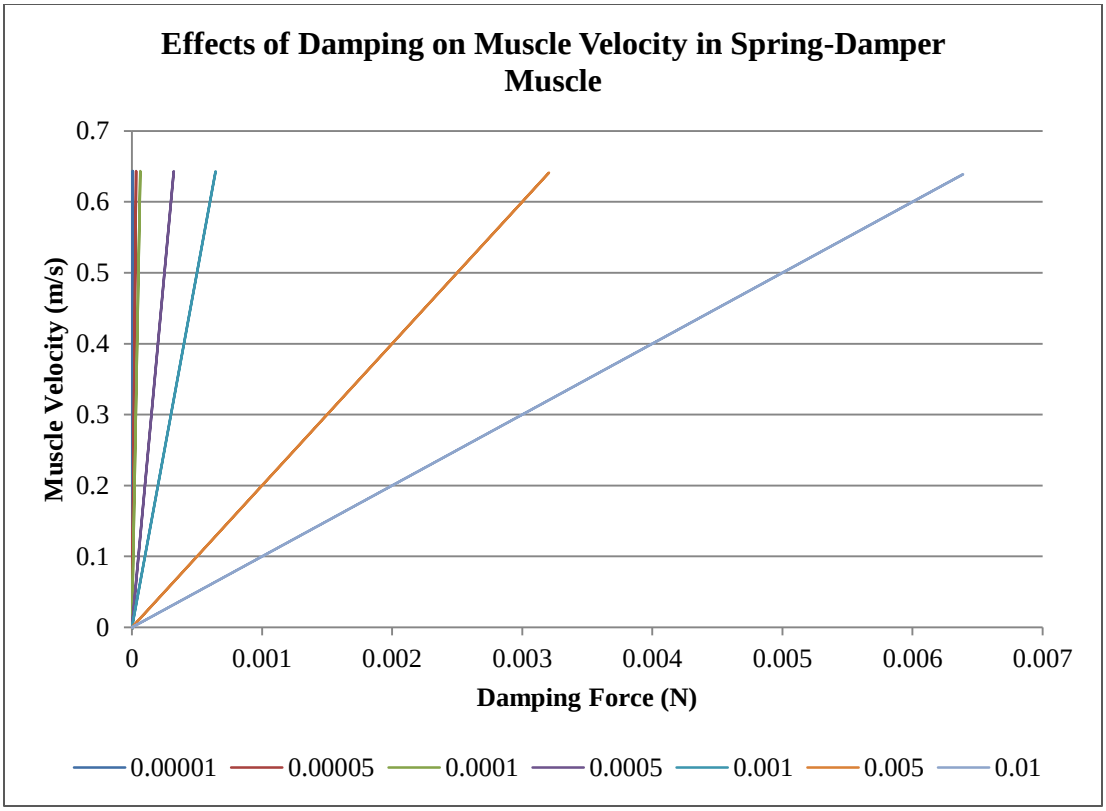

Figure 39: Relationship between muscle velocity and damping force within the spring-damper muscle system. The linearity between the two variables represents the relationship defined by the damping force in equation 17, where the damping force is equivalent to the muscle velocity times the damping coefficient. The slope of each of these lines to be one divided by the damping coefficient used.

It should be noted from figure 39 that the smallest damping coefficients produce extremely steep lines that look as if they would be undefined. However, this is more so due to the values being so much smaller in a case where the damping force is negligible to those that affect the muscle performance, like damping coefficients of 0.005 and 0.01 kg/s.

6.4: Case 4: Spring – Damper Muscle Force with Consideration of Gravity

Cases 1 through 3 employed the use of a point mass held at a distance of l_{out} from the pivot joint of the leg geometry. This case begins to use a resolved force at $\frac{l_{out}}{2}$ of the lower leg. With this, a true force-velocity curve could be determined to visualize the effects of changing spring stiffness and damping on the muscle. First the effects of spring stiffness were observed with k equal to 200, 300, and 400 kg/s², while damping was zero.

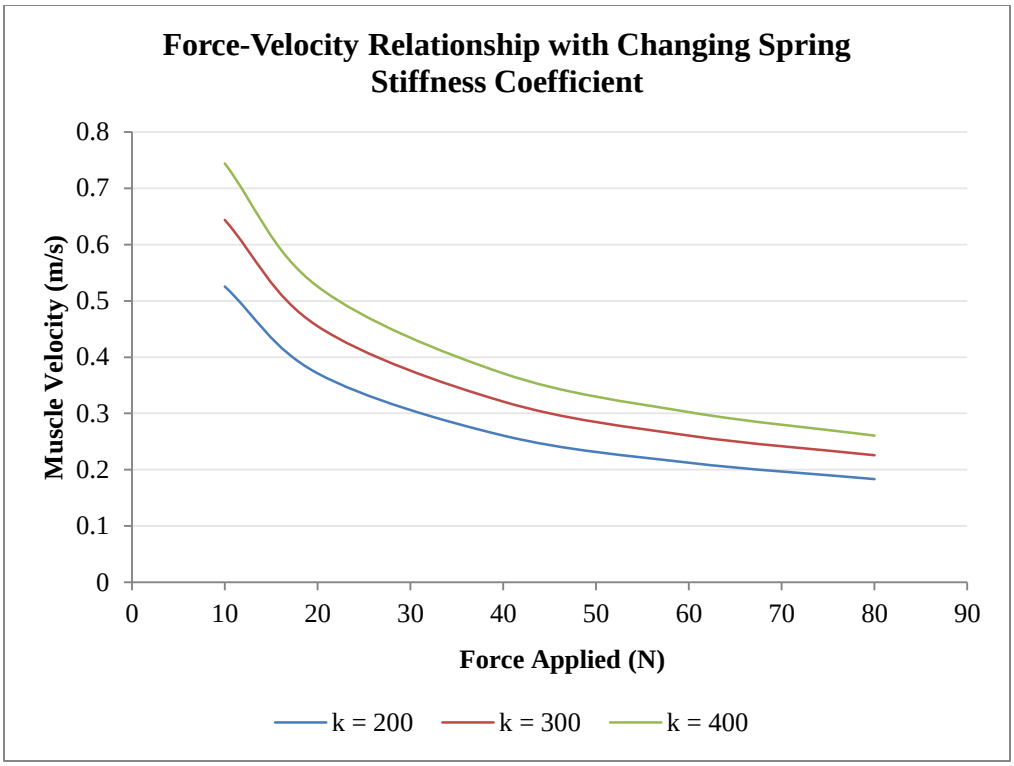

Figure 40: Relationship between the changes in stiffness of the spring of the spring-damper muscle as it pertains to the force-velocity relationship curve. In general, the higher the stiffness the higher the achievable maximum velocity for force loads ranging between 10 and 80N.

As seen above in figure 40, it is apparent that the three different spring stiffness coefficients used follow the same pattern in the force-velocity curve. The major difference is the higher the muscle velocity in a case with spring stiffness of 400 kg/s² compared to spring stiffness of 200 kg/s². This can be explained by the increase in the force produced by the spring of higher stiffness than in a case of a spring with much lower stiffness, given by equation 11. Furthermore, with a change in the damping coefficient, the smaller the expected maximum velocity output is for each applied load. This can be seen below in figure 41. For the produced data depicted in figure 41, the spring stiffness was held at 300 kg/s² as previously used for all other simulations. As depicted below, the variance is slight between no damping and extreme damping. However, it still follows the described trend that higher damping causes higher resistive force, so lower maximum muscle velocities.

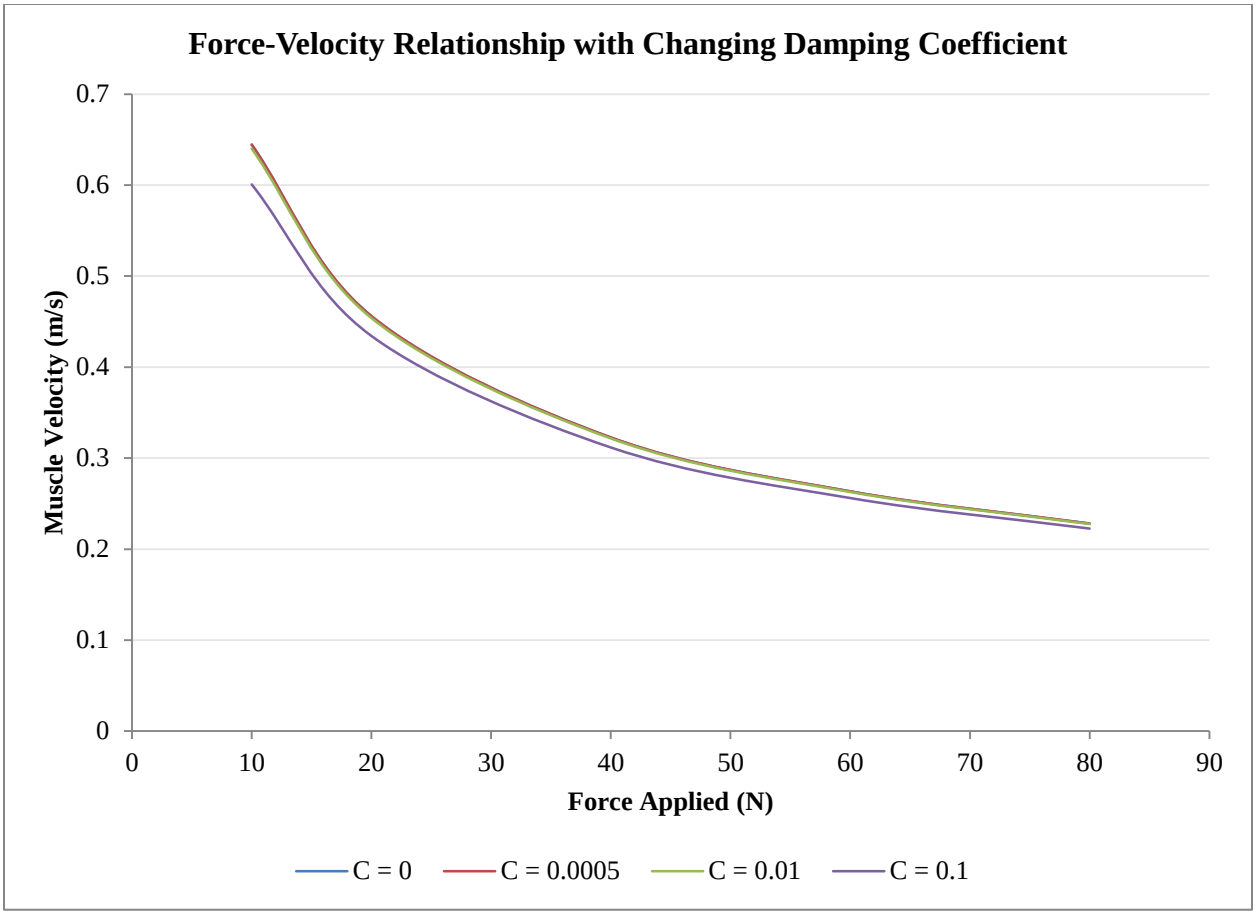

Figure 41: Relationship of increasing damping coefficient on the force-velocity relationship curve. As observed, the increase in damping coefficient causes a decrease in the maximum achievable velocity for a given load. In this case, the case with a damping coefficient of 0.1 kg/s causes the greatest variation away from the zero-damping case. Although this is a slight change, it is justifiable for the simulation to produce data as such. Suggested previously, the increase in damping coefficient increases the resistance to motion. In this case, the motion being resisted is the contraction of the spring.

6.5: Case 5: Spring – Damper Muscle Force with Consideration of Gravity and Reaction Force

The main purpose of this simulation is to ultimately simulate the jumping of a locust. Previous iterations have failed to fully simulate the jumping because of the lack of ground reaction forces acting on the leg of the locust. Thus, up until this point only a locust leg kick has been observed through the simulations. Below, in figure 42, the force-velocity curve relationship can be observed.

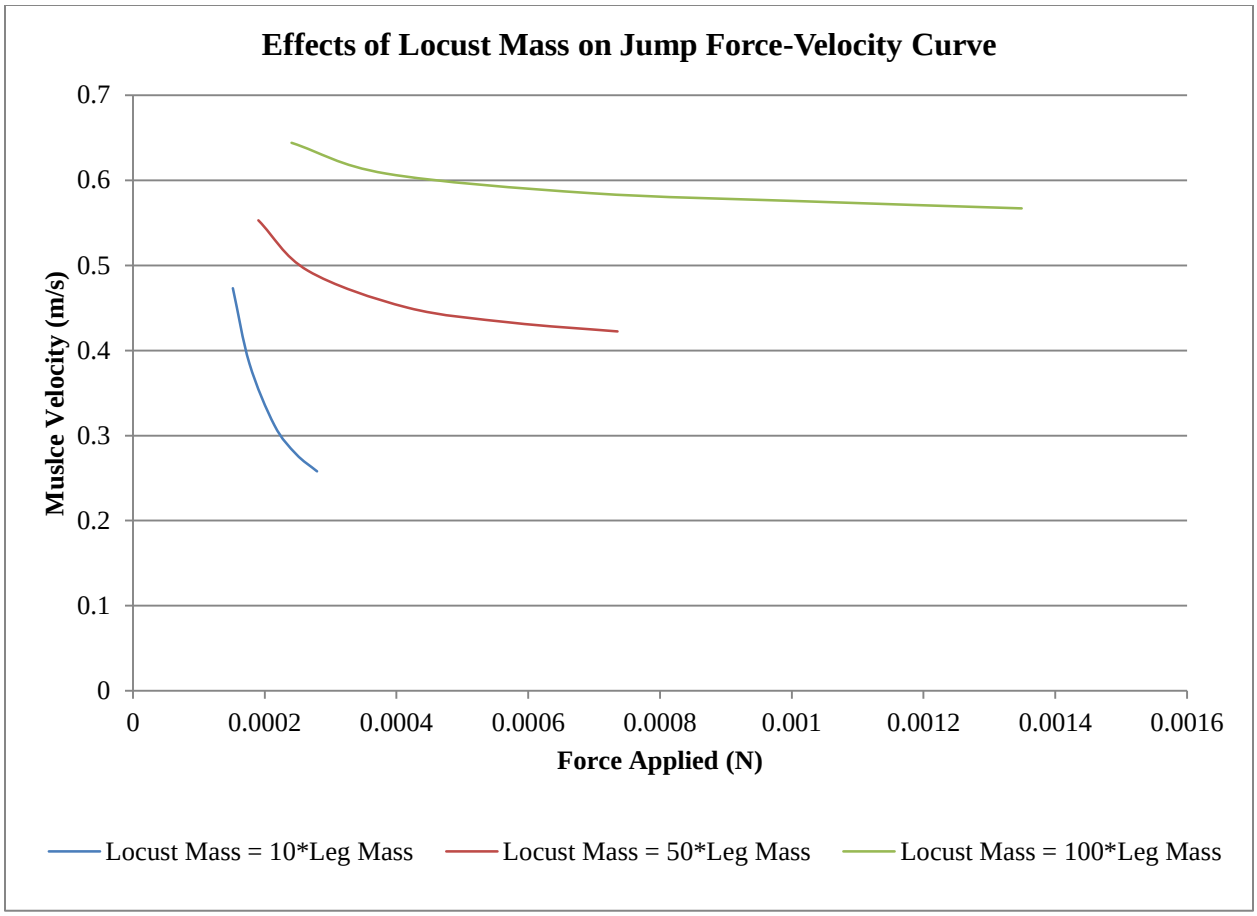

Figure 42: Force Velocity Relationship for varying locust masses during a jump. Locust mass multipliers of 10, 50 and 100 were used to observe the effects of weight on the maximum velocity output and force-velocity relationship curve. As observed, a locust weighing 100 times had higher muscle velocity with a wider range of forces. The locust weight only 10 times the mass of the leg observed the lowest muscle velocities.

As seen in figure 42, a locust weighing only 10 times the leg mass had the lowest muscle velocity and applied forces. This is in part due to the higher effects on gravity within this model on a locust of this size. As suggested through literature, the effects of not only viscous drag, but gravitational effects, on organisms of smaller body size cause greater effects on the force-velocity curve for that organism [30]. In this case, the gravitational effect on the smaller locust outweighs the potential to achieve higher muscle velocities and applied forces. The opposite holds true for the larger locust, with 100 times the leg mass. These results are expected to that of what has been seen within literature of organism locomotion.

6.6: Case 6: Spring – Damper Muscle Force with Consideration of Gravity and Drag Force

The last simulation accomplished dealt with the effects of viscous drag on a fin, rather than a locust leg. Varying percent glycerine solutions were used to obtain the density necessary for the drag force equation. Only two leg masses were used in this case, 10 mg and 80mg, while the damping force remained at 0.5 kg/s. The results can be shown in tables 5 and 6 for 10mg and 80mg fin masses, respectively.

10 mg Fin Mass		
Percent Glycerine	**Muscle Velocity**	**Viscous Force**
%	*m/s*	*N*
0	0.006589388	0.025056829
25	0.006396227	0.025063626
50	0.006205593	0.025070334
75	0.006025927	0.025076657
100	0.005866399	0.025082271

Table 5: Data related to viscous force and muscle velocity on a 10mg fin on varying percent glycerine solutions. The results yield data that shows as the viscous force increases due to the resistance to higher velocities, the muscle velocity decreases. Further, as the percent glycerine solution increases to a highly viscous environment, the muscle velocity drastically decreases.

80mg Fin Mass		
Percent Glycerine	**Muscle Velocity**	**Viscous Force**
%	*m/s*	*N*
0	0.006567089	0.024716744
25	0.006374493	0.02472359
50	0.006184428	0.024730342
75	0.006005303	0.024736712
100	0.005846262	0.024742373

Table 6: Similarly to the data presented for a fin mass of 10mg, an 80mg fin has decreasing velocity with increasing viscous forces and percent glycerine solution. The results show that the 80mg fin has lower muscle velocities than the 10mg fin for all percent glycerine solutions.

The results are as expected, the higher the percent glycerine solution the higher the density will be and the lower the output velocity. With an increase in the density the viscous

force will be increased slightly, but the overall change in viscous force is due to the reaction of the fluid to higher muscle velocities trying to actuate within the solution.

6.8: Effects of Varying Actuator Types to Propagate Leg Kick

The effects of differing actuator types are exemplified through Cases 1, 2a, 2b, and 3. The first case, being the simplest, only involved the use of a constant, controllable applied force. It was observed that this was not truly representative of a muscle, as the force over the duration of the leg kick did not lose energy. However, valuable data was shown through the depictions of angular displacement, translational leg velocity, and rate of change of angular momentum of the constant system, through figures 32, 33, and 34, respectively. Under varying changes of mass, the maximum angular displacement achieved decreased as mass increased. This should hold true because of the higher moment of inertia, for which the leg mass is accounted by within the Case 1 model. By definition, moment of inertia is the tendency of a body to resist angular acceleration. The additional weight added to the leg is resisting the muscle's force to want to accelerate in a kicking fashion. Secondly, with the increase in leg mass, the translational velocity of the lower leg drastically decreases. In a similar explanation to the moment of inertia, the increase in leg mass causes for decreases in the maximum allowable translational velocity for the leg. Although the actuator presented in this case was not a comparable to an actual muscle, it was an important case to propagate Case 2b, and 3 from, and began as a starting point to build the model presented in Cases 4, 5, and 6.

The second type of muscle employed was the use of a single spring in Case 2a and 2b. The spring itself allows for proper energetics of the system to be observed, but lacks the ability to have an intrinsic damping effect to resist the rotational motion of the lower leg. Simply put, the springs simulated in this case wanted to rotate. Although the decreases in the translational velocity were observed with increase in mass, it is understood through Hill-type muscles that at some point the resistive forces will cause either a constant maximum output velocity to be achieved or decrease in maximum output velocity. This was, however, observed in Case 3, with the addition of a damper to the actuator, and can be visualized in figure 43 below. In general, the decrease in maximum achievable translational velocity between the masses is still observed. However, there is a logarithmic nature to the curve for each mass simulated. This is what is

expected of a Hill-type muscle, not only in relation to the effects mechanical advantage has on the system, but the effects of a damper wanting to resist the contraction of an ideal spring.

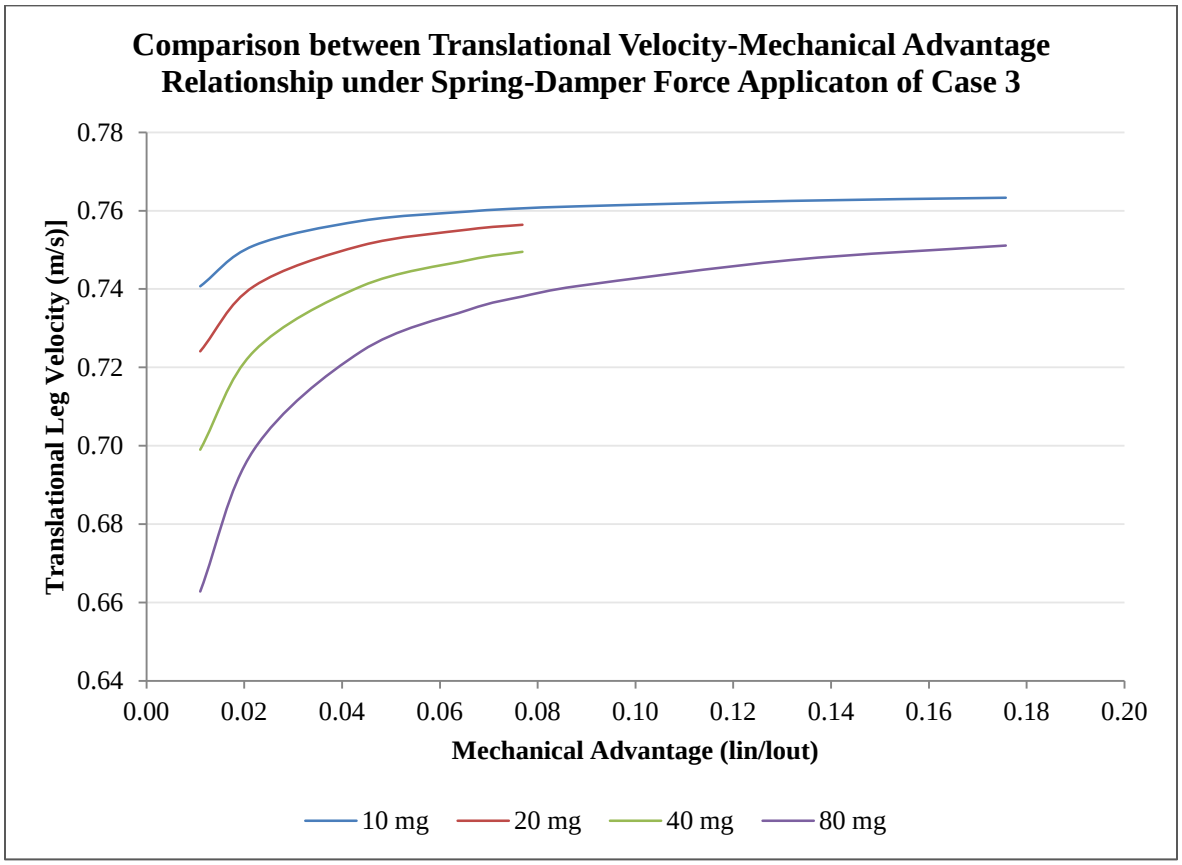

Figure 43: Graphical representation of the effects of adding a damper to the actuator. The above shows what is expected of a Hill-type muscle, for the translational velocity of the lower leg follows a logarithmic trend to resist the rotation of the lower leg as mechanical advantage increases.

6.9: Effects of External Forces on Simulation Model

External forces were observed through the simulations of Cases 4, 5, and 6 on inertial loading, ground reactant force loading, and viscous force loading. Each of these was observed to follow the general shape of a Hill-type muscle through the force-velocity relationship curve. Looking at case 4, the effects were seen drastically in the variance of damping coefficient and spring stiffness of the system. The only external force added to the system for this case, was the inertial loading of the leg mass resolved about a distance of l_{out} from the knee joint of the leg. Looking at figure 40 and 41, it is clear to see that as the inertial load increases the muscle

shortening velocity decreases with respect to changes in both damping coefficient and spring stiffness.

Moving onto Case 5, the same decaying relation between force and muscle velocity was observed. As stated previously, this simulation held the damping coefficient at 0.5kg/s because it was large enough to visibly see the effects within the simulation on the force-velocity relation. Moreover, the locust mass was assumed to be 10 times the leg mass for the nominal case, while observations were made for 50 times the leg mass and 100 times the leg mass. Looking at figure 42, it is apparent that Case 5 yields similar results to that of Case 4. However, the main difference lies within the trend between the assumed locusts' leg mass. There is an understandable increase in the maximum achievable velocity as the locusts' mass increases. This is because the higher the mass of the body the larger the reaction force output onto the ground. Due to equal and opposite reactions, this same force is acted back onto the locust as it jumps. Thus, with a higher body mass a higher reaction force will be achieved along with a higher maximum muscle velocity.

Lastly, the viscous loading effects were observed on a fin, similar in shape to the locust leg geometry. Looking at tables 5 and 6, it can be inferred that as the viscous force increases on the fin during actuation, the muscle velocity decreases. This is in part due to the damper of the muscle, but also the resistance of the viscous fluid onto the fin. Thus, being able to see this inference from the physical data, it is understood that the viscous forces acting on the fin cause a similar force-velocity relationship seen in Cases 4 and 5. However, the relationship does not represent an exponentially decaying graph. Instead, figure 44 shows that the trend between the viscous force acting on the muscle from varying glycerine solutions is linear to the muscle velocity. This has been concluded to be due to the relationship of the viscous drag force to the muscles velocity through equation 22. The square of the viscous force is approximately that of the muscle velocity, and the damping force can account for the variance between the muscle velocity observed and the viscous force.

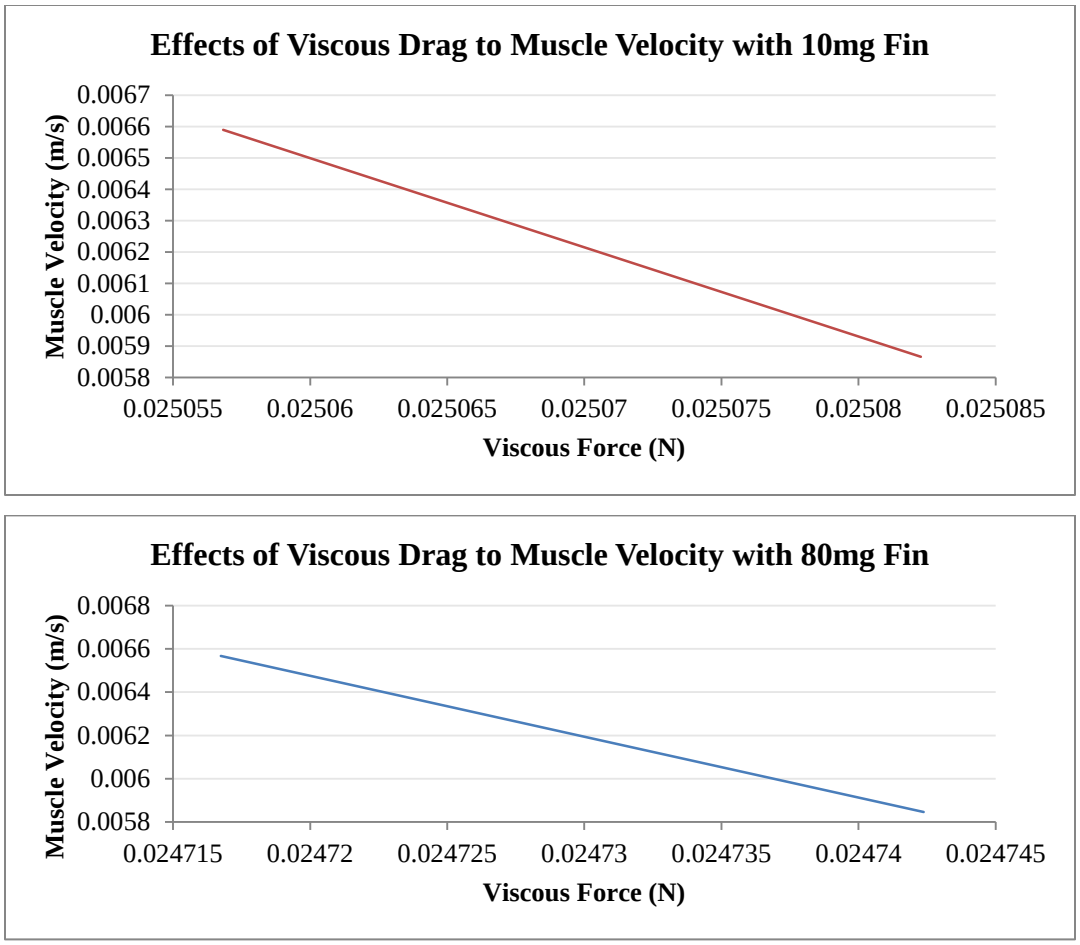

Figure 44: Comparison between the 10mg and 80mg fin. It is observed that the viscous force squared is almost equivalent to that of the muscle velocity, which hold true from equation 22 defining viscous drag. Although this is not an exponential decay with the relation to the Hill's force velocity curve, it does represent a decrease in the muscle velocity with increasing viscous resistance.

6.10: Validation Data from Experimental Testing

The experimental tests aimed to validate the data shown through the theoretical simulations. Force loading, inertial loading, and viscous loading cases were tested as discussed in Chapter 5. It should be noted that the data for each case and trial were conducted on separate days and times. This aided in the randomization of the test, and subsequently determines repeatability of the testing. Overall, the results from the force loading tests yielded the most useful data, in regards to this thesis project. Two cases of damping were observed: minimal and maximum. The results are shown in figures 45 and 46, respectively.

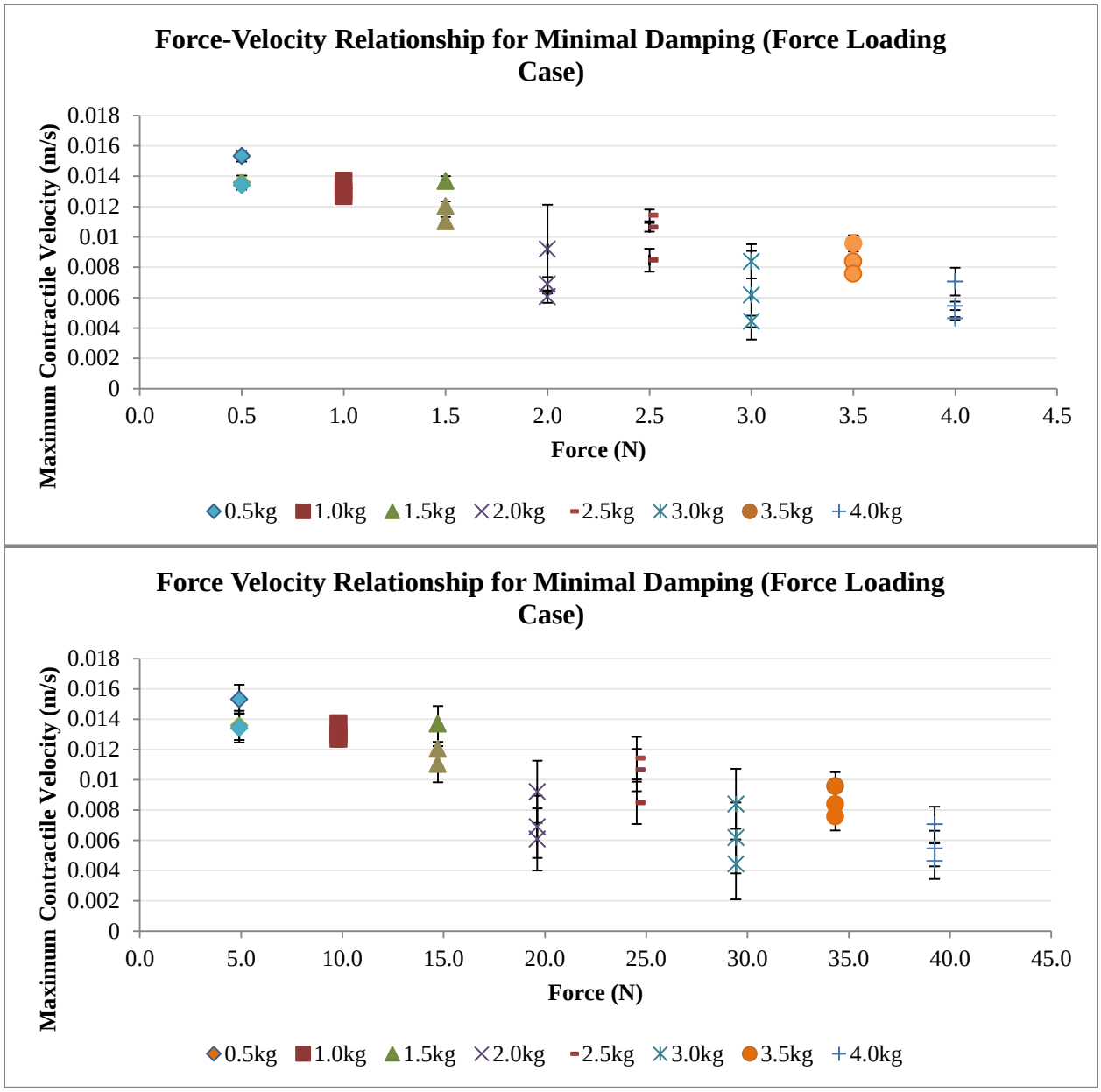

Figure 45: Minimal damping case under force loading conditions. The weights were applied to the spring-damper 'muscle' directly through the use of a weight basket. It can be seen that there is an apparent decrease in the data from 0.5kg to 4.0kg applied load. Three trials were accomplished for each loading case, and three contractions are related to each data point. The top graph shows the standard deviation of contractions per load trial, while the bottom graph shows the standard deviations between all trials.

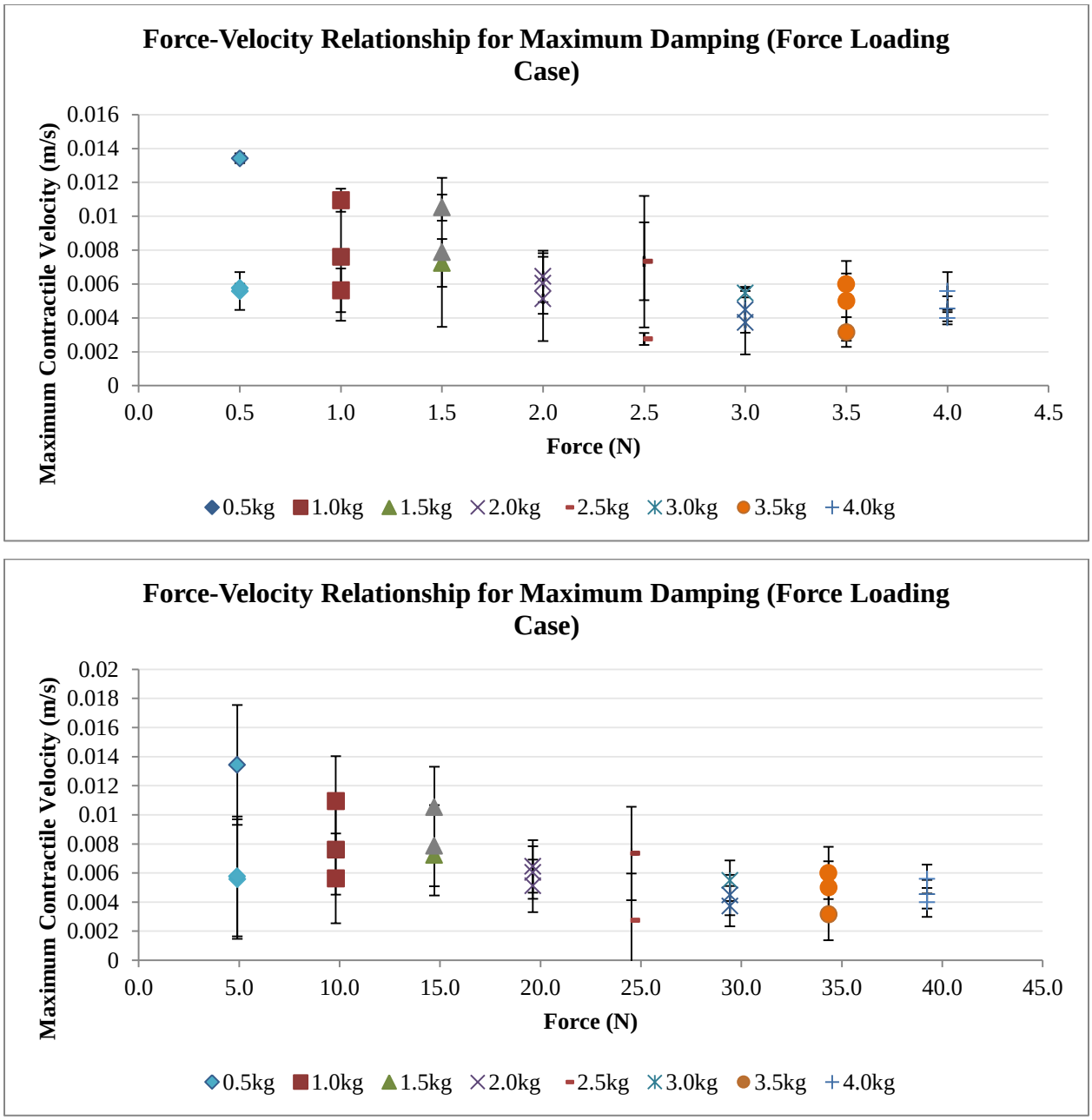

Figure 46: Maximum damping case with applied load directly onto the spring-damper 'muscle'. Slight appearance of decrease in the contractile force as the load increases from 0.5kg to 4.0kg. Three trials were accomplished in a similar fashion to the minimal loading case, where each data point represents an average of three contractions. The top graph shows the standard deviation of contractions per load trial, while the bottom graph shows the standard deviations between all trials.

As observed, the minimal damping case yielded the best data. Not only are the results repeatable, but the results clearly show a trend between the contractile velocity of the spring-damper 'muscle' and the applied load. However, this trend was not as clear for the maximum

damping force tests. It is evident that there is a slight decrease in the contractile velocity between the loads, but the standard deviation is much greater and causes overlap between these loads. Moreover, the average percent error between the three trials was extremely high, as observed in table 7.

Loading	**Average Percent Difference**
kg	*%*
0.5	55.164
1.0	78.154
1.5	35.435
2.0	17.063
2.5	60.696
3.0	27.347
3.5	43.580
4.0	32.199

Table 7: Percent Difference between All Three Trials of Force Loading Experimental Case with Damping

These errors could be due to the two degrees of freedom along the spring-damper 'muscle'. During contraction the muscle will contract in a manner of the least resistance. With the maximum damping force case, the spring-damper 'muscle' rotated about the Z-axis for some loading trials due to it being the path of least resistance to the contraction. However, these trials were repeated for proper data. Modifications to correct for this issue will be further discussed in Chapter 7.

The inertial loading and viscous force cases yielded the worst data of all the experiments, due to the lack of force-velocity relationship. Since the minimal damping force gave the best results for the force loading case, it was implemented for the experimentation of both the inertial and viscous loading tests. The force-velocity curves for each can be seen in figures 47 and 48, respectively.

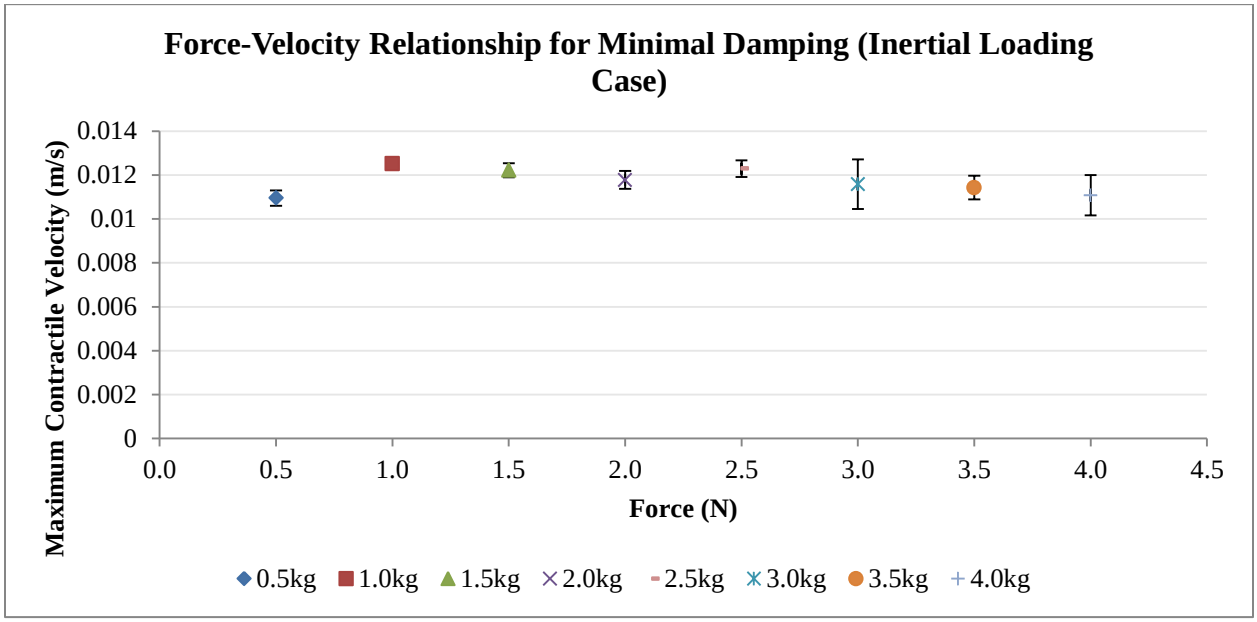

Figure 47: Force-velocity relationship for inertial loading case, under minimal damping conditions. There no trend observable between the force loading and contractile velocity of the muscle that is related to the Hill's muscle model.

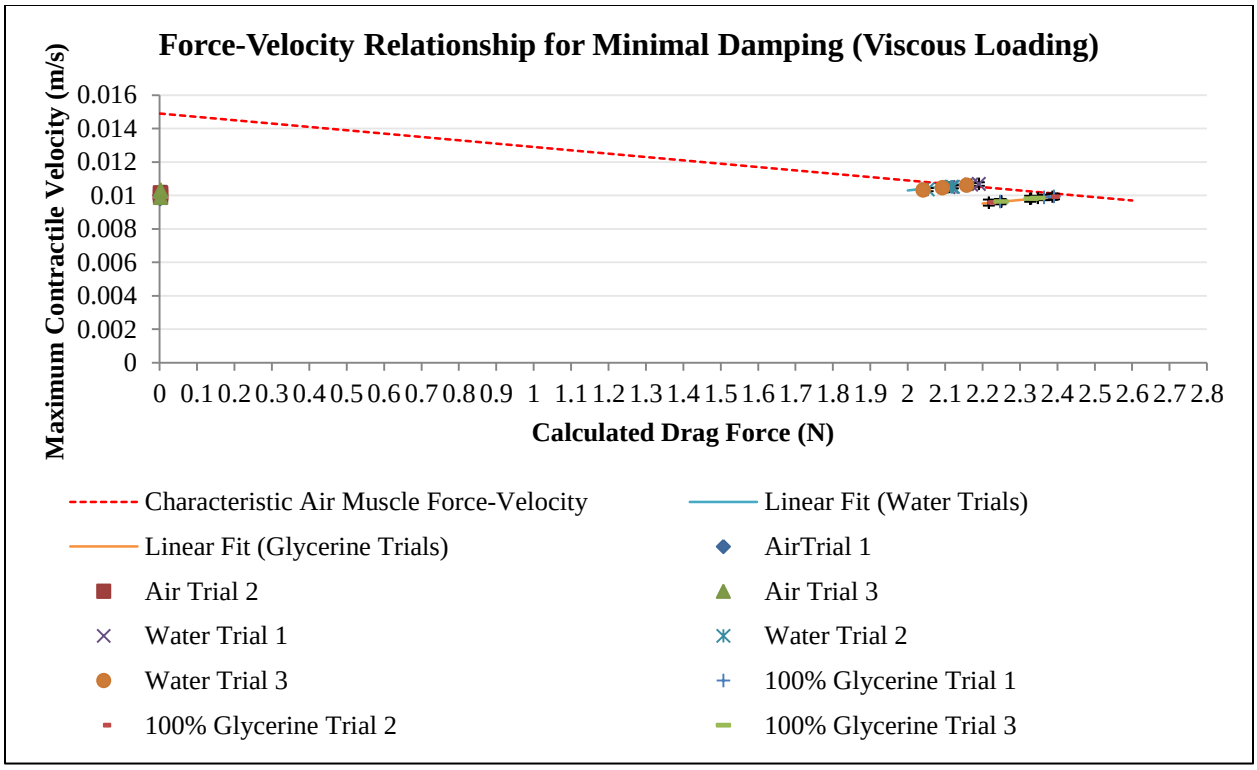

Figure 48: Relationship between force-velocity of the spring-damper 'muscle' under viscous loading conditions in air and water. As seen above, the data between each viscous fluids trials are greatly related, but there is no correlation between the viscous force and the contractile velocity of the experimental muscle.

The issues associated with the data could be due to the limitations of the test fixture. The linear potentiometer of the test fixture has a 10V maximum. This is correlated to a 1 inch change in distance. Due to this, the McKibben air muscle could only be built to actuate less than 1 in. The motion of the air muscle is already slight, so the addition of indirect test fixtures, such as the inertial test bed and the viscous test bed, do not actuate much. This limitation could cause for the discrepancies of the force-velocity curves for the inertial and viscous loading experiments. Modifications to negate this issue will be later presented in Chapter 7.

Chapter 7: Conclusion

7.1: Overview

This thesis aimed to present a working theoretical model for a simple MSK lever system that included a muscle, a lever, and a load. Various cases were explored. This included varying properties of the muscle, ranging from a simplistic constant force, to a spring damper system that replicated the Hill muscle equation. The cases also included varying the resistive forces acting on the lever. For every combination of muscle and resistive force, the gearing was varied in order to explore the effect of gearing on the MSK system.

Cases 4, 5, and 6 clearly show that the use of a theoretical spring-damper 'muscle' follows similar trends to the Hill's muscle model. More specifically, these cases clearly depict the proper force-velocity relationship where with increasing loads acting on the muscle, there will be a decrease in the muscle velocity. Furthermore, it is observed through Case 3, that the spring-damper in parallel produces data related to the translational velocity of the rotating body and mechanical advantage that represent a biological muscle.

Experimental data did further the validation of the theoretical model for the force loading case, as it gave the most promising data. Not only was the data repeatable between trials, but the data clearly showed a trend between the force-velocity relation for the minimal damping case. Although there was slight relation with the maximum damping case, it was apparent that changes need to be made to the test fixture prior to obtaining better data. Moreover, the viscous and inertial loading cases presented data that was unhelpful in the sole purpose of validating the theoretical model. It was seen that there were issues pertaining to the test fixtures capabilities that need to be addressed for better validation of this model.

7.2: Future Research Opportunities

There are several opportunities for future research regarding both the theoretical and experimental models. In relation to the theoretical model, further research should be accomplished on the viscous force case. As presented previously, data showed a linear trend between the viscous force and the muscle velocity of Case 3. For future work to obtain a proper force-velocity curve, iterations of varying damping force should be explored. Although it is understandable the relation between the viscous force and muscle velocity in equation 22, a higher or lower damping force might be able to obtain the force-velocity curve. Moreover the

theoretical model should be assessed on another biological system to validate the usability and continuity of the model to represent all MSK lever systems. This is a rather large area of research, but better data may be available regarding MSK physiology of humans or other large organisms. Furthermore, the application of a theoretical model to a larger MSK system might allow for better comparability to the experimental models that utilize the McKibben air muscle in parallel with dampers.

Lastly, major research can be conducted on the use of McKibben air muscles in parallel with dampers. As observed in this thesis project, only the force loading scenario provided fruitful data. This was concluded to be associated with the limitations of the current test fixture. The linear potentiometer was the limiting factor for this experimental testing. It only was capably of extending an inch past its resting length. Furthermore, it is unwise to run the linear potentiometer to its limits (i.e. 1V and 10V). In order to allow for larger McKibben air muscles, a larger linear potentiometer must be employed. This will allow for a greater contraction in the McKibben air muscle that will actuate the inertial test bed and viscous test bed over a larger range. This may provide better data compared to the current model. In addition to the change in linear potentiometer, the spring-damper 'muscle' must be limited to only one degree of freedom. This will cause the 'muscle' to only actuate in the Z-axis, and provide stronger data for the maximum damping force experimentation.

References

[1] McDowell, J. 2010, *Encyclopedia of Human Body Systems*, Greenwood, Westport, CT.

[2] Ren, L., Qian, Z. and Ren, L., 2014, "Biomechanics of Musculoskeletal System and Its Biomimetic Implications: A Review," Journal of Bionic Engineering, **11**(2), pp. 159–175.

[3] Singh, A.P., 2012, "Cortical Bone and Cancellous Bone," from http://boneandspine.com/cortical-bone-and-cancellous-bone/.

[4] "Chapter 6: Bones and Skeletal Tissues,"n.d., http://classes.midlandstech.edu/carterp/courses/bio210/chap06/lecture1.html.

[5] Pruitt, L.A. and Chakravartula, A.M., 2011, *Mechanics of biomaterials: fundamental principles for implant design*, Cambridge University Press, Cambridge.

[6] King, B.G., Showers, M.J. and Innes L.C., 1969, *Human anatomy and physiology,* Saunders, Philadelphia, PA.

[7] "Trabeculae," from http://www.trabecularbone.org/cortical-bone/.

[8] "BME 332: Bone Structure-Function," from http://www.umich.edu/~bme332/ch9bone/bme332bone.htm.

[9] Kimball, J.W., 1965, *Biology,* Addison-Wesley Pub. Co., Palo Alto, CA.

[10] "Chapter 9: Muscular Movement and Control," n.d., from https://droualb.faculty.mjc.edu/lecture notes/unit 3/chapter_9_muscle_movement with figures.htm.

[11] Krans, J.L., 2010, "The Sliding Filament Theory of Muscle Contraction." Nature Education, **3**(9), pp.66.

[12] Nordin, M. and Frankel, V.H., 2001, *Basic biomechanics of the musculoskeletal system,* Lippincott Williams & Wilkins, Philadelphia, PA.

[13] Azizi, E., Brainerd, E.L. and Roberts, T.J., 2007, "Variable gearing in pennate muscles," *Proceedings of the National Academy of Sciences*.

[14] Baratta, R.V., Solomonow, M., Best, R. and D'Ambrosia, R., 1998, "Force, velocity and energy dynamics of nine load-moving muscles," Medical Engineering & Physics, **19**(1), pp. 37-49.

[15] Leyland,T. "Simple Biomechanical Models : Introduction to Static Equilibrium." from http://www.sfu.ca/~leyland/Kin201%20Files/SimpleModels.pdf

[16] Schafer, R.C., 1987, *Clinical biomechanics: musculoskeletal actions and reactions*, 2nd ed., Williams & Wilkins, Baltimore, MD.

[17] Pichtikova, M., 2014, "Back Tuck – Biomechanics Ex. Science Summative," from http://butlersbacktuck.weebly.com/conclusion.html.

[18] Seow, C.Y., 2013, "Hill's equation of muscle performance and its hidden insight on molecular mechanisms," The Journal of General Physiology, **142**(6), pp. 561–573.

[19] "Muscle Tension-Velocity," from http://www.brown.edu/Departments/Engineering/Courses/En123/Lectures/HillEqn.htm.

[20] Hill, A.V., 1938, "The heat of shortening and the dynamic constants of muscle,"Proceedings of the Royal Society: Biological Sciences, **126**(843), pp. 135-195.

[21] Göktepe, S., Menzel, A. and Kuhl, E., 2014, "The generalized Hill model: A kinematic approach towards active muscle contraction," Journal of the Mechanics and Physics of Solids, **72**, pp. 20–39.

[22] Haeufle, D., Günther, M., Bayer, A. and Schmitt, S. "Hill-type muscle model with serial damping and eccentric force–velocity relation," Journal of Biomechanics,**47**(6), pp. 1531–1536.

[23] Raabe, M.E. and Chaudhari, A.M., 2016, "An investigation of jogging biomechanics using the full-body lumbar spine model: Model development and validation," Journal of Biomechanics, **49**(7), pp. 1238–1243.

[24] Monsabert, B.G.D., Vigouroux, L., Bendahan, D. and Berton, E., 2014, "Quantification of finger joint loadings using musculoskeletal modelling clarifies mechanical risk factors of hand osteoarthritis," Medical Engineering & Physics, **36**(2), pp. 177–184.

[25] Basafa, E., Murphy, R.J., Gordon, C.R. and Armand, M., 2014, "Modeling the biomechanics of swine mastication – An inverse dynamics approach," Journal of Biomechanics, **47**(11), pp. 2626–2632.

[26] Shourijeh, M.S., McPhee, J., "Forward Dynamic Optimization of Human Gait Simulations: A Global Parameterization Approach." Journal of Computational Nonlinear Dynamics, **9**(3).

[27] Shourijeh, M.S., Smale, K.B., Potvin, B.M. and D. L. Benoit, 2016, "A forward-muscular inverse-skeletal dynamics framework for human musculoskeletal simulations," Journal of Biomechanics, **49**(9), pp. 1718–1723.

[28] Lloyd, D.G. and Besier, T.F.,2003, “An EMG-driven musculoskeletal model to estimate muscle forces and knee joint movements in vivo,” Journal of Biomechanics, **36**(6), pp. 765-776.

[29] Fitzpatrick, C.K. and Rullkoetter, P.J., 2014, “Estimating total knee replacement joint load ratios from kinematics,” Journal of Biomechanics, **47**(12), pp. 3003–3011.

[30] Azuma, A., 2006, *The biokinetics of flying and swimming*, American Institute of Aeronautics and Astronautics, Reston, VA.

[31] Gregersen, C.S. and Carrier, D.R., 2004, “Gear ratios at the limb joints of jumping dogs,” Journal of Biomechanics, **37**(7), pp. 1011–1018.

[32] Daley, M.A., Usherwood, J.R., Felix, G. and Biewener, A.A., 2006, “Running over rough terrain: guinea fowl maintain dynamic stability despite a large unexpected change in substrate height,” National Center for Biotechnology Information.

[33] Richards, C.T., “Building a robotic link between muscle dynamics and hydrodynamics,” The Journal of Experimental Biology, **214**(14), pp. 2381-2389.

[34] Maynard Smith, J. and Savage, R. J. G., 1956, “Some Locomotory Adaptations in Mammals,” Journal of the Linnean Society of London, Zoology, **42**(288), pp. 603-622.

[35] McHenry, M. and Summers, A., 2011, “A force-speed trade-off is not absolute,” Biology Letters, **7**(6), pp.880-881.

[36] Oufiero, C.E., Holzman, R.A., Young, F.A. and Wainwright, P.C., 2012, “New insights from serranid fishes on the role of trade-offs in suction-feeding diversification,” Journal of Experimental Biology, **215**(21), pp.3845-3855.

[37] Blanco, M.M. and Patek, S.N., 2014, “Muscle trade-offs in a power-amplified prey capture system.,” Evolution, **68**(5), pp. 1399–1414.

[38] Edman, K.A.,1979, “The velocity of unloaded shortening and its relation to sarcomere length and isometric force in vertebrate muscle fibres.,” The Journal of Physiology, **291**(1), pp.143-159.

[39] Herrel, A., Podos, J., Vanhooydonck, B. and Hendry, A.P., 2008, “Force-velocity trade-off in Darwin's finch jaw function: a biomechanical basis for ecological speciation?,” Functional Ecology, **23**(1), pp.119-125.

[40] Van Wassenbergh, S., Herrel, A., Adriaens, D. and Aerts, P., (2007), "No trade-off between biting and suction feeding performance in clariid catfishes," Journal of Experimental Biology, **210**(1), pp.27-36.

[41] Mchenry, M. J., 2011, "There is no trade-off between speed and force in a dynamic lever system," Biology Letters, **7**(3), pp.384-386.

[42] "Shape Effects on Drag," 2015, from https://www.grc.nasa.gov/WWW/K-12/airplane/shaped.html.

[43] "Density of Glycerine-Water Solutions," from http://edge.rit.edu/edge/P13051/public/Research Notes/Density of Aqueous Glycerol Solutions.pdf.

[44] Phatak, A., 2016, "Relationship Between Force Applied and Velocity of Contraction of Air Muscle," M.S. thesis, Department of Mechanical Engineering, Rochester Institute of Technology.

[45] Chou, C.P. and Hannaford, B., 1996, "Measurement and modeling of McKibben pneumatic artificial muscles," IEEE Transactions on Robotics and Automation, **12**(1), pp. 90–102.

[46] Chou, C.P. and Hannaford, B., 1994, "Static and dynamic characteristics of McKibben pneumatic artificial muscles," *IEEE International Conference on Robotics and Automation,* San Diego, CA, pp. 281-286.

[47] Zhang, Z. and Philen, M., 2011, "Pressurized artificial muscles," Journal of Intelligent Material Systems and Structures, **23(**3), pp. 255–268.

[48] Tondu, B., Boitier, V. and Lopez, P., 1994, "Naturally compliant robot-arms actuated by McKibben artificial muscles," *IEEE International Conference on Systems, Man, and Cybernetics,* San Antonio, TX, pp. 2635-2640. Characterization and modeling of air muscles

[49] Bertetto, A.M. and Ruggiu, M.,2004, "Characterization and modeling of air muscles," Mechanics Research Communications, **31**(2), pp. 185–194.

[50] Andrikopoulos, G., Nikolakopoulos, G. and Manesis, S., 2013, "Pneumatic artificial muscles: A switching Model Predictive Control approach," Control Engineering Practice, **21**(12), pp. 1653–1664.

[51] “Levers and Body Parts” from https://www.biologycorner.com/worksheets/articles/levers_body.html.

Appendix A: Case 1 – Constant Applied Force Simulation Documents

Case 1 Simulink Block Diagram

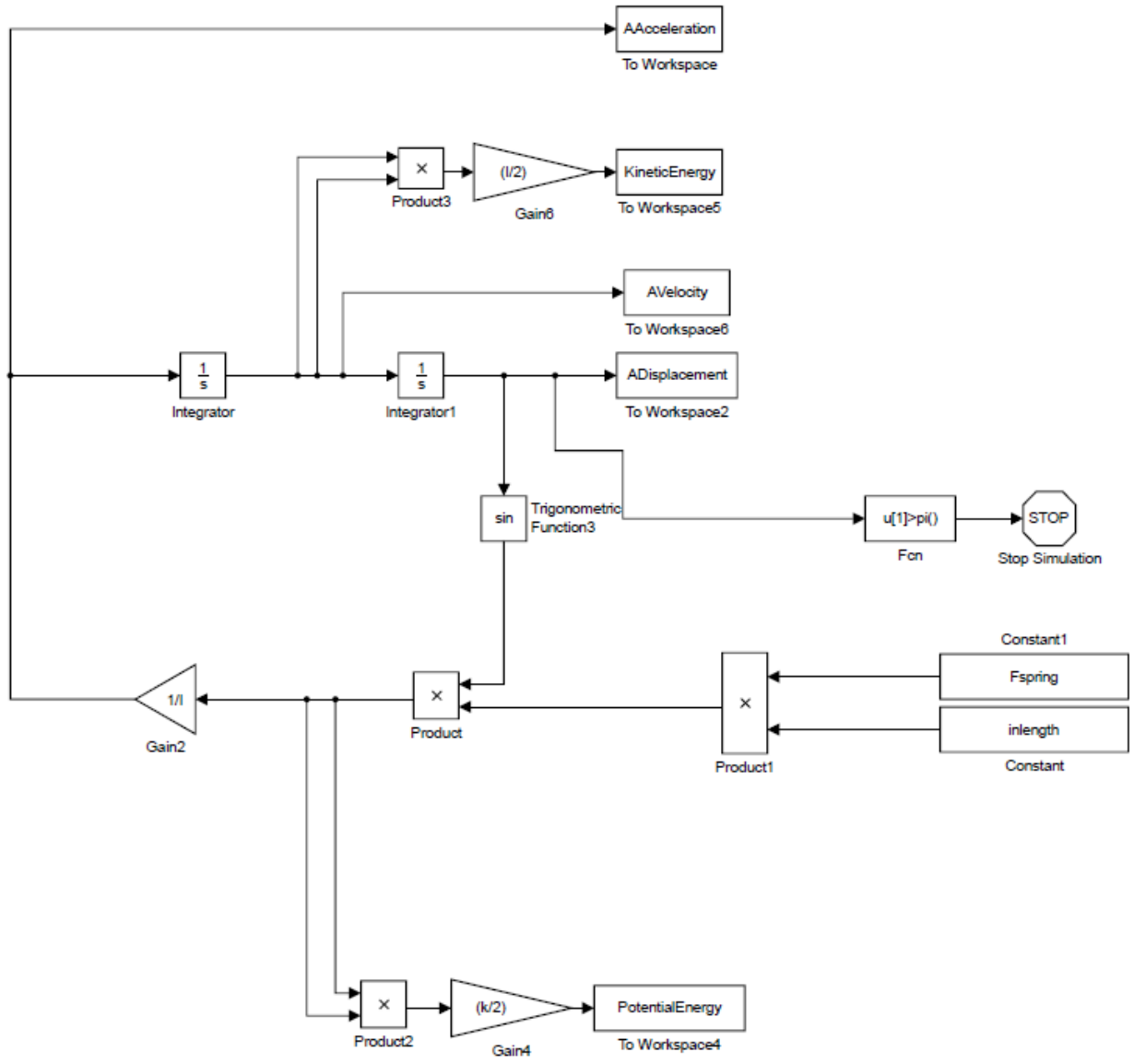

Case 1 MATLAB Code

```
%% Case 1: Constant Force
% Created by: Jenna Hopkins

close all
clear all
clc
```

```
k = .3e3; %N/m
inlength = (7.6e-4)+((7.6e-4)*0)%m
sstretch = 1.5e-3; %m
L = sstretch;%m
m = 10e-6; %kg
theta0 = 6*(pi()/180);%rad
lleg = 30e-3; %m
I = (m/3)*((lleg/2)^2); %kg-m^2
outlength = 1.73e-2; %m

Fspring = k*L; %N
F = ones(57,1); % Vector containing all 1's
Fspring_matrix = Fspring.* F; % Vector containing Constant Force
MA = inlength/outlength;  % Mechanical Advantage of System


sim('Sim_Locust')
% Output of Simulink Data with ODE45
AAcceleration1 = AAcceleration*(180/pi()); % Angular Acceleration [deg/s^2]
AVelocity1 = AVelocity*(180/pi()); % Angular Velocity [deg/s]
ADisplacement1 = ADisplacement*(180/pi()); % Angular Displacement [deg]

% Correcting Simulation Output
j = size(ADisplacement1);

for i = 1:j % Correcting all output vectors for last index before simulation goes over
180 degrees
    if ADisplacement1(i) < 180
        ADisplacementc(i) = ADisplacement1(i);
        AAccelerationc(i) = AAcceleration1(i);
        KineticEnergyc(i) = KineticEnergy(i);
        AVelocityc(i) = AVelocity1(i);
        PotentialEnergyc(i) = PotentialEnergy(i);

    end
end

LAcceleration1 = (AAccelerationc*pi()/180)*outlength; % Lineaer Acceleration [m/s^2]
LVelocity1 = (AVelocityc*pi()/180)*outlength; % Linear Velocity [m/s]
LDisplacement1 = (ADisplacementc*pi()/180)*outlength; % Linear Displacement [m]

% Obtain Maximums of Kinematics
Max_AAcceleration = max(AAccelerationc); % Maximum Angular Acceleration [deg/s^2]
Max_AVelocity = max(AVelocityc); % Maximum Angular Velocity [deg/s]
Max_ADisplacement = max(ADisplacementc); % Maximum Angular Displacement [deg]

Max_LAcceleration = max(LAcceleration1); % Maximum Linear Acceleration [m/s^2]
Max_LVelocity = max(LVelocity1); % Maximum Linear Velocity [m/s]
Max_LDisplacement = max(LDisplacement1); % Maximum Linear Displacement [m]

Max_ForceInput = max(Fspring_matrix); %Maximum Spring Force [J]
Max_PotentialEnergy = max(PotentialEnergyc); %Maximum Potential Energy [J]
Max_KineticEnergy = max(KineticEnergyc); %Maximum Kinetic Energy [J]
rcam = (I.*AAccelerationc);
Max_rcam = max(rcam); %Maximum Rate of Change of Angular Momentum

% Display Data in Command Window
display(MA, 'Mechanical Advantage of System:')
display(Max_LVelocity, 'Maximum Linear Velocity:')
display(Max_ADisplacement, 'Maximum Angular Displacement:')
display(Max_ForceInput, 'Maximum Input Force:')
```

```
% display(Max_KineticEnergy, 'Maximum Output Rate of Change of Angular Momentum:')
display(Max_rcam, 'Maximum Rate of Change of Angular Momentum:')

figure(1) % Figure of Potential Energy vs. Time
plot(tout, PotentialEnergy)
title('Potential Energy during Leg Kick')
xlabel('Time (s)')
ylabel('Potential Energy (J)')

figure (2) % Figure of Constant Force for Entire Time of Simulation
plot(tout, Fspring_matrix, '--r')
title('Spring Force during Leg Kick')
xlabel('Time (s)')
ylabel('Spring Force (N)')
```

Appendix B: Case 2a - Spring Muscle Force in terms of l_{in} Simulation Documents

Case 2a Simulink Block Diagram

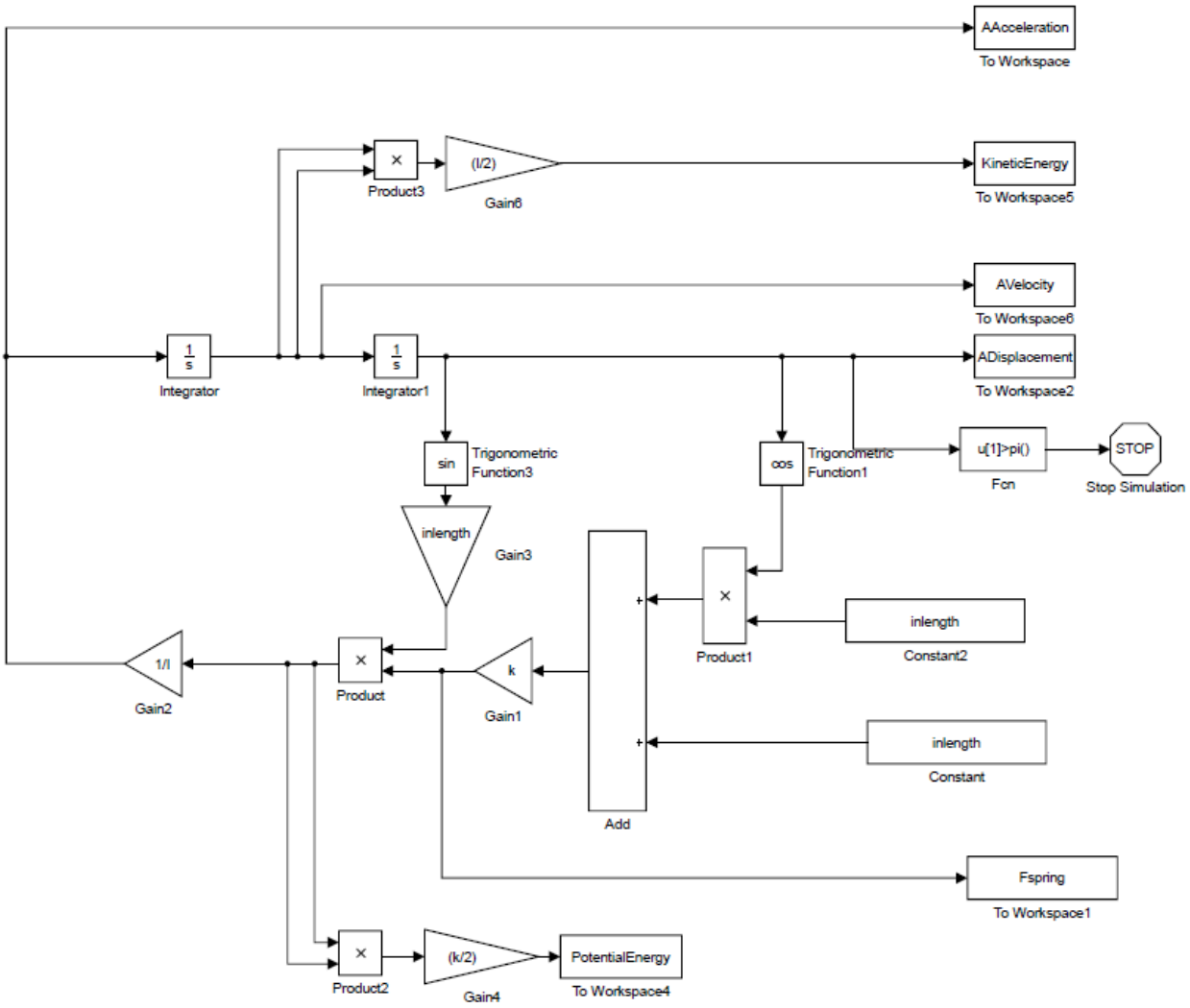

Case 2a MATLAB Code

```
%% Case 2a: Spring Force in terms of lin
% Created by: Jenna Hopkins

close all
clear all
clc

k = .3e3; %N/m
inlength = (7.6e-4)+((7.6e-4)*0);%m
sstretch = 1.5e-3; %m
L = sstretch;%m
m = 10e-6; %kg
```

```
theta0 = 6*(pi()/180);%rad
lleg = 40e-3; %m
I = (m/3)*((lleg/2)^2); %kg-m^2
outlength = 1.73e-2; %m
MA = inlength/outlength; %Mechanical Advantage of the System

sim('Sim_Locust2')
% Output of Simulink Data with ODE45
AAcceleration1 = AAcceleration*(180/pi()); % Angular Acceleration [deg/s^2]
AVelocity1 = AVelocity*(180/pi()); % Angular Velocity [deg/s]
ADisplacement1 = ADisplacement*(180/pi()); % Angular Displacement [deg]
% Correcting Simulation Output
j = size(ADisplacement1);

for i = 1:j % Correction to take data points before simulation is more than 180
degrees
    if ADisplacement1(i) < 180
        ADisplacementc(i) = ADisplacement1(i);
        AAccelerationc(i) = AAcceleration1(i);
        KineticEnergyc(i) = KineticEnergy(i);
        AVelocityc(i) = AVelocity1(i);
        PotentialEnergyc(i) = PotentialEnergy(i);

    end
end

LAcceleration1 = (AAccelerationc*pi()/180)*outlength; % Lineaer Acceleration [m/s^2]
LVelocity1 = (AVelocityc*pi()/180)*outlength; % Linear Velocity [m/s]
LDisplacement1 = (ADisplacementc*pi()/180)*outlength; % Linear Displacement [m]

% Obtain Maximums of Kinematics
Max_AAcceleration = max(AAccelerationc); % Maximum Angular Acceleration [deg/s^2]
Max_AVelocity = max(AVelocityc); % Maximum Angular Velocity [deg/s]
Max_ADisplacement = max(ADisplacementc); % Maximum Angular Displacement [deg]

Max_LAcceleration = max(LAcceleration1); % Maximum Linear Acceleration [m/s^2]
Max_LVelocity = max(LVelocity1); % Maximum Linear Velocity [m/s]
Max_LDisplacement = max(LDisplacement1); % Maximum Linear Displacement [m]

Max_ForceInput = max(Fspring); %Maximum Spring Force [J]
Max_PotentialEnergy = max(PotentialEnergyc); %Maximum Potential Energy [J]
Max_KineticEnergy = max(KineticEnergyc); %Maximum Kinetic Energy [J]
rcam = (I.*AAccelerationc);

Max_rcam = max(rcam); %Maximum Rate of Change of Angular Momentum
% Display Data in Command Window
display(MA, 'Mechanical Advantage of System:')
display(Max_LVelocity, 'Maximum Linear Velocity:')
display(Max_ADisplacement, 'Maximum Angular Displacement:')
display(Max_ForceInput, 'Maximum Input Force:')
display(Max_rcam, 'Maximum Rate of Change of Angular Momentum:')
% display(Max_PotentialEnergy, 'Maximum Input Force:')
% display(Max_KineticEnergy, 'Maximum Output Rate of Change of Angular Momentum:')

figure(1) % Spring Force vs. Time
plot(tout, Fspring)
title('Spring Force during Leg Kick')
xlabel('Time (s)')
ylabel('Spring Force (N)')

figure(2) % Potential Engery vs. Time
plot(tout, PotentialEnergy)
title('Potential Energy during Leg Kick')
```

```
xlabel('Time(s)')
ylabel('Potential Energy (J)')

figure(3) % Angular Discplacement vs. Time
plot(tout, ADisplacement1)
title('Angular Acceleration during Leg Kick')
xlabel('Time(s)')
ylabel('Angular Displacement (deg/s^2)')
```

Appendix C: Case 2b - Spring Muscle Force in terms of θ Simulation Documents

Case 2b Simulink Block Diagram

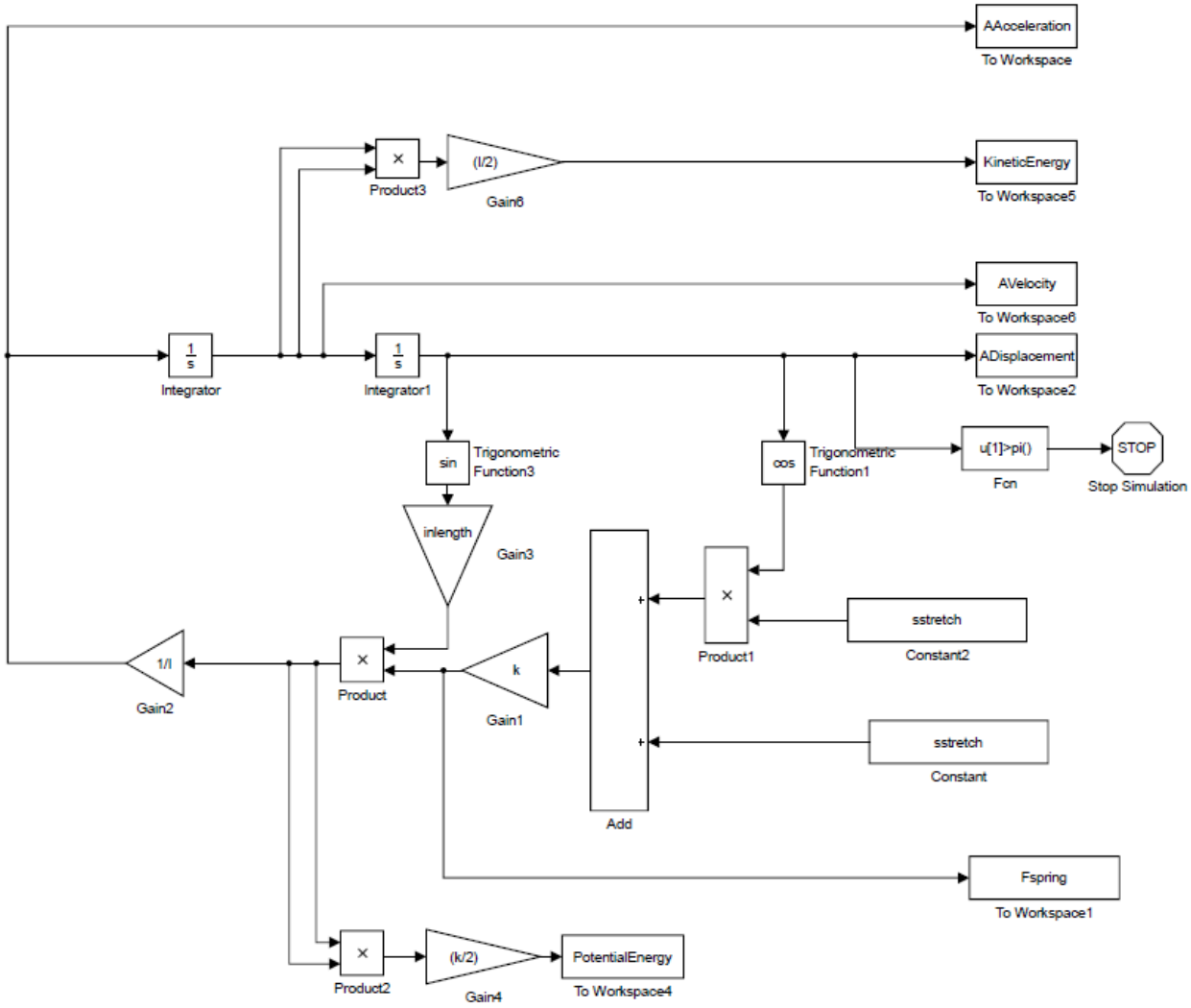

Case 2b MATLAB Code

```
%% Case 2b: Spring Force in Terms of Theta
% Created by: Jenna Hopkins

close all
clear all
clc

k = .3e3; %N/m
inlength = (7.6e-4)+((7.6e-4)*0)%m
sstretch = (1.5e-3)- (7.6e-4); %m
L = sstretch;%m
m = 110e-6; %kg
```

```
theta0 = 6*(pi()/180);%rad
lleg = 30e-3; %m
I = (m/3)*((lleg/2)^2); %kg-m^2
outlength = 1.73e-2;%m


MA = inlength/outlength; %Mechanical Advantage


sim('Sim_Locust3')
% Output of Simulink Data with ODE45
AAcceleration1 = AAcceleration*(180/pi()); % Angular Acceleration [deg/s^2]
AVelocity1 = AVelocity*(180/pi()); % Angular Velocity [deg/s]
ADisplacement1 = ADisplacement*(180/pi()); % Angular Displacement [deg]

% Correcting Simulation Output
j = size(ADisplacement1);

for i = 1:j
    if ADisplacement1(i) < 180 % Correction to take data points prior to 180 degrees
        ADisplacementc(i) = ADisplacement1(i);
        AAccelerationc(i) = AAcceleration1(i);
        KineticEnergyc(i) = KineticEnergy(i);
        AVelocityc(i) = AVelocity1(i);
        PotentialEnergyc(i) = PotentialEnergy(i);

    end
end

LAcceleration1 = (AAccelerationc*pi()/180)*outlength; % Lineaer Acceleration [m/s^2]
LVelocity1 = (AVelocityc*pi()/180)*outlength; % Linear Velocity [m/s]
LDisplacement1 = (ADisplacementc*pi()/180)*outlength; % Linear Displacement [m]

% Obtain Maximums of Kinematics
Max_AAcceleration = max(AAccelerationc); % Maximum Angular Acceleration [deg/s^2]
Max_AVelocity = max(AVelocityc); % Maximum Angular Velocity [deg/s]
Max_ADisplacement = max(ADisplacementc); % Maximum Angular Displacement [deg]

Max_LAcceleration = max(LAcceleration1); % Maximum Linear Acceleration [m/s^2]
Max_LVelocity = max(LVelocity1); % Maximum Linear Velocity [m/s]
Max_LDisplacement = max(LDisplacement1); % Maximum Linear Displacement [m]

Max_ForceInput = max(Fspring); %Maximum Spring Force [J]
Max_PotentialEnergy = max(PotentialEnergyc); %Maximum Potential Energy [J]
Max_KineticEnergy = max(KineticEnergyc); %Maximum Kinetic Energy [J]
rcam = (I.*AAccelerationc);
Max_rcam = max(rcam); %Maximum Rate of Change of Angular Momentum

% Display Data in Command Window
display(MA, 'Mechanical Advantage of System:')
display(Max_LVelocity, 'Maximum Linear Velocity:')
display(Max_ADisplacement, 'Maximum Angular Displacement:')
display(Max_ForceInput, 'Maximum Input Force:')
% display(Max_KineticEnergy, 'Maximum Output Rate of Change of Angular Momentum:')
display(Max_rcam, 'Maximum Rate of Change of Angular Momentum:')

figure(1) % Potential Energy during Kick
plot(tout, PotentialEnergy)
title('Potential Energy during Kick')
xlabel('Time(s)')
ylabel('Potential Energy (J)')

figure (2) %Force of Spring during Kick
```

```
plot(tout, Fspring)
title('Spring Force in Terms of Theta during Leg Kick')
xlabel('Time(s)')
ylabel('Spring Force (N)')
```

Appendix D: Case 3 - Spring – Damper Muscle Force Simulation Documents

Case 3 Simulink Block Diagram

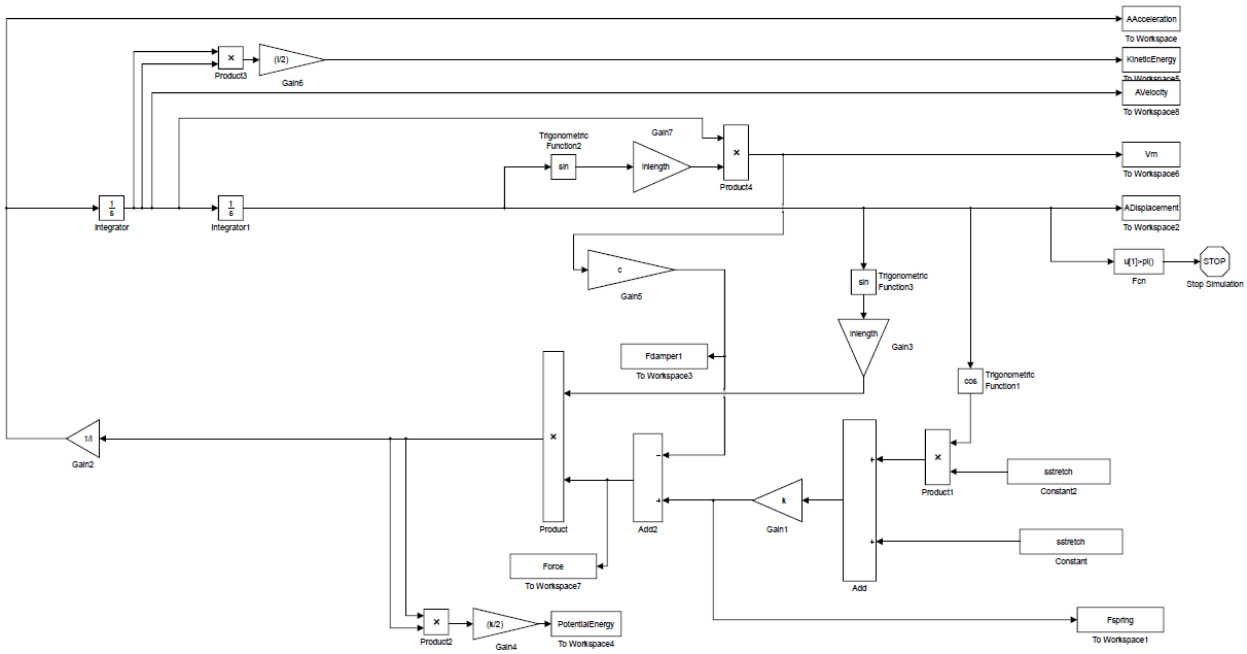

Case 3 MATLAB Code

```
%% Case 3: Spring-Damper Muscle
% Created by: Jenna Hopkins

close all
clear all
clc

k = .3e3; %N/m
inlength = (7.6e-4)+((7.6e-4)*0);%m
sstretch = (1.5e-3)-(7.6e-4); %m
L = sstretch;%m
m = 10e-6; %kg
theta0 = 6*(pi()/180);%rad
lleg = 30e-3; %m
I = (m/3)*((lleg/2)^2); %kg-m^2
outlength = 1.73e-2; %m
c =0.0001;  %Coefficient of Damping
g = -9.8; %m/s^2

MA = inlength/outlength;  %Mechanical Advantage


sim('Sim_Locust5')
% Output of Simulink Data with ODE45
AAcceleration1 = AAcceleration*(180/pi()); % Angular Acceleration [deg/s^2]
AVelocity1 = AVelocity*(180/pi()); % Angular Velocity [deg/s]
ADisplacement1 = ADisplacement*(180/pi()); % Angular Displacement [deg]

% Correcting Simulation Output
```

```
j = size(ADisplacement1);

for i = 1:j
    if ADisplacement1(i) < 180 %Correction to take data points before 180 degrees
        ADisplacementc(i) = ADisplacement1(i);
        AAccelerationc(i) = AAcceleration1(i);
        KineticEnergyc(i) = KineticEnergy(i);
        AVelocityc(i) = AVelocity1(i);
        PotentialEnergyc(i) = PotentialEnergy(i);

    end
end

LAcceleration1 = (AAccelerationc*pi()/180)*outlength; % Lineaer Acceleration [m/s^2]
LVelocity1 = (AVelocityc*pi()/180)*outlength; % Linear Velocity [m/s]
LDisplacement1 = (ADisplacementc*pi()/180)*outlength; % Linear Displacement [m]
LVelocity1t = LVelocity1';

% Obtain Maximums of Kinematics
Max_AAcceleration = max(AAccelerationc); % Maximum Angular Acceleration [deg/s^2]
Max_AVelocity = max(AVelocityc); % Maximum Angular Velocity [deg/s]
Max_ADisplacement = max(ADisplacementc); % Maximum Angular Displacement [deg]

Max_LAcceleration = max(LAcceleration1); % Maximum Linear Acceleration [m/s^2]
Max_LVelocity = max(LVelocity1); % Maximum Linear Velocity [m/s]
Max_LDisplacement = max(LDisplacement1); % Maximum Linear Displacement [m]

Max_ForceInput = max(Fspring); %Maximum Spring Force [J]
Max_PotentialEnergy = max(PotentialEnergyc); %Maximum Potential Energy [J]
Max_KineticEnergy = max(KineticEnergyc); %Maximum Kinetic Energy [J]
rcam = (I.*AAccelerationc);
Max_rcam = max(rcam); %Maximum Rate of Change of Angular Momentum
Max_Vm = max(Vm); % Maximum Muslce Velocity

% Display Data in Command Window
display(MA, 'Mechanical Advantage of System:')
display(Max_LVelocity, 'Maximum Linear Velocity:')
display(Max_ADisplacement, 'Maximum Angular Displacement:')
display(Max_ForceInput, 'Maximum Input Force:')
% display(Max_KineticEnergy, 'Maximum Output Rate of Change of Angular Momentum:')
display(Max_rcam, 'Maximum Rate of Change of Angular Momentum:')
display(Max_Vm, 'Maximum Muslce Velocity:')

figure (1)
subplot(4,1,1) % Angular Displacement during Kick
plot(tout, ADisplacement1)
title ('Angular Displacement vs Time')
xlabel('Times(s)')
ylabel('Angular Displacement (deg/s)')

subplot(4,1,2)
plot(tout, Vm) %Muscle Velocity
title('Muscle Velocity vs. Time')
xlabel('Time(s)')
ylabel('Muscle Velocity (m/s)')

subplot(4,1,3)
plot(tout, Force)% Force Output of Muscle
title('Force Output vs. Time')
xlabel('Time(s)')
ylabel('Muscle Force Applied (N)')

subplot(4,1,4)
```

```
plot(Fdamper1, Vm) % Force of Damping in Relation to Muscle Velocity
title('Muscle Velocity vs. Damping Force')
xlabel('Damping Force (N)')
ylabel('Muscle Force (N)'))

figure(2)
plot(tout, Fspring) % Force of the Spring during Kick

figure (3)
plot(tout, Fdamper1)% Damping Force during Kick
Fdamper1

figure (4)
plot(tout, PotentialEnergy) % Potential Energy during Kick
```

Appendix E: Case 4 - Spring – Damper Muscle Force with Consideration of Gravity Simulation Documents

Case 4 Simulink Block Diagram

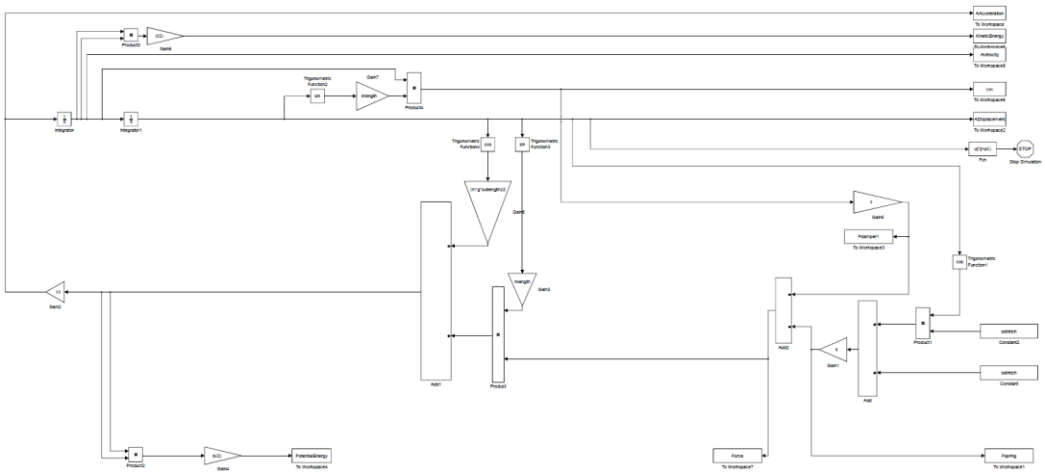

Case 4 MATLAB Code

```
%% Case 5: Spring-Damper Muscle with Gravity and Reaction Force
% Created by: Jenna Hopkins
 close all
clear all
clc

k = .3e3; %N/m
inlength = (7.6e-4)+((7.6e-4)*0);%m
sstretch = (1.5e-3)-(7.6e-4); %m
L = sstretch;%m
m = 80e-6; %kg
theta0 = 6*(pi()/180);%rad
lleg = 30e-3; %m
I = (m/3)*((lleg/2)^2); %kg-m^2
outlength = 1.73e-2;%m
c =0.5;% Damping Coefficient
g = -9.8; %m/s^2

MA = inlength/outlength;  %Mechanical Advantage


sim('WeightDistribution')
% Output of Simulink Data with ODE45
AAcceleration1 = AAcceleration*(180/pi()); % Angular Acceleration [deg/s^2]
AVelocity1 = AVelocity*(180/pi()); % Angular Velocity [deg/s]
ADisplacement1 = ADisplacement*(180/pi()); % Angular Displacement [deg]

% Correcting Simulation Output
j = size(ADisplacement1);

for i = 1:j
    if ADisplacement1(i) < 180 %Correction to get data points before 180 degrees
        ADisplacementc(i) = ADisplacement1(i);
        AAccelerationc(i) = AAcceleration1(i);
        KineticEnergyc(i) = KineticEnergy(i);
        AVelocityc(i) = AVelocity1(i);
```

```
        PotentialEnergyc(i) = PotentialEnergy(i);

    end
end

LAcceleration1 = (AAccelerationc*pi()/180)*outlength; % Lineaer Acceleration [m/s^2]
LVelocity1 = (AVelocityc*pi()/180)*outlength; % Linear Velocity [m/s]
LDisplacement1 = (ADisplacementc*pi()/180)*outlength; % Linear Displacement [m]
LVelocity1t = LVelocity1';

% Obtain Maximums of Kinematics
Max_AAcceleration = max(AAccelerationc); % Maximum Angular Acceleration [deg/s^2]
Max_AVelocity = max(AVelocityc); % Maximum Angular Velocity [deg/s]
Max_ADisplacement = max(ADisplacementc); % Maximum Angular Displacement [deg]

Max_LAcceleration = max(LAcceleration1); % Maximum Linear Acceleration [m/s^2]
Max_LVelocity = max(LVelocity1); % Maximum Linear Velocity [m/s]
Max_LDisplacement = max(LDisplacement1); % Maximum Linear Displacement [m]

Max_ForceInput = max(Fspring); %Maximum Spring Force [J]
Max_PotentialEnergy = max(PotentialEnergyc); %Maximum Potential Energy [J]
Max_KineticEnergy = max(KineticEnergyc); %Maximum Kinetic Energy [J]
rcam = (I.*AAccelerationc);
Max_rcam = max(rcam); %Maximum Rate of Change of Angular Momentum
Max_Vm = max(Vm); % Maximum Muslce Velocity

% Display Data in Command Window
display(MA, 'Mechanical Advantage of System:')
display(Max_LVelocity, 'Maximum Linear Velocity:')
display(Max_ADisplacement, 'Maximum Angular Displacement:')
display(Max_ForceInput, 'Maximum Input Force:')
% display(Max_KineticEnergy, 'Maximum Output Rate of Change of Angular Momentum:')
display(Max_rcam, 'Maximum Rate of Change of Angular Momentum:')
display(Max_Vm, 'Maximum Muslce Velocity:')

figure (1)
subplot(4,1,1)% Angular Displacment during Kick
plot(tout, ADisplacement1)
title ('Angular Displacement vs Time')
xlabel('Time(s)')
ylabel('Angular Displacement (deg/s)')

subplot(4,1,2)
plot(tout, Vm)% Muscle Velocity during Kick
title('Velocity vs. Time')
xlabel('Time(s)')
ylabel('Muslce Velocity (m/s)')

subplot(4,1,3)
plot(tout, Force) % Force of Muscle during Kick
title('Force Output vs. Time')
xlabel('Time(s)')
ylabel('Muscle Force Applied during Leg Kick (N)')

subplot(4,1,4)
plot(Fdamper1, Vm) % Muscle Velocity vs. Damping Force

figure(2) % Potential Energy during Kick
plot(tout, PotentialEnergy)
 figure (3) % Spring Force during Kick
plot(tout, Fspring)
 figure (4) % Force of Damper during Kick
plot(tout, Fdamper1)
```

Appendix F - Case 5 - Spring – Damper Muscle Force with Consideration of Gravity and Reaction Force Simulation Documents

Case 5 Simulink Block Diagram

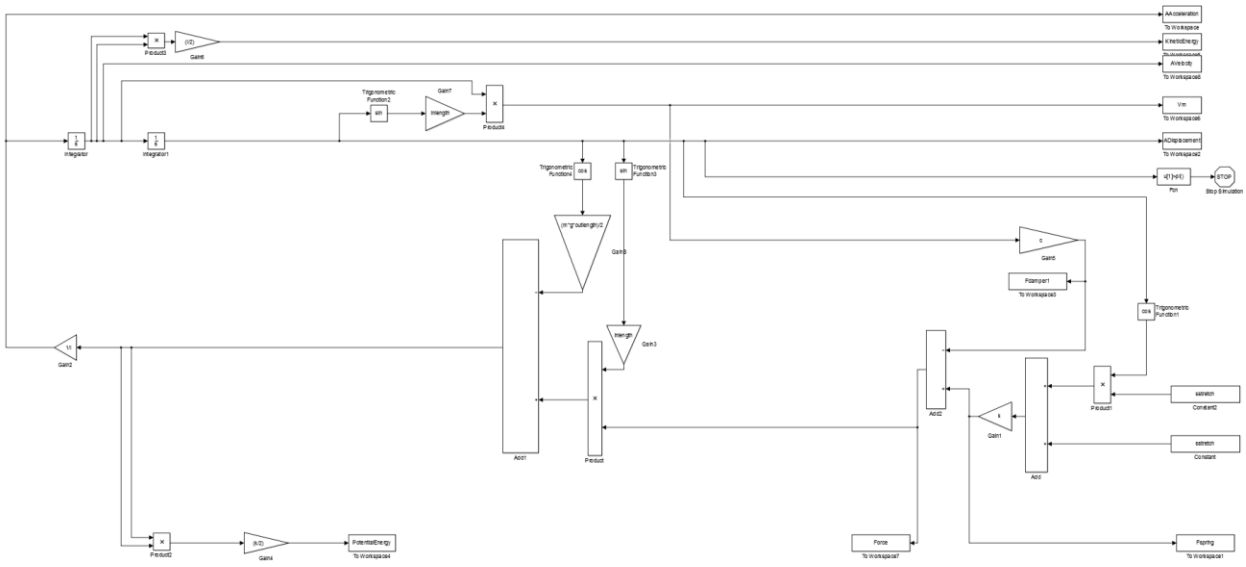

Case 5 MATLAB Code

```
%% Case 5: Spring-Damper Muscle with Gravity and Reactant Force
% Created by: Jenna Hopkins

close all
clear all
clc

k = .3e3; %N/m
inlength = (7.6e-4)+((7.6e-4)*0);%m
sstretch = (1.5e-3)-(7.6e-4); %m
L = sstretch;%m
m = 80e-6; %kg
theta0 = 6*(pi()/180);%rad
lleg = 30e-3; %m
I = (m/3)*((lleg/2)^2); %kg-m^2
outlength = 1.73e-2;%m
c =0.5; %Coefficient of Damping
g = -9.8; %m/s^2

MA = inlength/outlength;  % Mechanical Advantage


sim('ReactantForce')
% Output of Simulink Data with ODE45
AAcceleration1 = AAcceleration*(180/pi()); % Angular Acceleration [deg/s^2]
AVelocity1 = AVelocity*(180/pi()); % Angular Velocity [deg/s]
ADisplacement1 = ADisplacement*(180/pi()); % Angular Displacement [deg]

% Correcting Simulation Output
j = size(ADisplacement1);

for i = 1:j
```

```
    if ADisplacement1(i) < 180 % Correction to stop data collection to before 180
degrees
        ADisplacementc(i) = ADisplacement1(i);
        AAccelerationc(i) = AAcceleration1(i);
        KineticEnergyc(i) = KineticEnergy(i);
        AVelocityc(i) = AVelocity1(i);
        PotentialEnergyc(i) = PotentialEnergy(i);

    end
end

LAcceleration1 = (AAccelerationc*pi()/180)*outlength; % Lineaer Acceleration [m/s^2]
LVelocity1 = (AVelocityc*pi()/180)*outlength; % Linear Velocity [m/s]
LDisplacement1 = (ADisplacementc*pi()/180)*outlength; % Linear Displacement [m]
LVelocity1t = LVelocity1';

% Obtain Maximums of Kinematics
Max_AAcceleration = max(AAccelerationc); % Maximum Angular Acceleration [deg/s^2]
Max_AVelocity = max(AVelocityc); % Maximum Angular Velocity [deg/s]
Max_ADisplacement = max(ADisplacementc); % Maximum Angular Displacement [deg]

Max_LAcceleration = max(LAcceleration1); % Maximum Linear Acceleration [m/s^2]
Max_LVelocity = max(LVelocity1); % Maximum Linear Velocity [m/s]
Max_LDisplacement = max(LDisplacement1); % Maximum Linear Displacement [m]

Max_ForceInput = max(Fspring); %Maximum Spring Force [J]
Max_PotentialEnergy = max(PotentialEnergyc); %Maximum Potential Energy [J]
Max_KineticEnergy = max(KineticEnergyc); %Maximum Kinetic Energy [J]
rcam = (I.*AAccelerationc);
Max_rcam = max(rcam); %Maximum Rate of Change of Angular Momentum
Max_Vm = max(Vm); % Maximum Muslce Velocity

% Display Data in Command Window
display(MA, 'Mechanical Advantage of System:')
display(Max_LVelocity, 'Maximum Linear Velocity:')
display(Max_ADisplacement, 'Maximum Angular Displacement:')
display(Max_ForceInput, 'Maximum Input Force:')
% display(Max_KineticEnergy, 'Maximum Output Rate of Change of Angular Momentum:')
display(Max_rcam, 'Maximum Rate of Change of Angular Momentum:')
display(Max_Vm, 'Maximum Muslce Velocity:')


% figure (1)
% subplot(4,1,1)
% plot(tout, ADisplacement1)
% title ('Angular Displacement vs Time')
% xlabel('Time(s)')
% ylabel('Angular Displacement (deg/s)')
%
% subplot(4,1,2)
% plot(tout, Vm)
% title('Velocity vs. Time')
% xlabel('Time(s)')
% ylabel('Muslce Velocity (m/s)')
%
% subplot(4,1,3)
% plot(tout, Force)
% title('Force Output vs. Time')
% xlabel('Time(s)')
% ylabel('Muscle Force Applied during Leg Kick (N)')
%
% subplot(4,1,4)
% plot(Fdamper1, Vm)
```

```
% title('Muscle Velocity vs. Damping Force')
% xlabel('Damping Force (N)')
% ylabel('Muscle Velocity (m/s)')

% figure(2)
% plot(tout, PotentialEnergy)
%
% figure (3)
% plot(tout, Fspring)
% figure (4)
% plot(tout, Fdamper1)
% Fdamper1
```

Appendix G: Case 6 - Spring – Damper Muscle Force with Consideration of Gravity and Drag Force Simulation Documents

Case 6 Simulink Block Diagram

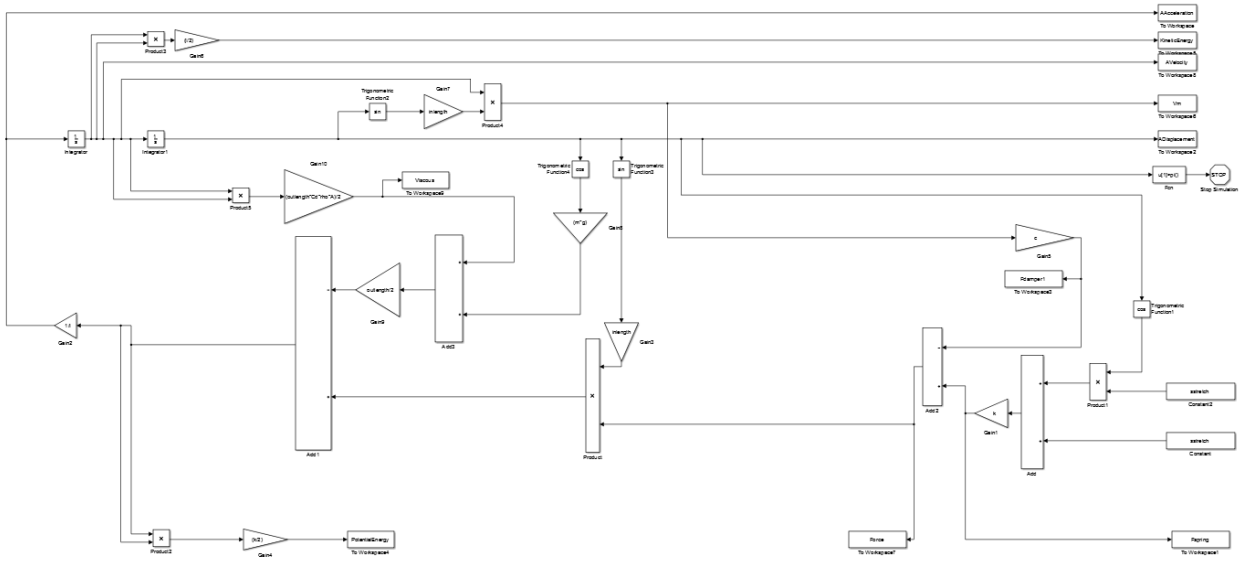

Case 6 MATLAB Code

```
%% Case 6: Spring-Damper Muscle Force with Consideration Gravity and Drag Force
close all
clear all
clc

k = .3e3; %N/m
inlength = (7.6e-4)+((7.6e-4)*0);%m
sstretch = (1.5e-3)-(7.6e-4); %m
L = sstretch;%m
m = 80e-6; %kg
theta0 = 6*(pi()/180);%rad
lleg = 30e-3;%m
I = (m/3)*((lleg/2)^2);%kg-m^2
outlength = 1.73e-2;%m
c =0.5;% Coefficient of Drag
g = -9.8; %m/s^2
Cd = 1.28; %assuming flat plate NASA determination
rho = 1261.08; %kg/m^3 which is varied based on % glycerine solution at 20C (Room
Temp)
A = 2*inlength*outlength;  % Projected Area of lower leg geometry.

MA = inlength/outlength;  % Mechanical Advantage


sim('ViscousDrag')
% Output of Simulink Data with ODE45
AAcceleration1 = AAcceleration*(180/pi()); % Angular Acceleration [deg/s^2]
AVelocity1 = AVelocity*(180/pi()); % Angular Velocity [deg/s]
ADisplacement1 = ADisplacement*(180/pi()); % Angular Displacement [deg]

% Correcting Simulation Output
j = size(ADisplacement1);
```

```
for i = 1:j
    if ADisplacement1(i) < 180 %Correction to obtain data prior to 180 degrees
        ADisplacementc(i) = ADisplacement1(i);
        AAccelerationc(i) = AAcceleration1(i);
        KineticEnergyc(i) = KineticEnergy(i);
        AVelocityc(i) = AVelocity1(i);
        PotentialEnergyc(i) = PotentialEnergy(i);

    end
end

LAcceleration1 = (AAccelerationc*pi()/180)*outlength; % Lineaer Acceleration [m/s^2]
LVelocity1 = (AVelocityc*pi()/180)*outlength; % Linear Velocity [m/s]
LDisplacement1 = (ADisplacementc*pi()/180)*outlength; % Linear Displacement [m]
LVelocity1t = LVelocity1';

% Obtain Maximums of Kinematics
Max_AAcceleration = max(AAccelerationc); % Maximum Angular Acceleration [deg/s^2]
Max_AVelocity = max(AVelocityc); % Maximum Angular Velocity [deg/s]
Max_ADisplacement = max(ADisplacementc); % Maximum Angular Displacement [deg]

Max_LAcceleration = max(LAcceleration1); % Maximum Linear Acceleration [m/s^2]
Max_LVelocity = max(LVelocity1); % Maximum Linear Velocity [m/s]
Max_LDisplacement = max(LDisplacement1); % Maximum Linear Displacement [m]

Max_ForceInput = max(Fspring); %Maximum Spring Force [J]
Max_PotentialEnergy = max(PotentialEnergyc); %Maximum Potential Energy [J]
Max_KineticEnergy = max(KineticEnergyc); %Maximum Kinetic Energy [J]
rcam = (I.*AAccelerationc);
Max_rcam = max(rcam); %Maximum Rate of Change of Angular Momentum
Max_Vm = max(Vm); % Maximum Muslce Velocity

% Display Data in Command Window
display(MA, 'Mechanical Advantage of System:')
display(Max_LVelocity, 'Maximum Linear Velocity:')
display(Max_ADisplacement, 'Maximum Angular Displacement:')
display(Max_ForceInput, 'Maximum Input Force:')
% display(Max_KineticEnergy, 'Maximum Output Rate of Change of Angular Momentum:')
display(Max_rcam, 'Maximum Rate of Change of Angular Momentum:')
display(Max_Vm, 'Maximum Muslce Velocity:')
% figure(7)
% plot(tout, PotentialEnergy)
%
% figure (8)
% plot(tout, Fspring)
% figure (9)
% plot(tout, Fdamper1)
% Fdamper1

figure (1)
subplot(4,1,1)
plot(tout, ADisplacement1)
title ('Angular Displacement vs Time')
xlabel('Time(s)')
ylabel('Angular Displacement (deg/s)')

subplot(4,1,2)
plot(tout, Vm)
title('Velocity vs. Time')
xlabel('Time(s)')
ylabel('Muslce Velocity (m/s)')
```

```
subplot(4,1,3)
plot(tout, Force)
title('Force Output vs. Time')
xlabel('Time(s)')
ylabel('Muscle Force Applied during Leg Kick (N)')

subplot(4,1,4)
plot(Fdamper1, Vm)
title('Muscle Velocity vs. Damping Force')
xlabel('Damping Force (N)')
ylabel('Muscle Velocity (m/s)')

figure (2)
plot(Force, Vm)
```

Appendix H: Experimental Data Post-Processing MatLab Code for Force, Inertial, and Viscous Loading

```
%% Experimental Data Processing: Minimal Damping Trial 2 - Force Loading
% Created by: Jenna Hopkins

close all
clear all
clc
format compact

%%Read Spreadsheet in Matlab

% 500g Spreadsheet (One Load)
One = xlsread('Force Scenario (Minimal Damping 3.xlsx', 10);
t1 = One(:,1);
v1 = One(:,2);
iterationsperstep = 40;
coeff4stepMA = ones(1, iterationsperstep)/iterationsperstep;
averagevel1 = filter(coeff4stepMA, 1, v1);
fDelay1 = (length(coeff4stepMA)-1)/2;
figure(1)
plot(t1, v1,t1-fDelay1/85, averagevel1)
ylabel('Contractile Velocity (m/s)')
xlabel('Time (s)')
title('Contractile Velocity of "Muscle" with 500g Load')
legend('Raw Data for 500g Load', 'Moving Average Filtered Data')

% 1000g Spreadsheet (One Load)
One = xlsread('Force Scenario (Minimal Damping 3.xlsx', 10);
t2 = One(:,3);
v2 = One(:,4);
iterationsperstep = 40;
coeff4stepMA = ones(1, iterationsperstep)/iterationsperstep;
averagevel2 = filter(coeff4stepMA, 1, v2);
fDelay2 = (length(coeff4stepMA)-1)/2;
figure(2)
plot(t2, v2,t2-fDelay2/85, averagevel2)
ylabel('Contractile Velocity (m/s)')
xlabel('Time (s)')
title('Contractile Velocity of "Muscle" with 1000g Load')
legend('Raw Data for 1000g Load', 'Moving Average Filtered Data')

% 1500g Spreadsheet (One Load)
One = xlsread('Force Scenario (Minimal Damping 3.xlsx', 10);
t3 = One(:,5);
v3 = One(:,6);
iterationsperstep = 40;
coeff4stepMA = ones(1, iterationsperstep)/iterationsperstep;
averagevel3 = filter(coeff4stepMA, 1, v3);
fDelay3 = (length(coeff4stepMA)-1)/2;
figure(3)
plot(t3, v3,t3-fDelay3/85, averagevel3)
ylabel('Contractile Velocity (m/s)')
xlabel('Time (s)')
title('Contractile Velocity of "Muscle" with 1500g Load')
legend('Raw Data for 1500g Load', 'Moving Average Filtered Data')
```

```
% 2000g Spreadsheet (One Load)
One = xlsread('Force Scenario (Minimal Damping 3.xlsx', 10);
t4 = One(:,7);
v4 = One(:,8);
iterationsperstep = 40;
coeff4stepMA = ones(1, iterationsperstep)/iterationsperstep;
averagevel4 = filter(coeff4stepMA, 1, v4);
fDelay4 = (length(coeff4stepMA)-1)/2;
figure(4)
plot(t4, v4,t4-fDelay4/85, averagevel4)
ylabel('Contractile Velocity (m/s)')
xlabel('Time (s)')
title('Contractile Velocity of "Muscle" with 2000g Load')
legend('Raw Data for 2000g Load', 'Moving Average Filtered Data')

% 2500g Spreadsheet (One Load)
One = xlsread('Force Scenario (Minimal Damping 3.xlsx', 10);
t5 = One(:,9);
v5 = One(:,10);
iterationsperstep = 40;
coeff4stepMA = ones(1, iterationsperstep)/iterationsperstep;
averagevel5 = filter(coeff4stepMA, 1, v5);
fDelay5 = (length(coeff4stepMA)-1)/2;
figure(5)
plot(t5, v5,t5-fDelay5/85, averagevel5)
ylabel('Contractile Velocity (m/s)')
xlabel('Time (s)')
title('Contractile Velocity of "Muscle" with 2500g Load')
legend('Raw Data for 2500g Load', 'Moving Average Filtered Data')

% 3000g Spreadsheet (One Load)
One = xlsread('Force Scenario (Minimal Damping 3.xlsx', 10);
t6 = One(:,11);
v6 = One(:,12);
iterationsperstep = 40;
coeff4stepMA = ones(1, iterationsperstep)/iterationsperstep;
averagevel6 = filter(coeff4stepMA, 1, v6);
fDelay6 = (length(coeff4stepMA)-1)/2;
figure(6)
plot(t6, v6,t6-fDelay6/85, averagevel6)
ylabel('Contractile Velocity (m/s)')
xlabel('Time (s)')
title('Contractile Velocity of "Muscle" with 3000g Load')
legend('Raw Data for 3000g Load', 'Moving Average Filtered Data')

% 3500g Spreadsheet (One Load)
One = xlsread('Force Scenario (Minimal Damping 3.xlsx', 10);
t7 = One(:,13);
v7 = One(:,14);
iterationsperstep = 40;
coeff4stepMA = ones(1, iterationsperstep)/iterationsperstep;
averagevel7 = filter(coeff4stepMA, 1, v7);
fDelay7 = (length(coeff4stepMA)-1)/2;
figure(7)
plot(t7, v7,t7-fDelay7/85, averagevel7)
ylabel('Contractile Velocity (m/s)')
xlabel('Time (s)')
title('Contractile Velocity of "Muscle" with 3500g Load')
legend('Raw Data for 3500g Load', 'Moving Average Filtered Data')

% 4000g Spreadsheet (One Load)
One = xlsread('Force Scenario (Minimal Damping 3.xlsx', 10);
```

```
t8 = One(:,15);
v8 = One(:,16);
iterationsperstep = 40;
coeff4stepMA = ones(1, iterationsperstep)/iterationsperstep;
averagevel8 = filter(coeff4stepMA, 1, v8);
fDelay8 = (length(coeff4stepMA)-1)/2;
figure(8)
plot(t8, v8,t8-fDelay8/85, averagevel8)
ylabel('Contractile Velocity (m/s)')
xlabel('Time (s)')
title('Contractile Velocity of "Muscle" with 4000g Load')
legend('Raw Data for 4000g Load', 'Moving Average Filtered Data')
```